

Physically transient electronic materials and devices

Jun-Seok Shim ^a, John A. Rogers ^{b,c,d,e,f,**}, Seung-Kyun Kang ^{a,g,h,*}



^a Department of Materials Science and Engineering, Seoul National University, Seoul, 08826, Republic of Korea

^b Center for Bio-Integrated Electronics, Northwestern University, Evanston, IL, 60208, USA

^c Querrey Simpson Institute for Biotechnology, Northwestern University, Evanston, IL, 60208, USA

^d Department of Materials Science Engineering, Northwestern University, Evanston, IL, 60208, USA

^e Department of Biomedical Engineering, Chemistry, Mechanical Engineering, Electrical Engineering, Computer Science and Neurological Surgery, Northwestern University, Evanston, IL, 60208, USA

^f Department of Neurological Surgery, Feinberg School of Medicine, Northwestern University, Chicago, IL, 60611, USA

^g Research Institute of Advanced Materials, Seoul National University, Seoul, 08826, Republic of Korea

^h Institute of Engineering Research, Seoul National University, Seoul, 08826, Republic of Korea

ARTICLE INFO

Keywords:

Transient electronics
Biodegradable electronics
Ecofriendly electronics
Trigger transient electronics
Si dissolution chemistry

ABSTRACT

Transient electronics, which can be tuned to be completely or partially dissolvable, degradable, and disintegrable, create new opportunities in the upcoming ubiquitous electronics era that are inaccessible with conventional permanent electronics. This emerging field offers unique electronic applications in environmentally degradable eco-devices with minimal or zero waste, biodegradable medical implants not requiring secondary removal surgery, and hardware-based security devices with self-destructing circuits. Nanoscale thin-film processing that exploits Si in single-crystalline form and related techniques allow construction of transient electronics with high performance and versatile characteristics, including nearly all types of active electronic components, integrated circuits, sensors and other integrated wireless medical devices. Here we review recently developed transient electronics and materials, mainly illustrating representative inorganic and Si electronic materials technologies. Dissolution chemistry and reaction kinetics of semiconductors, dielectric and metal conductors are described to explain the dependence on environmental conditions such as temperature, pH, ion species and materials microstructure, density, crystallinity, composition. Materials and approaches that define the functional lifetime of transient electronic are introduced in two aspects: using passive encapsulation layers to control water-vapor diffusion and using on-demand active triggerable systems of stimulus-responsive materials. Transfer-printing approaches and solution printing processes offer strategies to integrate high-performance inorganic electronic materials with soft and flexible biodegradable organic substrates. Various examples of biodegradable medical electronics for clinically relevant diseases and symptoms support effective practical applications.

1. Introduction

The rapid development of electronic devices has contributed to convenience in daily life and to advanced smart medical care [1–11]. Bio-integrated electronic devices, for example, that perform real-time and remote diagnosis and treatment inside or outside the body offer possibilities for personalized, mobilized, and autonomous medical services [1–11]. Conventional electronic devices should provide stable and reliable long-term operation and durability; however, excessive use of long-lasting electronics results in problems, such as pollution caused by toxic electronic wastes [12–14]. An expanding collection of electronic

systems will be applied to daily life including biomedical healthcare, thus motivating needs for biocompatible and eco-compatible form of electronics [1–11]. Transient electronics, which have the ability to disappear either partially or completely in a controlled manner via dissolution, degradation, or disintegration, through electrochemical, mechanical, or chemical processes, suggest a new paradigm of bio/eco-compatible electronics that exist only for a required amount of time [15]. The concept of transient electronics enables the fabrication of minimal or zero-waste electronics without harmful byproducts and creates new opportunities in the biomedical field, such as biodegradable electronic devices that do not pose residue issues and do not require

* Corresponding author at: Department of Materials Science and Engineering, Seoul National University, Seoul, 08826, Republic of Korea.

** Corresponding author at: Center for Bio-Integrated Electronics, Northwestern University, Evanston, IL, 60208, USA.

E-mail addresses: jrogers@northwestern.edu (J.A. Rogers), kskg7227@snu.ac.kr (S.-K. Kang).

removal surgery [8–11]. In addition, hardware security devices that protect sensitive information in personal mobile devices and military security devices by destroying key hardware permanently when they are exposed to unwanted parties can also be developed using concepts in transient electronics [16–18].

The study of transient electronics initially starts from works on partially degradable electronics. Although eco/bio-degradable platforms including scaffolds, surgical suture thread, bone joints, bioactive glasses, drug delivery vehicles, and others in the use of environmentally degradable eco-friendly bioplastics and biomedical implants developed from non-electrical functional transient materials was presented, most of these functions are limited to passive structures [19,20]. The partially degradable inorganic transistor comprising Si nanomembranes (Si NMs) semiconducting channel, SiO_2 gate dielectric, Au electrode and polyimide (PI) encapsulation on silk substrate with electron mobility, threshold voltage, and on/off ratio of $\sim 500 \text{ cm}^2/\text{V}\cdot\text{s}$, $\sim 0.2 \text{ V}$, and $> 10^4$ first suggested the concept of transient electronics [21]. Here fast dissolution of silk substrate causes the disintegration of circuits after immersion in water [21].

The biodegradable organic transistor also provides an important contribution to electrically functional transient materials and devices. Bettinger et al. demonstrated an organic thin film transistor composed of a 5,5'-bis-(7-dodecyl-9H-fluoren-2-yl)-2,2'-bithiophene (DDFTTF) semiconductor, poly(vinyl alcohol) (PVA) as a dielectric, and poly(L-lactide-co-glycolide) (PLGA) as a substrate, with a mobility, on/off ratio, and threshold voltage of $0.207 \pm 0.069 \text{ cm}^2/\text{V}\cdot\text{s}$, $5.5 \pm 2.1 \times 103$, and $-15.4 \pm 1.7 \text{ V}$, respectively [22]. Several studies have been performed using organics developed from natural materials, including eumelanin, β -carotene, indanthrene yellow G, indanthrene brilliant orange RF, and perylene diimide, which have been used as semiconductors, and sugars (glucose, lactose, and sucrose), nucleobases (adenine and guanine), and caffeine, which have been used as dielectrics [23]. Recently developed synthetic semiconducting polymers such as poly(diketopyrrolopyrrole-p-phenylenediamine) (PDPP-PD), which is synthesized through a condensation reaction between diketopyrrolopyrrole-aldehyde and p-phenylenediamine under the catalysis of toluenesulfonic acid, demonstrate flexible electronics with biodegradability [24,25]. Transient organic transistors based on PDPP-PD show relatively high hole mobilities of $0.21 \pm 0.03 \text{ cm}^2/\text{V}\cdot\text{s}$ and an average threshold voltage of $4.67 \pm 0.28 \text{ V}$ with high flexibility, exhibiting less than a 5% change in the transfer characteristics during bending deformation, with a 2-mm radius [24]. Although it is possible to fabricate transient electronics with acceptable operation for certain, narrow classes of applications using organic materials, their performance is still limited compared to devices based on inorganic materials.

The demonstration of fully biodegradable inorganic electronics using Si single crystalline in nanomembrane form offers another transition toward high-performance transient electronics and exploits related research into all aspects of materials and device studies [15]. Hwang et al. showed that 70-nm-thick electronic-grade Si nanomembranes dissolves in phosphate buffered saline (PBS) at 37°C within approximately 15 days and also demonstrated fully biodegradable Si devices, such as diodes, transistors, and various sensors, developed using Si NM semiconductors, MgO and/or SiO_2 dielectrics, and Mg conductors on biodegradable silk substrates [15]. This innovation relies on two important features: 1) a significant reduction in thickness turns slowly soluble materials (traditionally regarded as insoluble in conventional, bulk forms) into degradable materials within an acceptable time frame for many applications, and 2) most aspects of Si electronics technology, including device architecture, fabrication, circuit design, and packaging, can be exploited in transient electronics [15]. Extensive research on Si transient electronics has examined the basic electronic active and passive components involved, such as diodes, transistors, capacitors, integrated circuits such as complementary metal–oxide–semiconductor (CMOS), inverters, NAND, NOR gates, and ring oscillators that exploit semiconducting properties, solar cells, image sensors based on

photovoltaic and photoconducting behavior, mechanical sensors such as strain sensors, accelerometers, pressure sensors with piezoresistivity, and pH sensors constructed using ion-sensitive transistors [9,15,26–29].

Fig. 1 summarize the topics important to transient electronic studies in materials science and engineering. Understanding of the dissolution chemistry of electrically functional materials, such as semiconductors, dielectrics, and conductors, is the starting point in designing high-performance transient electronics with lifetimes suitable for their applications [15,30–37]. The dissolution kinetics of such devices are highly dependent on environmental conditions, including temperature and ion species, as well as the intrinsic microstructure, geometry, and thickness of the materials. In this way, kinetic models and databases offer wide ranges of tunability of life cycles, depending on the application [38–40]. Precise control of the lifetime of a transient electronic device is critically important, along with the dissolution time frame as a function of electronic change or function, even via partial degradation, dissolution, or destruction of the circuit [16–18,41]. The materials and strategies used to control the lifetime (or the dissolution time), including accelerating, decelerating, and initiating degradation of transient electronics, as important strategies [16–18,36,41–43]. Fabrication strategies for integrating transient materials that have relatively strong reactivity to water, organic solvents, and temperature into electronic devices are also essential [26,27,44–53]. For example, transfer printing technology that uses a sacrificial or temporary processing substrate avoids exposure of sensitive materials to aggressive conditions, and solution processes enable low-temperature and solvent-compatible fabrication [26,27,44–53]. Transient electronics formed with materials that have well-studied dissolution kinetics and with optimized fabrication processes yield reliable operational lifetimes for a wide range of electronics, from components to integrated devices and sensors with unique and powerful applications [9,15,26–29,32]. These materials and fabrication strategies can be utilized in diverse biomedical devices, eco-friendly devices, and security devices [8–11,17,18,54].

This paper reviews the history and recent progress in four aspects of transient electronics development. First, the dissolution chemistry and kinetics of transient electronic materials used in semiconductors, dielectrics, and conductors are introduced. The dissolution kinetics of Si NMs are mainly discussed with respect to various environmental effects, including temperature, pH, anion and cation concentrations, and protein, as well as microstructural effects, such as crystallinity, porosity, and alloying. The dissolution chemistry and kinetics of other transient semiconductors, such as Ge, SiGe, ZnO , and amorphous indium-gallium-zinc-oxide (a-IGZO), are reviewed to summarize the wide choices of materials for active electronics. Dielectric materials, which are important for gate dielectrics and passivation, are discussed in a manner similar to Si dissolution chemistry and kinetics for silicon oxides and nitrides, magnesium oxides, and spin-on-glasses. The biodegradation of five representative metals (Mg, Zn, Fe, Mo, and W) used in transient electronics shows different chemistries and kinetics related to the formation of oxides and microstructure variation. Potential candidates for biodegradable metals for transient electronics are also discussed.

Second, materials and strategies for controlling the lifetime in passive and active modes are introduced in the context of encapsulation and trigger transient materials. The role of water permeation in biodegradable encapsulation is highlighted for both inorganic and organic transient passivation materials. Microstructural defects critically affect the water-barrier characteristics of inorganic encapsulants, while molecular chemistry is key in organic encapsulation. Representative encapsulation materials and methods are discussed. The use of triggered transient electronics, which are usually made of stimulus-responsive materials, to actively initiate degradation and disintegration mechanisms are discussed. Triggering systems using unusual materials that interact with external stimuli such as light, heat, and electrical fields are classified on the basis of the initiation mechanism or direct source of degradation. Remote controllability of trigger transience and extension to transformation of function are described.

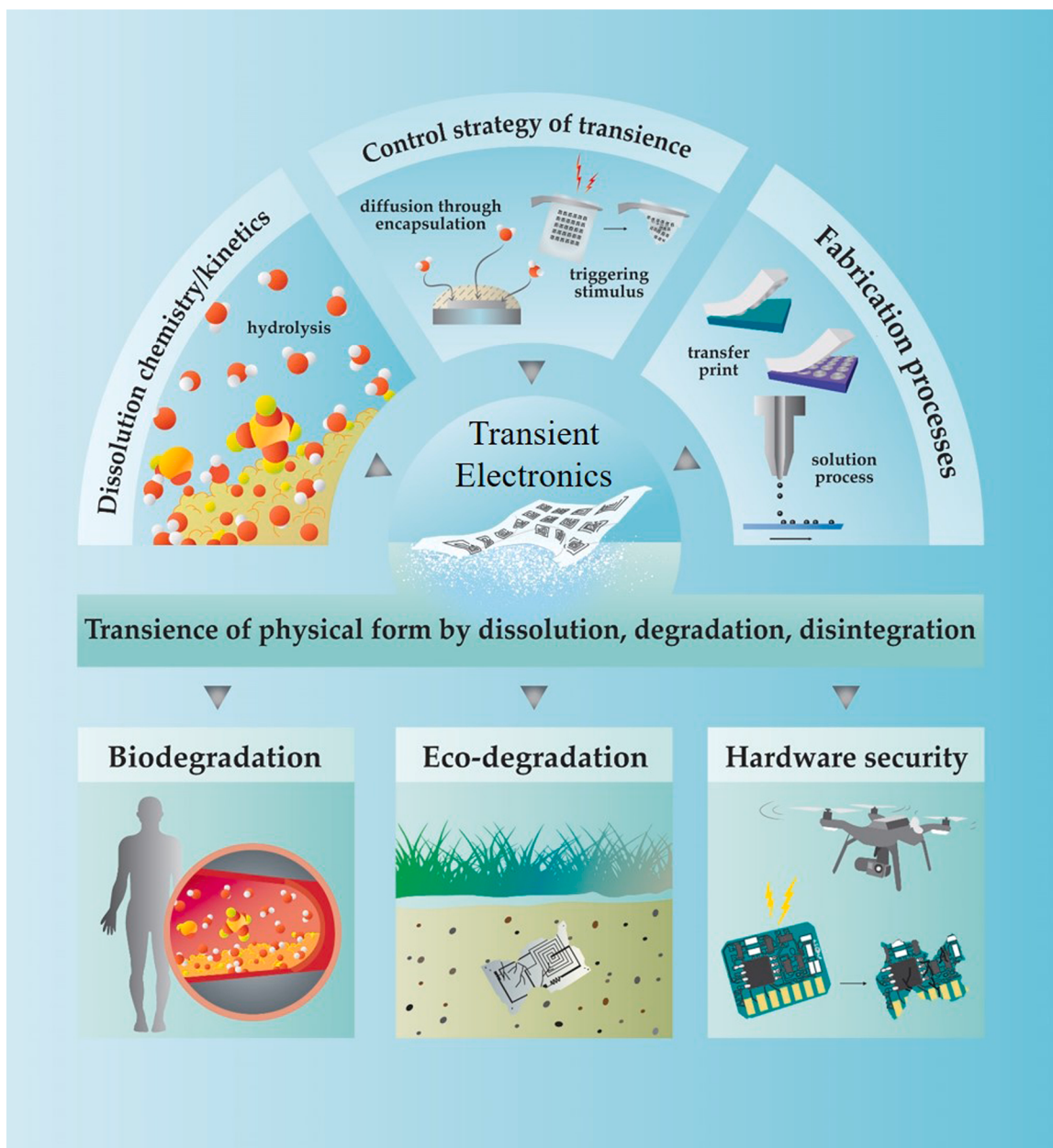


Fig. 1. Schematic illustration of representative fields and applications of transient electronics.

Next, two approaches to minimizing exposure of sensitive materials in the reactive step of the fabrication process are discussed. Transfer-printing technology that exploits Si photolithographic processes can be used to produce integrated transient inorganic devices with high performance and sophisticated features on biodegradable and flexible soft polymer substrates. A solution process using a mixture of biodegradable organic binders and a biodegradable inorganic filler offering a low-temperature process and mass production options are reviewed with various methods to enhance the conductivity and long-term suitability.

Finally, various transient devices, including basic electronic components, electronic circuits, and sensors, are introduced. Transient energy sources, including energy storage devices and harvesting systems, are also discussed in terms of their role in supporting the independent operation of transient electronic devices. Medical applications for biodegradable devices for temporary sensing and therapy, including treatment of traumatic injury, regenerative medicine, post-operative monitoring, and on-demand drug release, demonstrate the clinically

relevant usage of transient electronics in practice.

2. Dissolution chemistry of transient inorganic electronic materials

2.1. Dissolution kinetics of Silicon Nanomembranes

2.1.1. Effect of solution and temperature on dissolution kinetics

Anisotropic etching (fast dissolution) of monocrystalline silicon (mono-Si) in an aqueous alkaline solution is the starting point in studying the dissolution of silicon in biofluids. Si etching technology has been widely used in various silicon structures such as passive mechanical elements, sensors, actuators, and micro-optical components in a highly controllable and reproducible manner due to its anisotropy and smoothly controllable etch rate by changing the etchant concentration and intrinsic factors of the silicon [55]. The main component of silicon etchants is either an organic solution using ethylenediamine (EDP, $\text{NH}_2(\text{CH}_2)_2\text{NH}_2$) and pyrocatechol ($\text{C}_2\text{H}_4(\text{OH})_2$), or an inorganic

solution of KOH or NaOH [55]. Both systems have OH⁻ as the main species, and etching occurs by the reaction of silicon with OH⁻ in the following steps [55]. First, nucleophilic attack of two OH⁻ onto silicon surfaces with dangling bonds occurs, weakening the backbonds of the surface silicon atoms. OH⁻ forms Si—O bonding by attacking the Si backbond because the Si-O binding energy (193 kcal/mol) is greater than the Si-Si binding energy (78 kcal/mol). Backbond breakage forms a silicon-hydroxide complex that is further combined with two other OH⁻ to form Si(OH)₄. The formation of Si(OH)₄ follows: Si + 4H₂O → Si(OH)₄ + 2H₂. Si(OH)₄ is relatively unstable in strong basic solutions (over pH 12), so two additional H⁺ are detached to form SiO₂(OH)₂⁻ [55]. The overall reaction in strong basic solution is: Si + 2OH⁻ + 2H₂O → SiO₂(OH)₂⁻ + 2H₂ [55]. The concentration of OH⁻ is closely related to the etch rate because OH⁻ is the main species in the anisotropic etching that weakens the silicon backbonds [55]. The etch rate is proportional to the fourth power of [H₂O] in aqueous KOH solutions, as expressed by R ~ [H₂O]⁴[KOH]^{1/4}, where R is the Si etch rate [55]. Combined with the effect of temperature in Arrhenius scaling, the following formula is known as the etch rate of Si in KOH:

$$R = k_0[H_2O]^4[KOH]^{1/4}e^{-E_a/kT} \quad (1)$$

E_a and k₀ are found to be ~0.59 eV and 2480 μm/h × (mol/L)^{-4.25} [55].

Recent research has shown that Si NMs provide excellent flexibility with high performance comparable to conventional electronics [15]. While Si NMs have made possible the fabrication of various types of new silicon devices in flexible platforms through their transferable, stackable, bondable, and manufacturable properties, they have also strongly influenced the dissolution kinetics of Si [15]. Si NMs can be completely dissolved more quickly even in mild aqueous solutions, because of the extreme reduction of the thickness scale. Table 1 summarizes studies of the dissolution kinetics of Si NMs in mild aqueous solutions including various species [34,35,38,39,56].

Hwang et al. were the first to report that electronic-grade monocrystalline Si NMs can dissolve on relatively short timescales, through experiments on membranes with thicknesses 70 nm that dissolve in mild pH PBS (1.0 M, pH 7.4, Sigma-Aldrich, USA) with a dissolution rate about 4.5 nm/day at body temperature (37 °C) and 2 nm/day at room temperature (RT, 25 °C) [15]. Fig. 2A shows the atomic force microscope (AFM) images of Si NMs during dissolution in PBS at 37 °C [15]. The dissolution mechanism of silicon induced by nucleophilic attack of OH⁻ is similar to that of the anisotropic etching, but unlike at high pH of 12 or higher, Si(OH)₄ is stable in near-neutral solutions [15,33,34]. Si(OH)₄ molecules diffuse from the solid surface into the aqueous solution, leading to silicon dissolution to the equilibrium



The increased concentration of OH⁻ in this equilibrium accelerates the dissolution, as OH⁻ initiates dissolution [34]. Fig. 2B and 2C shows the relationship of OH⁻ concentration with thickness change and dissolution rate when Si NM of thickness 70 nm is immersed into a different aqueous buffer solution of pH 6–14 (pH 6 - citric acid/sodium hydroxide solution, pH 7 - potassium dihydrogen phosphate/disodium hydrogen phosphate, pH 8 - borax/hydrochloric acid, pH 10 - di-sodium tetraborate/sodium hydroxide, pH 12 - di-sodium hydrogen phosphate/sodium hydroxide solution, pH 13 - glycine/sodium hydroxide/sodium chloride solution, pH 14 - sodium hydroxide added to pH 13.0 to adjust the pH value, Sigma-Aldrich, USA). The dissolution rate is expressed by

$$R = k_0[H_2O]^4[OH^-]^{1/4}e^{-E_a/kT} \quad (3)$$

modified from anisotropic etching (Eq. (1)). Here E_a and k₀ are experimentally determined from Fig. 2C as ~0.40 eV and 7045 nm/h × (mol/L)^{-4.25}, respectively [34]. The concentration of Si(OH)₄, a byproduct of hydrolysis, also affects the dissolution rate. High

Table 1

Factors	Silicon	Solution	Dissolution rate	Refs.
		Aqueous buffer solution, pH 6 ~ 14, (Sigma-Aldrich, USA, pH 6 - citric acid/sodium hydroxide solution, pH 7 - potassium dihydrogen phosphate/disodium hydrogen phosphate, pH 8 - borax/hydrochloric acid, pH 10 - di-sodium tetraborate/sodium hydroxide, pH 12 - di-sodium hydrogen phosphate/sodium hydroxide solution, pH 13 - glycine/sodium hydroxide/sodium chloride solution, pH 14 - sodium hydroxide added to pH 13.0 to adjust the pH value, Sigma-Aldrich, USA)		
pH (OH ⁻)	70 nm thickness on SiO ₂ /Si substrate		Increases with pH	[34]
Anions				
Cl ⁻ , PO ₄ ³⁻	Lightly p-doped 10 ¹⁷ cm ⁻³ , 320 nm thickness on SiO ₂ /Si substrate	(molar ratio 19.8/80.2, Sigma-Aldrich, USA), Phosphate & chloride 0.05 ~ 1 M, pH 7.5, 37 °C PBS (1x, pH 7.4, Corning cellgro, USA), Si(OH) ₄ 0 ~ 200 ppm, albumin 10 ⁻² g/L 30 mL, 37 °C PBS (1x, pH 7.4, Corning cellgro, USA), NaCl, CaCl ₂ , MgCl ₂ 0 ~ 1 mM, 30 mL, 37 °C PBS (1x, pH 7.4, Corning cellgro, USA), albumin 10 ⁻² g/L ~ 35 g/L, 30 mL, 37 °C PBS (1x, pH 7.4, Corning cellgro, USA), albumin 10 ⁻² g/L 30 mL, 37 °C	Increases with the concentration of anions	[38]
Si(OH) ₄	Lightly p-doped 10 ¹⁵ cm ⁻³ , 200 nm thickness on SiO ₂ /Si substrate	(molar ratio 19.8/80.2, Sigma-Aldrich, USA), Phosphate & chloride 0.05 ~ 1 M, pH 7.5, 37 °C PBS (1x, pH 7.4, Corning cellgro, USA), Si(OH) ₄ 0 ~ 200 ppm, albumin 10 ⁻² g/L 30 mL, 37 °C PBS (1x, pH 7.4, Corning cellgro, USA), NaCl, CaCl ₂ , MgCl ₂ 0 ~ 1 mM, 30 mL, 37 °C PBS (1x, pH 7.4, Corning cellgro, USA), albumin 10 ⁻² g/L ~ 35 g/L, 30 mL, 37 °C PBS (1x, pH 7.4, Corning cellgro, USA), albumin 10 ⁻² g/L 30 mL, 37 °C	Decreases with the concentration of Si(OH) ₄	[56]
Cations	Lightly p-doped 10 ¹⁵ cm ⁻³ , 200 nm thickness on SiO ₂ /Si substrate	(molar ratio 19.8/80.2, Sigma-Aldrich, USA), Phosphate & chloride 0.05 ~ 1 M, pH 7.5, 37 °C PBS (1x, pH 7.4, Corning cellgro, USA), NaCl, CaCl ₂ , MgCl ₂ 0 ~ 1 mM, 30 mL, 37 °C PBS (1x, pH 7.4, Corning cellgro, USA), albumin 10 ⁻² g/L ~ 35 g/L, 30 mL, 37 °C PBS (1x, pH 7.4, Corning cellgro, USA), albumin 10 ⁻² g/L 30 mL, 37 °C	Increases with the concentration of cations	[56]
Protein (albumin)	Lightly p-doped 10 ¹⁵ cm ⁻³ , 200 nm thickness on SiO ₂ /Si substrate	(molar ratio 19.8/80.2, Sigma-Aldrich, USA), Phosphate & chloride 0.05 ~ 1 M, pH 7.5, 37 °C PBS (1x, pH 7.4, Corning cellgro, USA), NaCl, CaCl ₂ , MgCl ₂ 0 ~ 1 mM, 30 mL, 37 °C PBS (1x, pH 7.4, Corning cellgro, USA), albumin 10 ⁻² g/L ~ 35 g/L, 30 mL, 37 °C PBS (1x, pH 7.4, Corning cellgro, USA), albumin 10 ⁻² g/L 30 mL, 37 °C	Decreases with the concentration of albumin	[56]

(continued on next page) [39]

Table 1 (continued)

Factors	Silicon	Solution	Dissolution rate	Refs.
Doping concentration	p- and n-doped 10 ¹⁷ cm ⁻³ / 10 ¹⁹ cm ⁻³ / 10 ²⁰ cm ⁻³ , ~ 100 nm thickness on SiO ₂ /Si substrate	PBS (1 M, pH 7.4, Sigma-Aldrich, USA), pH 7.4, 37 °C	Decreases with the doping concentration	
	Polycrystalline Si(poly-Si)/ amorphous Si(a-Si), 100 nm thickness on SiO ₂ /Si substrate	Phosphate buffer solution (0.1 M, Sigma-Aldrich, USA), pH 7.4, 37 °C	Poly-Si : 2.8 nm/day a-Si : 4.1 nm/ day	[35]
Crystal structure				

concentrations of Si(OH)₄ move the equilibrium to the reverse reaction-dominant side in the hydrolysis Si + 4H₂O ⇌ Si(OH)₄ + 2H₂ [56]. Recent research shows that increasing the Si(OH)₄ concentration from 0 to 200 ppm decreases the dissolution rate from 5 to 0.5 nm/day for highly doped Si in PBS at 37 °C [56]. Notably, the change in dissolution rate is non-negligible even in solutions at the saturation level of Si(OH)₄ when Si(OH)₄ starts to polymerize to SiO₂ because Si hydrolysis is faster than conversion of Si(OH)₄ to SiO₂ [56].

Although OH⁻ is a major species in changing dissolution rates, other anions like phosphate and chloride, very common ions in biofluids, also affect dissolution behavior through adsorption and nucleophilic attack of silicon surface bonds. The dissolution behavior of Si NM of thickness 320 nm in phosphate buffer solution (molar ratio 19.8/80.2, pH 7.5, Sigma-Aldrich, USA) and buffered chloride solution of 0.05–1 M is summarized in Fig. 2D [38]. The dissolution rate increases with increasing ion concentration in both solutions [38]. The reaction rate is proportional to the fourth root of the ion concentration, as with OH⁻ [38]. Modifying Eq. (3) yields:

$$R = k_0 [H_2O]^4 [OH^-]^{1/4} [PO_4^{3-}]^{1/4} e^{-E_a/kT} \quad (4)$$

$$R = k_0 [H_2O]^4 [OH^-]^{1/4} [Cl^-]^{1/4} e^{-E_a/kT} \quad (5)$$

Here k₀ is 2480 μm/h × (mol/L)^{-4.5}, as in silicon etching in alkaline solution, and E_a varies from 0.64–0.84 eV by depending on the concentration [38]. The dissolution rates in phosphate solutions are faster than in chloride solutions at low concentrations, especially at 0.1 M concentration, whereas they are similar after 0.5 M concentration [38]. Modeling based on density-functional theory (DFT) confirms that the nucleophilic attack by anions like OH⁻, HPO₄²⁻, and Cl⁻ weakens the interior bonds of the silicon surface and increases susceptibility to further anion attack (Fig. 2E) [38]. E_{bonding} is calculated by E_{Si+Ion} – (E_{Si} + E_{Ion}), where E_{Si+Ion} is the total energy of the silicon with bonded anions and E_{Si} and E_{Ion} are the energies of the isolated silicon and anion, respectively. E_{bonding} computed by DFT shows a bonding tendency of OH⁻ > HPO₄²⁻ > Cl⁻, and confirms that Si(OH)₄ is more energetically stable than other ion-silicon complexes. [38] The elongation in the computed lengths of the interior bonds caused by anion adsorption is consistent with the weakening in bond strength [38]. The result that dissolution in pH 8.5 aqueous solution (~10 nm/day) is faster than in pH 7.5 with Cl⁻ 0.1 M aqueous solution (6.5 nm/day) confirms that OH⁻ has a greater effect on dissolution rate than other anions, since dissolution rate is more affected by increasing concentration of OH⁻ even when the increase in concentration of Cl⁻ is much larger [34,38].

Cations and proteins in common biofluids are additional factors in silicon dissolution kinetics, though their influence is much weaker than that of anions. Cations deprotonate the silanol group formed by

adsorption of water to the Si surface, thereby enhancing the reactivity of the siloxane group [56]. Fig. 2F shows the dissolution behavior of a Si NM of thickness 200 nm in 1 mM of CaCl₂, MgCl₂, and NaCl in protein-containing PBS (1x, pH 7.4, Corning cellgro, USA). [56] Increasing cation concentrations accelerate the dissolution rate regardless of cation type [56]. Ca²⁺ shows a faster dissolution rate than other cations because it has the greatest ability to deprotonate the silanol group and much lower activation energy for water rearrangement at the silicon surface [56,57]. Monovalent cations in the aqueous solution also affect the dissolution kinetics of Si NMs. Fig. 2G shows the dissolution rate of Si NM with different monovalent cations species. The dissolution rate of Si NM is higher in the solution containing K⁺ than in the solution containing Na⁺ at the same concentration and Si NM dimension. [58] A nucleophilic attack by anions to Si/solution interface that weakens Si interior bonds is promoted in solutions containing K⁺, as K⁺ has a higher frequency of solvent exchange rate than Na⁺ (Na⁺ and K⁺ is 109.0 and 109.2, respectively), resulting in more active exchange of cations with other anions in aqueous solution [58].

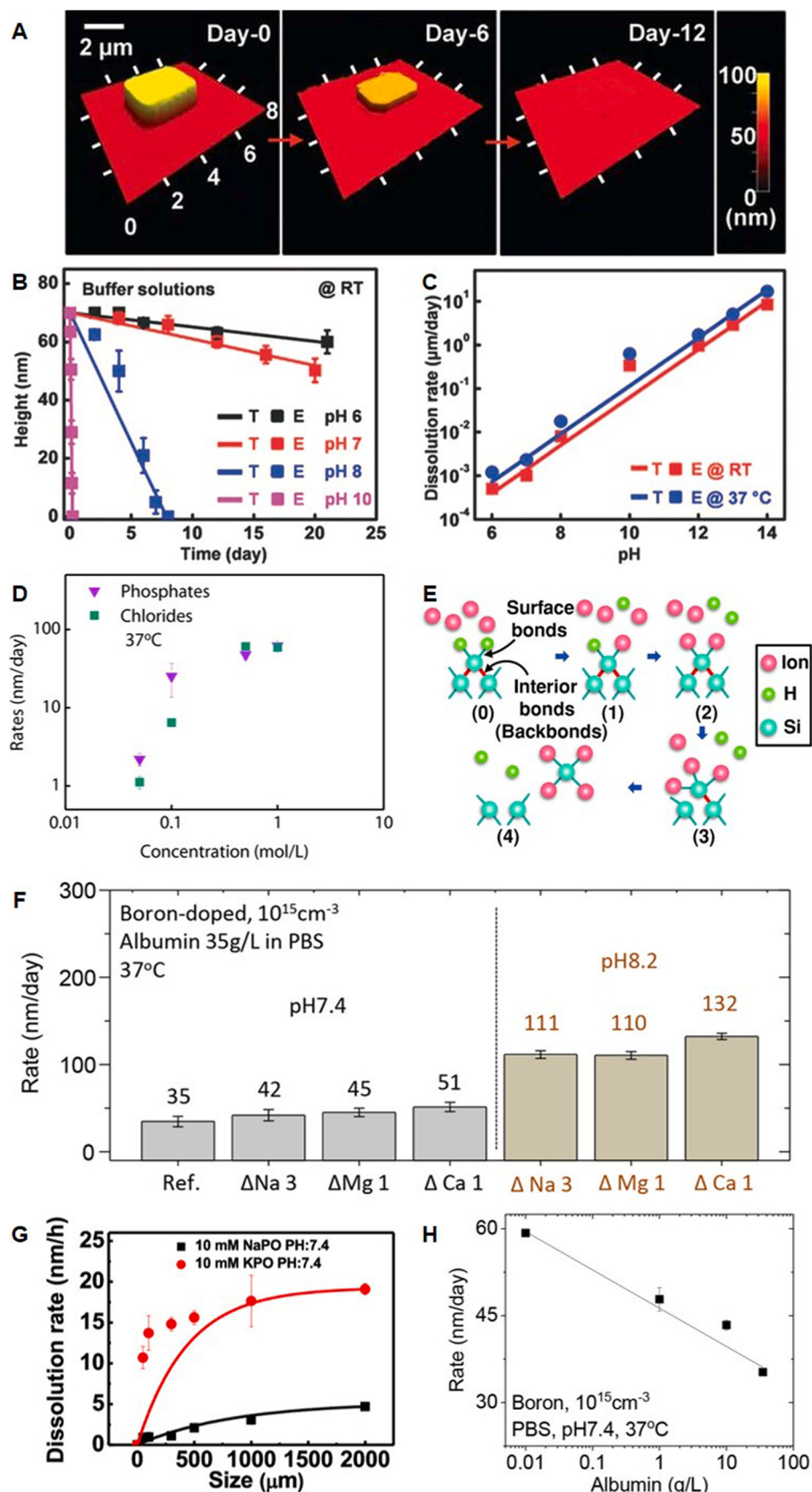
Proteins, a common species in biofluids, have a wide range of concentrations, between 10⁻² to 10² g/L (~80 g/L in blood, ~20 g/L in interstitial fluids, 0.1–1 g/L in saliva and aqueous humor, 0.01–0.1 g/L in urine) [56]. Fig. 2H shows the dissolution kinetics of a Si NM of thickness 200 nm in PBS (1x, pH 7.4, Corning cellgro, USA) with different concentrations of albumin, among the most common proteins in blood plasma [56]. The dissolution rate decreases with increasing albumin concentration because protein adsorption on the silicon surface limits the diffusive access of water to the silicon surface [56]. Biofluids contain several species including all the factors above such as anions, cations, proteins, and others [34,56]. Dissolution tests in bovine serum (Sigma-Aldrich, USA), a representative biofluid, yield practical dissolution rates in biofluids with complex combination of substances. The dissolution rates of 70 nm thick Si NM in bovine serum are ~1.6 nm/hour and ~4.2 nm/hour at RT and 37 °C, respectively, faster than any other solutions with a single environmental factor [34].

2.1.2. Effect of doping concentrations and microstructure on dissolution kinetics

Intrinsic factors of silicon such as doping concentrations and microstructures also play key roles in dissolution behavior. Doping of silicon has a strong effect on dissolution rate. Fig. 3A shows that the dissolution rate decreases slightly when the doping concentration increases to 10¹⁹ cm⁻³ and decreases significantly above 10²⁰ cm⁻³ in pH 7.4 PBS (0.1 M, pH 7.4, Sigma-Aldrich, USA) at 37 °C for both p- and n-doped Si NMs [39]. The strong reduction in dissolution rate at high doping concentrations is similar to the etch-stop phenomenon in anisotropic etching in KOH [59]. Two possible hypotheses describe the etch stop of doped Si in anisotropic etching: mechanically enhanced interatomic bonding due to a high doping concentration, and chemically blocked dissolution due to formation of a stable surface-oxide passivation layer through a barrier-less oxidation pathway by lattice strain induced by the different atomic sizes of dopants and silicon [59]. The etch-stop phenomenon is prominent in the anisotropic etching of boron-doped silicon, since the increase in hole concentration reduces the lifetime of the injected electrons through recombination, and formation of boron oxides and hydroxides decelerates dissolution [39,59]. The dependence of dissolution rate and doping concentration in Fig. 3A is expressed by

$$R = \frac{R_i}{1 + (C/C_0)^4} \quad (6)$$

which is modified from anisotropic etching under high pH [39,59]. The dissolution rate remains almost constant (R_i) until the doping concentration reaches a critical concentration C₀; a sharp decrease in dissolution rate occurs above C₀. The value of R_i varies according to environmental factors, while C₀ remains mostly unchanged at

**Fig. 2.** Dissolution kinetics of Si NM.

(A) Series of atomic force microscope (AFM) images of a Si NM showing continuous dissolution during immersion in PBS at 37 °C. Adapted with permission from References [15]. © 2012, American Association for the Advancement of Science (B) Dissolution kinetics of Si NMs (70 nm thick) in buffer solution of different pH at room temperature illustrated by thickness change (pH 6, black; pH 7, red; pH 8, blue; pH 10, purple) (theoretical, line; experimental, symbols). Adapted with permission from References [34]. © 2014 WILEY-VCH Verlag GmbH & Co. KGaA, Weinheim (C) Summarized dissolution kinetics of Si NMs depending on pH and temperature of aqueous buffer solutions at different temperatures. (room temperature, red; 37 °C, blue) (theoretical, line; experimental, symbols). Adapted with permission from References [34]. © 2014 WILEY-VCH Verlag GmbH & Co. KGaA, Weinheim (D) Anion concentration-dependent dissolution of Si NM at 37 °C (phosphate, purple; chloride, cyan). Adapted with permission from References [38]. © 2015 WILEY-VCH Verlag GmbH & Co. KGaA, Weinheim (E) Mechanism of Si(OH)₄ formation with anions at atomic-bond level based on DFT modeling. (0) initial state, (1) first ion adsorption and breakage of Si—H bonds in surface Si atoms, (2) second ion adsorption, (3) third ion adsorption and breakage of Si—Si bonds, (4) final ion adsorption and detaching of surface Si atoms as a form of Si(OH)₄. Adapted with permission from References [38]. © 2015 WILEY-VCH Verlag GmbH & Co. KGaA, Weinheim (F) Dissolution rates of Si NMs (doped with boron) depending on cation concentrations in phosphate buffer solution with albumin of 35 g/L and pH 7.4 at 37 °C. Adapted with permission from References [56]. © 2017, American Chemical Society (G) Dissolution kinetics of Si NMs (p-typed (boron), 10¹⁷ cm⁻³, (100, 200 nm thick) depending on the types of cations with the same phosphate concentration. Adapted with permission from References [58]. © 2019, American Chemical Society (H) Effect of protein concentration (albumin) on dissolution of Si NM (doped with boron) in phosphate buffer solution with pH 7.4 at 37 °C. Adapted with permission from References [56]. © 2017, American Chemical Society (For interpretation of the references to colour in this figure legend, the reader is referred to the web version of this article.).

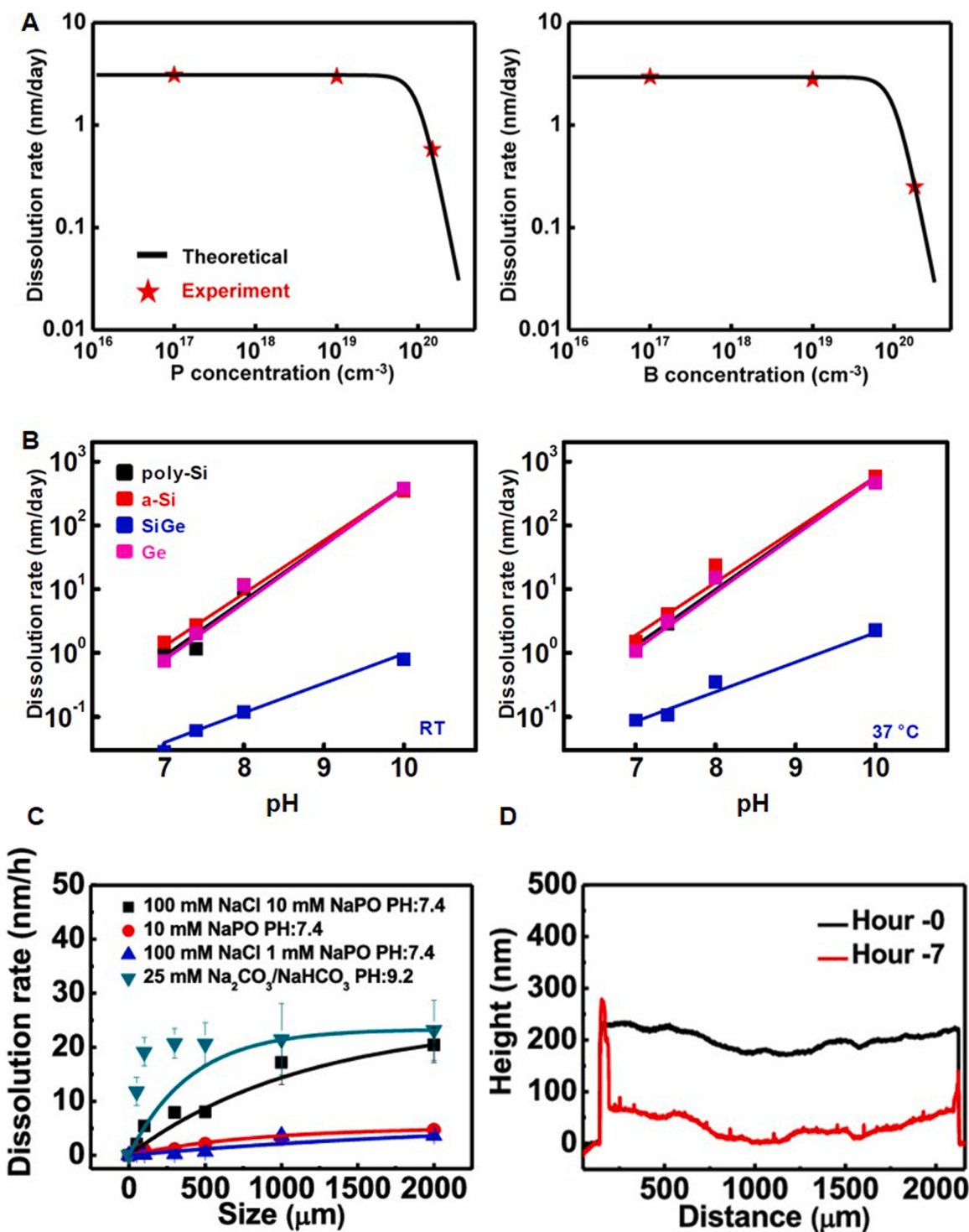


Fig. 3. Effect of microstructure on Si NM dissolution kinetics.

(A) Dissolution kinetics and etch-stop effect in Si NMs at different doping concentration (phosphorus, left; boron, right) (calculated, lines; measured, stars). Adapted with permission from References [39]. © 2014, American Chemical Society (B) pH-dependent dissolution kinetics for poly-Si (black), a-Si (red), SiGe (blue) and Ge (magenta) at room temperature (left) and 37 °C (right) (theoretical, lines; experimental, symbols). Adapted with permission from References [35]. © 2015, American Chemical Society (C) Dissolution kinetics of Si NMs (p-type (boron), 10^{17} cm^{-3} , (100), 200 nm thick) depending on dimensions of Si NMs in various types of saline-buffered solutions at 37 °C. (100 mM NaCl + 10 mM NaPO with pH 7.4, black; 10 mM NaPO with pH 7.4, red; 100 mM NaCl + 1 mM NaPO with pH 7.4, blue; 25 mM $\text{Na}_2\text{CO}_3/\text{NaHCO}_3$, cyan) (theoretical, line; experimental, symbols). Adapted with permission from References [58]. © 2019, American Chemical Society (D) the height profiles of Si pad ($2000 \times 2000 \mu\text{m}$) at two stages of hydrolysis in bicarbonate-buffered solutions (pH 9.2) at 37 °C (0 h, black; 7 h, red). Adapted with permission from References [58]. © 2019, American Chemical Society (For interpretation of the references to colour in this figure legend, the reader is referred to the web version of this article.).

$\sim 10^{20}$ cm $^{-3}$ [39].

Silicon's crystal structure also affects the dissolution behavior. Fig. 3B shows the dissolution behavior of polycrystalline Si (poly-Si) and amorphous Si (a-Si) of thickness 100 nm in an phosphate buffer solution (0.1 M, Sigma-Aldrich, USA) with pH 7–12 at RT and 37 °C [35]. The dissolution rates of poly-Si and a-Si at pH 7.4 and 37 °C are 2.8 nm/day and 4.1 nm/day, respectively. While the dissolution rate of poly-Si is similar to that of mono-Si (2.9 nm/day), a-Si dissolves faster because its low density leads to an enhancement in water penetration [35]. Similarly, the dissolution rate of porous Si is much greater than that of crystalline Si, depending on the porosity and pore size of Si [60]. The dissolution rates of both poly-Si and a-Si depend on pH and temperature, as with mono-Si. However, the proportionality to OH $^-$ is different, and a modified equation has been proposed [35]:

$$R = k_0 [H_2O]^4 [OH^-]^x e^{-E_a/kT} \quad (7)$$

The values of x determined from fitting data were 0.874 and 0.865 for poly-Si and a-Si, respectively, with the same k_0 as mono-Si [35].

The dimension of Si NM is another crucial factor affecting the dissolution rate of Si. Fig. 3C shows the dissolution kinetics of Si NMs with various dimensions of 2000 × 2000 μm, 1000 × 1000 μm, 500 × 500 μm, 300 × 300 μm, 100 × 100 μm, and 50 × 50 μm in diverse types of saline-buffered solutions [58]. The dissolution rates of Si NMs in all aqueous solutions increase as the dimensions of Si NMs increase [58]. Fig. 3D shows the thickness profiles of the Si pad (2000 × 2000 μm) with different immersion times in bicarbonate-buffered solutions (pH 9.2) at 37 °C [58]. The dissolution rate at the edge is much slower than at the center because the edge area reacts more sensitively to local perturbation [58]. The area occupied by the edge in the square increases as the square size of Si NM decreases; thus, the influence of the edge area on dissolution kinetics increases, resulting in slower dissolution rates [58].

2.1.3. Biocompatibility of electronic-grade silicon

The biocompatibility of Si is the important factor in applying Si transient electronics in biodegradable medical electronics and environmentally friendly devices. Extensive research on silicon biocompatibility has been performed using porous silicon, which is widely used for drug delivery vehicles [61–63]. The main dissolution product of silicon is Si(OH)₄, the most common form of nontoxic and bioavailable silicon in the human body [63]. Si(OH)₄ does not accumulate in the body; rather, it is absorbed along the gastrointestinal tract after dissolution and excreted via the urinary pathway [63]. However, reactive oxygen species (ROS) are also formed as byproducts of hydrolysis [63]. ROS can induce cell damage in abnormally large concentrations, so their effect is closely related to amounts and degradation rates, which mainly depend on the size of porous silicon particles [63]. Particles of 3–25 μm are cytotoxic to monocytes, but particles smaller than 1 μm show no cytotoxic effects on lymphoma cells, macrophages, and endothelial cells [63].

Research has also confirmed the biocompatibility of porous Si in in-vivo inflammation studies using animal models [63]. Porous silicons of size less than 1 μm accumulate within the liver and spleen after insertion into mice, but they are removed over four weeks with no morphological changes [63]. The levels of the enzyme lactate dehydrogenase (LDH), used to indicate tissue damage, did not increase except for multiple administrations of particles [63]. Also, in-vivo biocompatibility of porous silicon membranes was investigated using a mouse model [63]. Nanostructured porous silicon membrane of pore size 40–60 nm was implanted in rat conjunctiva [63]. Inflammatory response occurred with a very thin fibrous capsule wrapping around the implant [63]. Inflammatory cells formed only in a very small area around the implant, and tissue erosion or inflammatory cytokine were also not observed [63]. Similar results were obtained in a study of inserting porous silicon membrane into mouse sciatic nerve tissue and abdominal wall [63]. Because of the excellent biocompatibility of porous silicon, porous

silicon is emerging as an option for delivery of various drugs with no adverse effects, beginning with delivering insulin by a porous silicon layer across a Caco-2-cell monolayer [61,63].

Many researchers expected Si NMs would have excellent biocompatibility, since porous silicon is regarded as a biocompatible implant in small amounts even though it dissolves more aggressively than Si NMs [63]. Hwang et al. demonstrated the biocompatibility of Si NMs at the cell level by culturing a metastatic breast-cancer-cell line on a patterned array of Si NMs to analyze the growth and spread of cells and the dissolution of Si NM [39]. Fig. 4A shows images of cell proliferation and dissolution of patterned Si dots [39]. The Si dot pattern dissolved within 4 days and the concentrations of living cells increased significantly after 10 days [39]. No cytotoxic effects of a high concentration of ROS were observed, since the dissolution rate of Si NMs is much lower than that of porous Si [39]. The concentration of dead cells increased between days 5 and 10, likely due to natural cell death as the cell culture reached confluence [39]. These results confirmed that Si and its dissolution byproducts have no adverse effects on cell viability [39].

Hydrogen evaluation is another consideration in biocompatibility. Numerous studies have shown that abnormal accumulation of hydrogen gas in tissue cavities causes infection from local blood clotting or cystic subcutaneous foam. [64] The issue of hydrogen accumulation was more critical for pure Mg due to its fast corrosion rate (0.3 μm/h in DI water at RT), but hydrogen generation did not act as a toxic factor by controlling the corrosion rate through alloying as hydrogen diffused into the surrounding tissues without accumulation [37,65,66]. The degradation rate of Si NM is 2 nm/day in mild pH PBS at RT, well below that of Mg AZ31B alloy (0.08 μm/h in DI water at RT [15,37].

In-vivo histology and immunochemistry tests of Si NMs have also been conducted [34,39]. In-vivo evaluation by inserting a simple transient device with Si NMs (~100 nm thick) on a silk substrate into the subdermal tissue of BALB/c mice showed that the implants completely disappeared after 5 weeks with no significant inflammatory response in the subdermal area, silk film, and muscle layers [39]. Fig. 4B shows results in immune response and tissue inflammation testing by hematoxylin and eosin (H&E) staining for five weeks by inserting high-density polyethylene (HDPE) as control materials on the left-side dorsal skin and a transient electronic material on the right-side dorsal skin [39]. No serious complications occur as compared to the HDPE control with compatible levels of immune cells [39]. There are no significant differences in CD4+, CD8 + T cell and B cell concentrations in peripheral vascular lymphocytes and draining lymph nodes (DLNs) (Fig. 4C) [34]. Furthermore, the serum concentrations of pro-inflammatory cytokines (IL-6, IL-10, MCP-1, IFN-γ, TNF-α, IL-12p70) do not change significantly [34].

In-vivo tracking of Si provides an improved understanding of the biocompatibility of silicon inside the body. Fig. 4D shows the Si concentration in mouse blood, brain, heart, kidney, liver, lung, muscle, and spleen tissues after implanting biodegradable devices including Si NMs (1500 nm thick) on a ~10-μm-thick PLGA substrate measured with inductively coupled plasma optical emission spectrometry (ICP-OES) and inductively coupled plasma mass spectrometry (ICP-MS) [67]. No abnormal accumulation was observed over seven weeks of implantation compared with the control group (no implantation) [67]. The concentrations of Si in blood, heart, muscle and spleen cells increase for the first three weeks, but then slowly decrease and recover their original level by seven weeks [67]. Renal clearance to maintain metabolic balance of Si is observed through an increased Si concentration in the kidneys [67]. Histological images of each organ after five weeks in the experimental and control group show no local necrosis or inflammation in important organ tissues [67].

2.2. Other inorganic semiconductors

Other inorganic transient semiconductors with different mobilities and bandgaps from Si offer expanded application opportunities in active

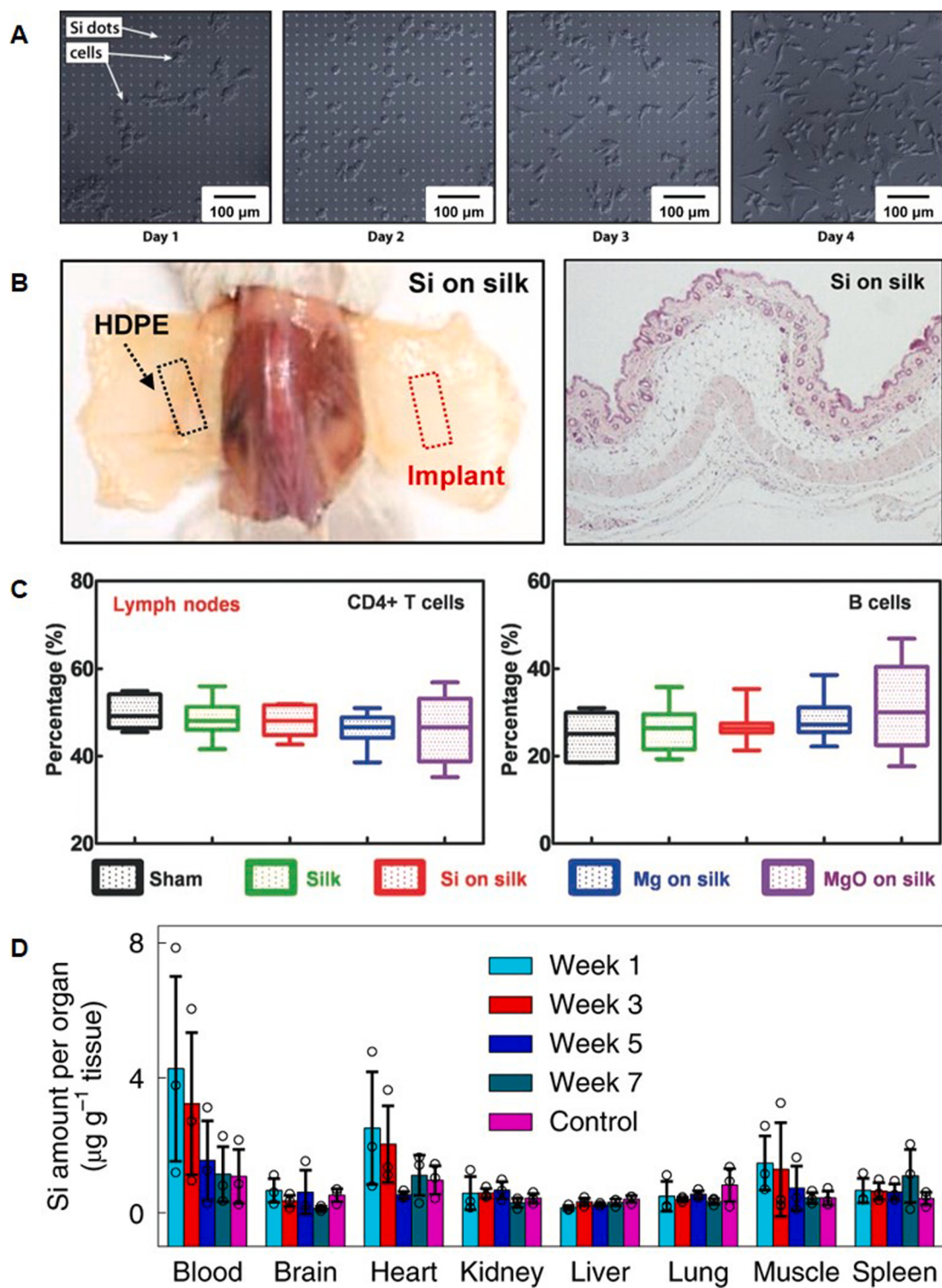


Fig. 4. In-vitro and in-vivo biocompatibility studies of Si NMs.

(A) Differential interference contrast images indicating cell viability with a Si NM array over four days. Adapted with permission from References [39]. © 2014, American Chemical Society (B) Implantation site (subdermal dorsal region) of Si/silk transient device and HDPE control sample (left) and H&E staining image after five weeks from implantation for BALB/c mice. Adapted with permission from References [39]. © 2014, American Chemical Society (C) Immunoprofiling of biocompatibility by concentrations of CD4 + T cells and B cells in lymph nodes of mice five weeks from implantation (sham, black; silk, green; Si on silk, red; Mg on silk, blue; MgO on silk, purple). Adapted with permission from References [34]. © 2014 WILEY-VCH Verlag GmbH & Co. KGaA, Weinheim (D) Variation of Si concentration in blood and major organs (brain, heart, kidney, liver, lung, muscle, and spleen tissues) after implantation of a transient photodetector built using Si NM (1500 nm thick), Zn electrodes (400 nm thick), SiO₂ interlayer (~50 nm thick), and PLGA (10 μm) substrate measured by inductively coupled plasma optical emission spectrometry (ICP-OES) and inductively coupled plasma mass spectrometry (ICP-MS) for seven weeks. Adapted with permission from References [67]. © 2019, The Author(s), under exclusive license to Springer Nature Limited For interpretation of the references to colour in this figure legend, the reader is referred to the web version of this article.).

transient electronics. Ge, used in high-frequency devices, is a representative example with small bandgap and large minority-carrier mobility [35]. Ge has two hydrolysis mechanisms depending on the presence of dissolved oxygen: [35,68]



Direct interaction of Ge without oxygen by Eq. (8) proceeds at a negligible rate, so hydrolysis in the presence of dissolved oxygen mainly follows Eq. (9) [35,68]. Fig. 5A shows the dissolution behavior of a 100-nm-thick Ge film in phosphate buffer solution (0.1 M,

Sigma-Aldrich, USA) at different pH and temperatures. The dependency on pH and temperature is similar to that of Si. The dissolution rate of Ge film in pH 7.4 and 37 °C is 3.1 nm/day, slightly faster than the mono-Si (2.9 nm/day), since the activation energy for Ge dissolution (~0.52 eV) is slightly below that of mono-Si (~0.59 eV) [35].

The alloy SiGe is also attractive as a transient semiconducting material with additional flexibility in band-gap tuning. Figs. 5B describe the change in dissolution rate of 30-nm-thick SiGe (Si_8Ge_2) in an phosphate buffer solution (0.1 M, Sigma-Aldrich, USA) at different pH and temperature. [35] Dissolution of SiGe occurs uniformly and the dissolution rate depends strongly on pH, just as in Si and Ge individually [34,35]. However, the dissolution rate of SiGe is much slower (0.1 nm/day) than

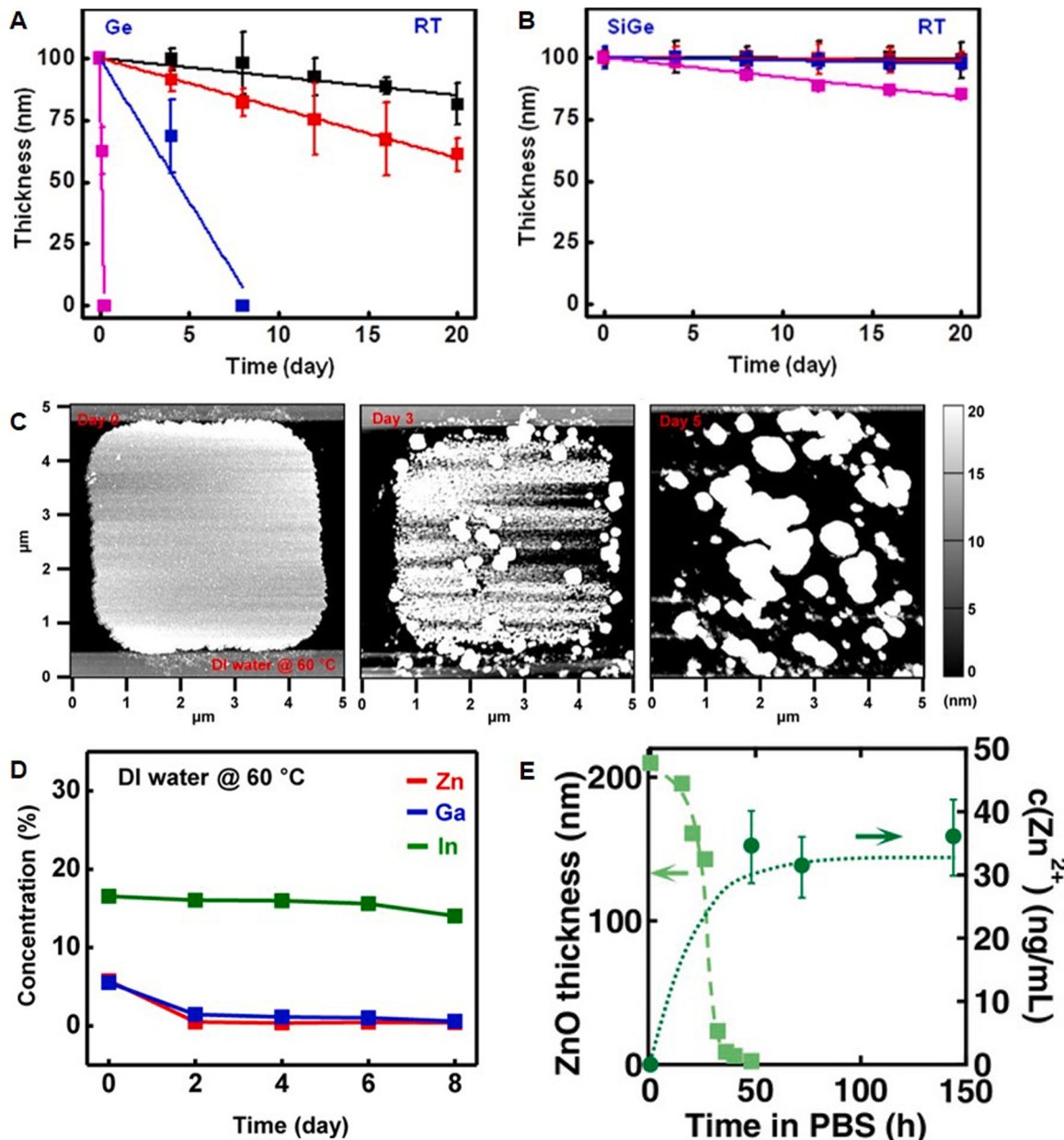
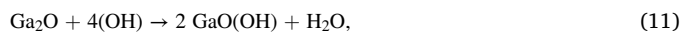
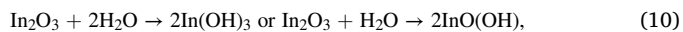


Fig. 5. Dissolution behaviors of other transient inorganic semiconductors.

pH-dependent dissolution kinetics of Ge (A) and SiGe (B) in aqueous buffer solutions at room temperature (pH 7, black; pH 7.4, red; pH 8, blue; pH 10, magenta) (calculated, lines; measured, squares). Adapted with permission from References [35]. © 2015, American Chemical Society (C) Non-uniform dissolution of a-IGZO observed by AFM topography during dissolution in DI water at 60 °C. Adapted with permission from References [70]. © 2015, American Chemical Society (D) Variation in atom composition measured by XPS explaining non-uniform dissolution by different dissolution rates of individual atoms during dissolution in DI water at 60 °C (Zn, red; Ga, blue; In, green). Adapted with permission from References [70]. © 2015, American Chemical Society (E) Thickness change of ZnO by dissolution in PBS at 37 °C and concentration variation of Zn^{2+} as a byproduct of dissolution. Adapted with permission from References [72]. © 2019 WILEY-VCH Verlag GmbH & Co. KGaA, Weinheim (For interpretation of the references to colour in this figure legend, the reader is referred to the web version of this article.).

that of mono-Si or Ge (2.9 nm/day and 3.1 nm/day, respectively) in phosphate buffer solution at pH 7.4 and 37 °C; this is consistent with the etching kinetics in high-alkaline solutions, where the etching rate is ~100 times smaller than that of mono-Si [35,69]. Lattice mismatch in the Si-Ge interface induces band bending, which results in increased hole supply yielding an etch-stop through recombination of injected electrons [69]. Increases in the Ge concentration in the alloy decrease the hole barrier at the Si-Ge and solution interfaces and enable the formation of a passivating oxide at the surface [69]. As a result, the activation energy for dissolution of Si-Ge alloy (~0.76 eV) is much greater than that of mono-Si (~0.59 eV), and the dissolution rate is much slower [35]. A SiGe epitaxial layer can be used as an etch-stop layer since the reduction in dissolution rate is similar to that of the etch-stop of heavily boron doped silicon [69].

a-IGZO is also attractive candidate as it is widely used in TFT technology such as active-matrix-display devices due to its excellent optical transparency, high mobility, low temperature deposition, and operational stability. [70] a-IGZO is an amorphous alloy of indium, gallium, and zinc oxide, and the components undergo different hydrolysis mechanisms to form their respective hydroxides: [70]



a-IGZO film shows irregular dissolution behavior, since a-IGZO is amorphous and the dissolution rates of each components differ. [70] Figs. 5C and 5D shows AFM images of a 35-nm-thick a-IGZO film during dissolution and the results of dissolution tests in deionized water (DI water) at 60 °C [70]. The AFM images for five days' immersion describe the slow dissolution of a-IGZO film and the isolated islands of residual materials, indicating non-uniform dissolution behavior [70]. The concentration changes show that dissolution of Zn and Ga oxides is much faster than that of In oxides; Zn and Ga almost dissolve within 2 days, while In oxide residues remain after 8 days [70]. Oxides dissolve much faster due to acceleration by other ions in bovine serum (K^+ , Na^+ , Cl^- , PO_4^{3-} , etc.); meanwhile, Zn and Ga oxides still dissolve faster than In oxide [70].

ZnO is another important transient semiconductor with wide and direct bandgap (~3.37 eV), a large exciton-binding energy (60 meV), and a strong piezoelectric response [71,72]. ZnO dissolves through the following hydrolysis reaction to form a slightly soluble hydroxide of $\text{Zn}(\text{OH})_2$ or completely soluble ion of Zn^{2+} :



depending on reaction conditions [71,72]. Fig. 5E shows the dissolution behavior of ZnO thin film (200 nm thick) obtained through pulsed layer deposition (PLD) on mono-Si(111) in PBS at pH 7.4 and 37 °C [72]. This ZnO film dissolved completely without residues after 48 h with an average dissolution rate of 4 nm/h [72]. Zn^{2+} can remain as a dissolution product of ZnO thin film since the initial amount of ZnO is small enough, as the saturated concentration of Zn^{2+} is much lower than the solubility of $\text{Zn}(\text{OH})_2$ around pH 7.4 and 25–50 °C (3.2–21 µg/mL, in Zn^{2+}) [72]. The dissolution rate gradually increases with immersion time because the surface roughness and related interface area with the surrounding solution increase with dissolution [72]. Hydrolysis at low pH proceeds through a new reaction:



which significantly increases the ZnO dissolution rate in PBS at pH 4.0 [71].

2.3. Dissolution kinetics of dielectrics

Biodegradable dielectrics are key materials for insulation, passivation and encapsulation in transient electronics [36]. Table 2 summarizes the studies of the dissolution kinetics of various dielectrics in mild aqueous solutions. In particular, silicon oxides and nitrides, which are widely used in thin-film electronics as gate dielectrics, passivating interlayers and vapor encapsulation, provide a wide range of dissolution timeframes and compatibility with well-developed fabrication processes [36]. Extensive geological studies of hydrolysis of quartz and silica support the chemistry and kinetics of dissolution of silicon dioxides (SiO_2) in alkaline solutions [73–75]. The following equation shows a dissolution chemistry of SiO_2 that is very similar to that of Si with initiation reaction of OH^- : [73]



The detailed dissolution mechanism starts with formation of $\sim\text{Si}-\text{OH}$ complex on the surface silica site by reaction with $\sim\text{Si}-\text{O}-\text{Si}\sim$ and H_2O ; then ionization of the $\sim\text{Si}-\text{OH}$ complex to a $\sim\text{Si}-\text{O}^-$ complex occurs as pH increases [57,73]. The $\sim\text{Si}-\text{O}^-$ complex forms an activated complex of $[(\text{nH}_2\text{O}) (\sim\text{Si}-\text{O}^-)]^*$ that eventually leads to detachment of the silicon atom [73]. The dissolution of amorphous silica follows a mechanism similar to that of quartz: surface deprotonation of the $\sim\text{Si}-\text{OH}$ complex leads to detachment of Si, with much higher dissolution rate [75]. The amorphous crystalline structure of silica (density 2.196 g/cm³) is the main cause of its faster dissolution than quartz (density 2.648 g/cm³) due to its porous structure [73–75]. Generation of small amounts of $\text{Si}(\text{OH})_4$ does not cause inflammation, so SiO_2 also has acceptable biocompatibility [36]. A biodegradable device including a thin layer of SiO_2 (~50 nm thick) implanted in the cerebral region of CD-1 female mice (Fig. 4D) with no local necrosis or inflammation of key organs (heart, kidney, lung and spleen) even after 5 weeks' implantation, indicating that SiO_2 has biocompatibility [67].

The different dissolution kinetics of quartz and silica suggests a microstructure-dependent dissolution kinetics for SiO_2 . Electronic-grade SiO_2 has a wide range of microstructures that depend strongly on deposition or growth method [36]. For example, thermally grown silicon oxides show high density compared to silicon oxides deposited by plasma-enhanced chemical vapor deposition (PECVD) and electron-beam evaporation (e-beam) [36]. Fig. 6A shows the wide range of dissolution behavior for SiO_2 : 100-nm films thermally grown in O_2 (tg-dry) and H_2O (tg-wet), and made by PECVD and e-beam in pH 7.4–12 aqueous buffer solution (Sigma-Aldrich, USA) at RT and 37 °C [36]. The dissolution rates of tg-dry, tg-wet, PECVD, and e-beam oxides

Table 2
Studies of dissolution kinetics of various dielectrics.

		Solution	Dissolution rate	Refs.
Silicon oxide	tg-dry	pH 7.4 aqueous buffer	0.01 nm/day	[36]
	tg-wet	solution (Sigma-Aldrich, USA), 37 °C	0.003 nm/day	
	PECVD		0.1 nm/day	
	e-beam		10 nm/day	
	LPCVD		0.16 nm/day	
Silicon nitride	HF	pH 7.4 aqueous buffer	0.85 nm/day	[36]
	PECVD	solution (Sigma-Aldrich, USA), 37 °C	0.85 nm/day	
	LF			
	PECVD			
		Aqueous solution with various pH	pH < 5 : proportional to $[\text{H}^+]$ pH > 7 : proportional to $[\text{OH}^-]$	
MgO				[79]
SOG	Cured at 300 °C	pH 7.4 PBS (Sigma-Aldrich, USA) at 37 °C	~50 nm/day	[81]
	Cured at 800 °C		~6 nm/day	

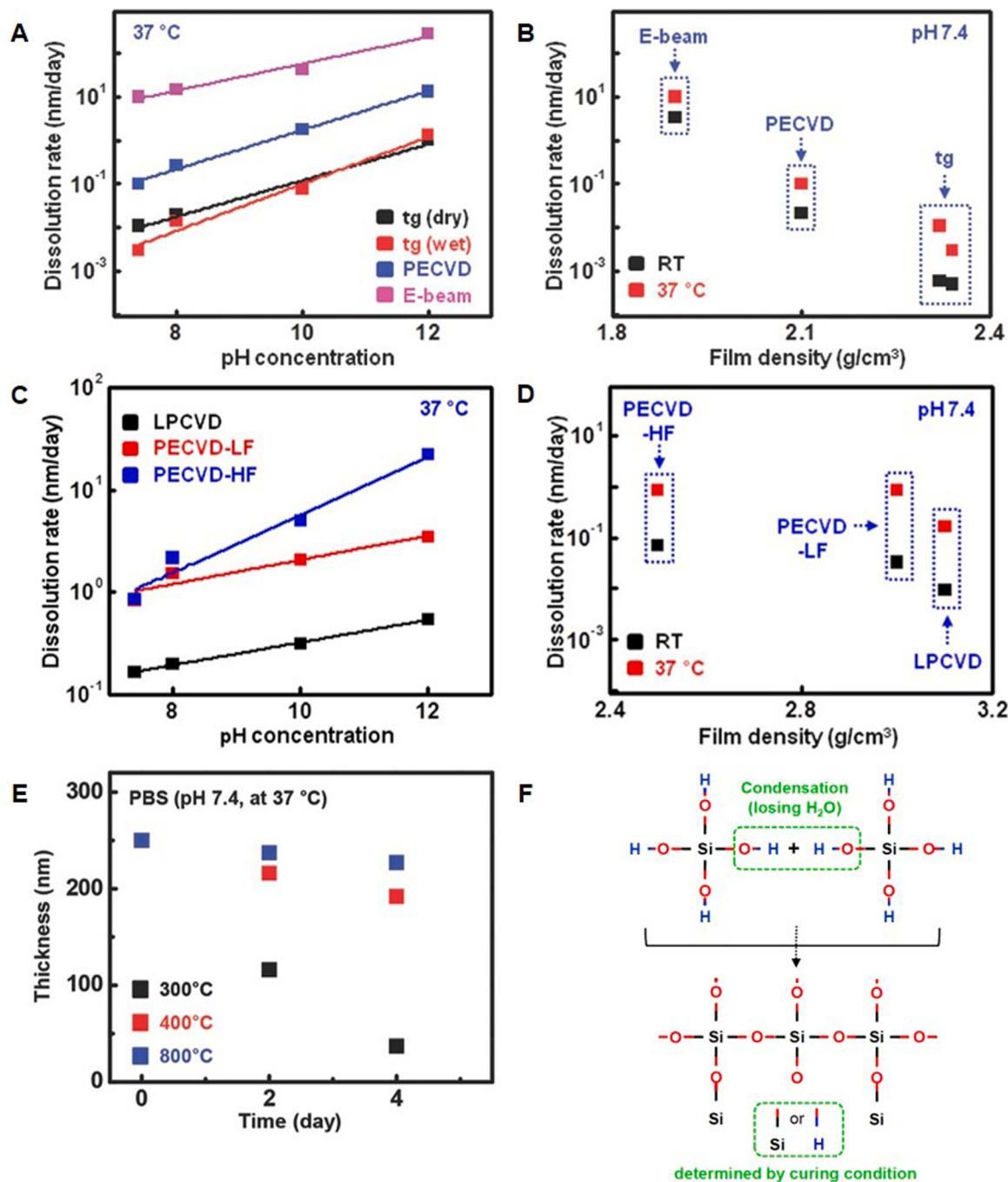


Fig. 6. Dissolution kinetics of Si-based dielectric materials depending on formation method.

(A) pH-dependent dissolution kinetics of silicon oxide formed by various methods during immersion in aqueous buffer solutions at 37 °C (thermal-grown oxide (dry oxidation), black; thermal-grown oxide (wet oxidation), red; PECVD oxide, blue; e-beam evaporation oxide, magenta). Adapted with permission from References [36]. © 2014 WILEY-VCH Verlag GmbH & Co. KGaA, Weinheim (B) Effect of density as determined by formation method on dissolution rate (room temperature, black; 37 °C, red). Adapted with permission from References [36]. © 2014 WILEY-VCH Verlag GmbH & Co. KGaA, Weinheim (C) Dissolution kinetics of silicon nitride formed by different fabrication methods and conditions in aqueous buffer solutions of different pH at 37 °C (LPCVD nitride, black; PECVD-LF nitride, red; PECVD-HF nitride, blue). Adapted with permission from References [36]. © 2014 WILEY-VCH Verlag GmbH & Co. KGaA, Weinheim (D) Effect of density on dissolution kinetics of silicon nitrides in aqueous buffer solutions at room temperature (black) and 37 °C (red). Adapted with permission from References [36]. © 2014 WILEY-VCH Verlag GmbH & Co. KGaA, Weinheim (E) Thickness variation in spin-on glass cured at different temperatures (300, black; 400, red; 800 °C, blue) during immersion in PBS at 37 °C. Adapted with permission from References [81]. © 2015 WILEY-VCH Verlag GmbH & Co. KGaA, Weinheim (F) Curing mechanism of SOG by condensation reactions at high temperature. Less cured SOG contains more -OH. Adapted with permission from References [81]. © 2015 WILEY-VCH Verlag GmbH & Co. KGaA, Weinheim (For interpretation of the references to colour in this figure legend, the reader is referred to the web version of this article.).

at pH 7.4 aqueous buffer solution (Sigma-Aldrich, USA) and 37 °C were 0.01, 0.003, 0.1, and 10 nm/day, respectively [36]. The film density is one of major factor affecting dissolution rate of oxides [36]. Fig. 6B shows the correlation between oxide film density and dissolution rate

[36]. Tg-dry and PECVD oxides have relatively high density (2.33 g/cm³, 2.10 g/cm³ respectively), while e-beam oxides have low density (1.90 g/cm³) [36]. The low-density e-beam oxide has a dissolution rate ~1000 times higher than tg-dry oxide [36]. Hydrolysis in

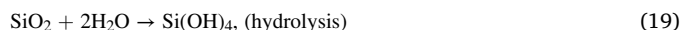
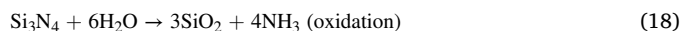
porous e-beam oxide is accelerated by an increase in the reactive surface area by enhanced water-molecule diffusion through the porous medium [36]. A modified reactive-diffusion model reflecting the initial density difference and increased diffusivity explains the density-dependent dissolution kinetics of SiO_2 , but the very much faster dissolution in e-beam oxides makes one suspect that other effects, such as nanoscale fragmentation, may be operative [36,40]. Oxide stoichiometry and bonding energy were also investigated to confirm their effects on dissolution kinetics [36]. tg-dry and PECVD oxides have a favorable stoichiometry of $\text{Si}: \text{O} = 1:2$, whereas e-beam oxides have a typically oxygen-rich stoichiometry ($\text{Si}: \text{O} = 1:2.2$) [36]. The bonding energies of tg-dry and PECVD oxides measured by X-ray photoelectron spectroscopy (XPS) are almost the same; that of the e-beam oxide is slightly smaller [36]. Density was considered a major factor in the dissolution kinetics in this study because the stoichiometry and bonding energy showed only small deviations [36]. In another study, SiO_2 of very low density and uniformity formed by polydimethylsiloxane (PDMS) calcination showed much faster dissolution, about $129 \pm 9 \text{ nm/day}$, supporting density-dependent dissolution kinetics [76].

The dissolution kinetics of silicon oxides are also variable with environment, such as temperature and ion species in solution [36]. Fig. 6A shows the dependence of dissolution rate of SiO_2 on pH [36]. The dissolution rate of each oxide mainly increases with pH since hydrolysis reactivity increases by the deprotonation of silanol groups on SiO_2 surface [73]. The dissolution rate has a linear relationship

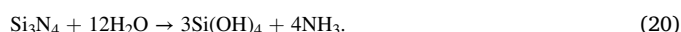
$$\log r = a + n[\text{pH}] \quad (17)$$

with pH, where r is the dissolution rate and a and n are constants [36]. The value of n varies from 0.31 to 0.44 at 37°C and 0.22 to 0.62 at RT (r is in $\text{mol m}^{-2} \text{s}^{-1}$) [36]. The dissolution rate also increases with temperature by an Arrhenius dependence [36]. Other ions also can affect the dissolution rate of SiO_2 [57]. Some representative anions such as Cl^- and HPO_4^{2-} accelerate dissolution, as in the case of silicon [77]. SiO_2 dissolves faster in solution with Na_2HPO_4 (NaPO) than NaCl because of the faster deprotonation of silanol groups by strong hydrogen-bonding interactions between phosphate and the SiO_2 surface [77]. Cations such as Ca^{2+} , Mg^{2+} , and Na^+ also accelerate SiO_2 dissolution and increase dramatically at high pH due to the stronger electrostatic interaction between the negatively charged SiO_2 surface and cation [77]. This interaction weakens the surrounding Si—O bonds, resulting in increased susceptibility to water attack, and the dissolution rate with Ca^{2+} is much faster, as in Si. The dissolution rate is significantly reduced as $\text{Si}(\text{OH})_4$ concentration increases, since the reverse hydrolysis reaction increases [77].

Silicon nitrides are also important dielectrics in transient electronics, with similar dissolution chemistry and kinetics to Si and Si oxides. Silicon nitrides undergo hydrolysis by two steps:



where the overall reaction is expressed as [36]



Silicon nitride has a degradation product of $\text{Si}(\text{OH})_4$, the same as silicon oxide, but also generates NH_3 [36]. Hepatic bile contains NH_3 with a concentration of 45–240 $\mu\text{mol/L}$, and a small amount of NH_3 is consumed by metabolism in the body without severe toxicity [78]. The dissolution kinetics of silicon nitride can be tuned by varying film density and stoichiometry by using different deposition methods and conditions, similar to silicon oxides [36]. Fig. 6C shows the dissolution behavior of silicon nitride produced by three deposition methods: low-pressure chemical vapor deposition (LPCVD), high-frequency PECVD (HF PECVD), and low-frequency PECVD (LF PECVD), in pH 7.4–12 aqueous buffer solution (Sigma-Aldrich, USA) at RT and 37°C

[36]. The dissolution rates of LPCVD and both types of PECVD nitride at pH 7.4 aqueous buffer solution (Sigma-Aldrich, USA), 37°C are ~ 0.16 , and $\sim 0.85 \text{ nm/day}$, respectively [36]. Here, LPCVD nitride has a high density of 3.1 g/cm^3 with a favorable stoichiometry of $\text{Si:N} = 3:3.9$, whereas HF and LF PECVD nitride have low densities of 2.5 g/cm^3 and 3.0 g/cm^3 with less favorable stoichiometry of $\text{Si:N} = 3:3.3$ and $\text{Si:N} = 3:4.3$, respectively [36]. The density of nitride is a major factor in dissolution rate, as in SiO_2 , so low-density PECVD nitride has a higher dissolution rate than high-density LPCVD nitride, where the less favorable stoichiometry of PECVD may also be a factor in dissolution (Fig. 6D) [36]. Since Si_3N_4 has SiO_2 as an intermediate product, the dissolution behavior according to pH is almost the same as that of SiO_2 with a linear dependence of $\log r = a + n[\text{pH}]$ ($n = 0.11$ to 0.28 for 37°C , 0.26 to 0.31 for RT) [36].

MgO is also used as a dielectric of transient electronics with faster dissolution rate than silicon oxides and nitrides [36,79]. The dissolution chemistry of MgO varies depending on pH [79,80]. At $\text{pH} < 5$, the reaction



is followed, while at $\text{pH} > 7$, the reaction



is followed [79]. Proton attack becomes a rate-determining step and the dissolution rate is proportional to $[\text{H}^+]$ at $\text{pH} < 5$, whereas at $\text{pH} > 7$, OH^- adsorption becomes a rate-determining step and the dissolution rate is proportional to $[\text{OH}^-]$ [79].

Spin-on glass (SOG) materials are also good candidates for transient dielectrics and passivation layers with good coverage on small patterns by filling gaps, pinholes and topographical features via a solution phase deposition approach. Fig. 6E and F shows the change in thickness of a SOG layer cured at three different temperatures, 300°C , 400°C and 800°C , in pH 7.4 PBS (Sigma-Aldrich, USA) at 37°C and the formation process of the silicate SOG followed by strong connection of Si—O—Si bonds by a condensation reaction between $\text{Si}(\text{OH})_4$ molecules at high temperature. Unreacted functional groups remain as Si—OH [81]. The reverse reaction of condensation corresponds to hydrolysis, so the presence of unreacted Si—OH increases the dissolution rate [81]. Curing time and temperature affect the portion of unreacted Si—OH and thus dissolution kinetics [81]. Fig. 6E shows that SOG cured at 300°C has the fastest dissolution rate of $\sim 50 \text{ nm/day}$, while SOG cured at 800°C has a relatively slow dissolution rate of $\sim 6 \text{ nm/day}$ [81]. Fourier-transform infrared spectroscopy (FT-IR) of SOG confirms that SOG cured at 300°C had the largest concentration of unreacted —OH groups [81]. SOG also has excellent biocompatibility as cell viability on days 1, 3, 6, and 9 through fluorescence-based live/dead assay while *in vitro* cell culture evaluations show that the dissolution product of SOG is not cytotoxic [81].

2.4. Biodegradable metals for transient electronics

Biodegradable metals with excellent conductivity and mechanical ductility are critically important as metal electrodes are essential in current collectors, interconnections, and electrocircuits in various electronic devices. Standard electrode potential (E) of metal is the most critical factor in determining whether metal is biodegradable, as the hydrolysis of biodegradable metals is an electrochemical reaction with water [82]. Fig. 7 shows the standard electrode potential of various metallic elements [82]. The metals with standard electrode potential less than hydrogen ($E^0 = 0 \text{ V}$) react electrochemically with water in an aqueous environment to degrade, and metals from Li to Pb in Fig. 7 correspond to these [82]. Furthermore, metals such as W, Bi and Cu with slightly positive standard electrode potentials can be dissolved in a specific environment [82]. For example, W has a positive standard electrode potential of 0.1 V, but oxygen-aided biodegradation proceeds

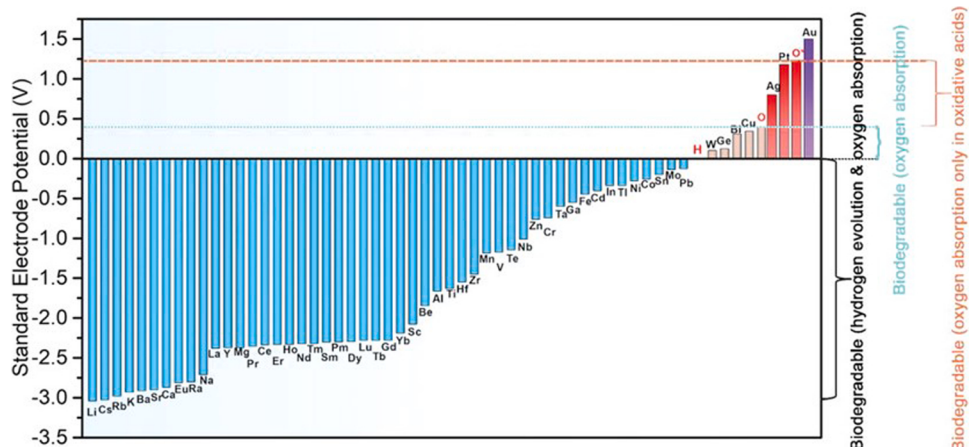


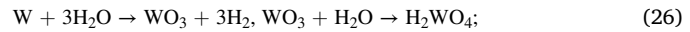
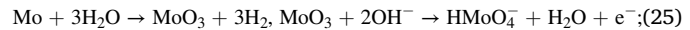
Fig. 7. Standard electrode potential of various metallic elements. (O* indicates standard electrode potential of O in an acidic environment). Adapted with permission from References [82]. © 2019 WILEY-VCH Verlag GmbH & Co. KGaA, Weinheim.

since the standard electrode potential of W is lower than O [82]. O has standard electrode potentials of 0.4 V in a neutral environment and 1.23 V in an acidic environment, so some metals such as Ag and Pt also dissolve in strong oxidative acid since the electrode potential of O is much higher [82]. The potentials of metals can be changed by various external factors such as alloying elements, environmental situations, surface states, absorbed gases, and mechanical stresses [82].

Many metals are biodegradable, but in order to be used as biodegradable conductors, metals also must have excellent biocompatibility and conductivity. Fig. 8 shows the amounts of various metals present in the body [82]. The biocompatible amount of metal depends mainly on the content in human body [82]. Major elements in the body such as Ca, Mg, Na and K are biocompatible, whereas trace elements such as Mn, Li, Mo, and W, can be problematic when used as primary components [82]. In particular, metals that are not present in the body can have serious adverse effects *in vivo* such as inappropriate accumulation or inflammatory aggregation [82]. However, since the scale of a thin film implantable device is very thin (~100 nm), trace elements (~mg in humans) also can be utilized as alloying elements [82]. Electrical conductivity is also required for use as a transient conductor [82]. Conductors used in electronics usually have conductivities of 10^4 to 10^7 S/m, and most biodegradable metals have conductivity large enough for use as conductors [37,82].

Mg, Zn, Mo, W, and Fe, are most commonly used as transient conductors as they demonstrate excellent biodegradability and biocompatibility among diverse biodegradable metals, and each undergoes

hydrolysis as shown in [37]



Dissolution of Fe proceeds by hydrolysis through many other reactions to form hydroxides (Fe(OH) , $\text{Fe}(\text{OH})_2$ or $\text{Fe}(\text{OH})_3$) or oxides (Fe_2O_3 , Fe_3O_4 or FeO), which leads to non-uniform dissolution due to the different solubility and hydrolysis rate of each oxide [37,83].

Yin et al. report a systematic dissolution study of electronic-grade Mg (300 nm thick), Zn (300 nm), W (150 nm), Mo (40 nm), Fe (150 nm), and an AZ31B thin film (300 nm) in DI water and Hanks' solution (H 8264, Sigma-Aldrich, USA) at RT and 37 °C [37]. The dissolution rate is analyzed by the electrical dissolution rate (EDR) to monitor electrical conductivity degradation as well as thickness change. EDR is defined as the change in electrical resistance R for an effective thickness h , according to [37]

$$R = R_0 h_0 / h, \quad (28)$$

where R_0 and h_0 are the initial electric resistance and initial thickness, respectively. Figures 9A – 9 F and Table 3 show the variation in

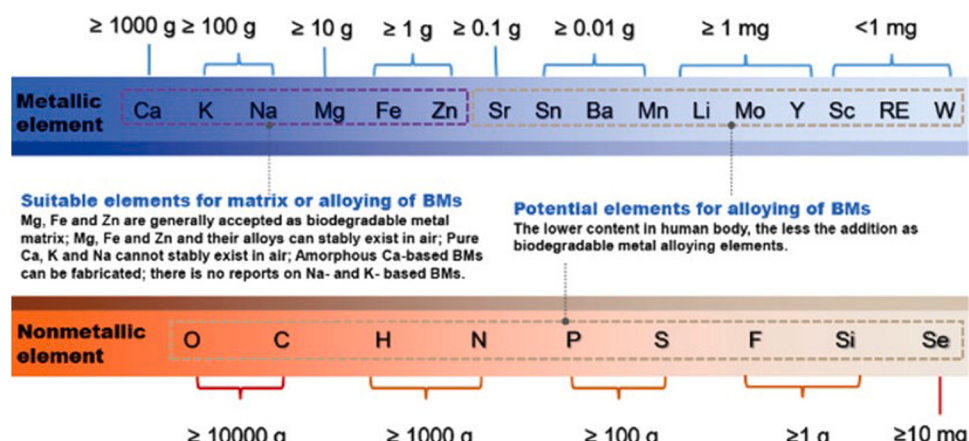


Fig. 8. Amounts of various biodegradable metals naturally present in the body. Adapted with permission from References [82]. © 2019 WILEY-VCH Verlag GmbH & Co. KGaA, Weinheim.

Table 3

Electrical and morphological dissolution rates of various metals in DI and Hanks' solution. Adapted with permission from References [37]. © 2013 WILEY- VCH Verlag GmbH & Co. KGaA, Weinheim.

	Electrical dissolution rates [$\mu\text{m h}^{-1}$]		Apparent morphological dissolution rates in DI water [$\mu\text{m h}^{-1}$]	Mass lost corrosion rates from literature [$\mu\text{m h}^{-1}$]
	DI	Hanks' solutions		
Mg	0.3 ± 0.1	4.8 ± 2.2	≈ 0.07	pH 7.4 SBF 37 °C: 0.05–0.5 0.05 M NaCl: 0.05–0.3 pH 7.4 SBF 37 °C: 0.02–0.1 0.05 M NaCl: ≈ 0.3 0.6 M NaCl: ≈ 0.1
AZ31B	0.08 ± 0.02	2.6 ± 2.1	≈ 0.02	
W (Sputter deposited)	$(4 \pm 1) \times 10^{-3}$	pH 5: $(1.4 \pm 0.4) \times 10^{-3}$ pH 7.4–8: $(8 \pm 2) \times 10^{-3}$ pH 7.4 37 °C: ≈ 0.02 pH 5: $\approx 2 \times 10^{-4}$ pH 7.4–8: $(7 \pm 2) \times 10^{-4}$ pH 7.4 37 °C: $\approx 2 \times 10^{-3}$ pH 5: $(6 \pm 2) \times 10^{-4}$ pH 7.4–8: $(2 \pm 0.3) \times 10^{-4}$ pH 7.4 37 °C: $(7 \pm 4) \times 10^{-4}$	$\approx 1.7 \times 10^{-3}$	pH 7.4 SBF: 0.02–0.06
W (CVD)	$(7 \pm 2) \times 10^{-4}$		$\approx 3 \times 10^{-4}$	
Mo	$(1 \pm 0.1) \times 10^{-3}$		$\approx 3 \times 10^{-4}$	pH 7 buffer: 1×10^{-3} pH 7 buffer thin film: 2×10^{-4} In vivo: $\approx 5 \times 10^{-3}$ DI water: $\approx 3 \times 10^{-3}$ Sea water: $\approx (2–8) \times 10^{-3}$
Zn	0.07 ± 0.02	0.3 ± 0.2	$\approx 7 \times 10^{-3}$	
Fe	$<1 \times 10^{-3}$	pH 5: $\approx 9 \times 10^{-3}$ pH 7.4–8: $\approx 2 \times 10^{-4}$ pH 7.4 37 °C: $\approx 7 \times 10^{-3}$	—	pH 7.4 SBF 37 °C: ≈ 0.02

resistance during dissolution and summarize results for EDR and morphological dissolution rate for the above six metals and alloy [37]. The dissolution kinetics of metals depends mainly on the formation of micropores or surface oxides, so microstructure change during dissolution was also investigated [37].

Fig. 9A and B show the dissolution kinetics of Mg and the AZ31B Mg alloy. The EDRs of Mg are about three times greater than that of AZ31B (0.3 and $0.08 \mu\text{m/h}$ in DI water at RT) [37]. In both cases, Mg(OH)_2 is the main dissolution product [37]. The EDRs in Hanks' solution are significantly higher than in DI water due to promotion of rapid attack by Cl^- [37]. There is a weak dependence on pH that is stronger in Hanks' solution [37]. The relatively fast dissolution kinetics of Mg and AZ31B are explained by changes in microstructures [37]. Fig. 9G shows the microstructural changes in Mg during dissolution in DI water [37]. Mg and the AZ31B Mg alloy seem to dissolve uniformly on a macroscopic scale; however, micropores develop at the microscopic scale that form needle-like dissolution products and accelerate water diffusion into materials [37]. In addition, a bi-layer surface structure composed of a thick Mg(OH)_2 rich outer layer on the thin crystalline MgO film appeared [37]. A surface oxide/hydroxide formed during dissolution decreases the rate of thickness change, but the oxides/hydroxides completely dissolve after 1–4 days, with relatively high solubility in water [37].

Fig. 9C describes the dissolution behavior of Mo [37]. Mo has a dissolution product of a Mo oxide mixture and a further soluble product [37]. OH^- is formed by oxygen reduction in the presence of dissolved oxygen by



and OH^- forms a soluble product of HMnO_4^- through the reaction in Eq. (25) [84]. Since the formation of Mo oxides is very important and oxygen is directly involved in the further reaction, the dissolution rate is closely related to oxygen solubility [37]. The EDRs of Mo are 2–5 times faster in DI water than in salt solutions at RT due to the strong dependence on oxygen solubility ($1 \times 10^{-3} \mu\text{m/h}$ in DI water at RT) [37]. The presence of ions such as Na^+ or Cl^- reduces oxygen solubility, so the dissolution rate decreases. [37] The dissolution rate is about three times lower at pH 7.4 than at pH 5 [37]. However, the EDRs are three times higher at 37 °C than at RT for Hanks' solution at pH 7.4 even though the oxygen solubility is lower at 37 °C, since the dissolution reaction

accelerates as the temperature increases [37]. The evolution of the Mo microstructure during dissolution in DI water, especially the surface passivation oxide layer, leads to changes in the dissolution kinetics [37]. An initial native oxide MoO_3 is present and an oxide mixture of MoO_2 , Mo_2O_5 , and MoO_3 develops on the surface as hydrolysis proceeds. [37] The oxide thickness gradually increases over time, and only Mo_2O_5 oxide ultimately remains. [37] W also has a mixture of W oxides and H_2WO_4 as a dissolution product, but EDRs are four times lower at pH 5 than at pH 7.4 ($7 \times 10^{-4} \mu\text{m/h}$ in DI water at RT) (Fig. 9D) [37,85]. W has a surface morphology similar to that of Mo with an initial native oxide of WO_3 , a mixture of W^{4+} , W^{5+} , W^{6+} oxide as dissolution products, and terminal products of W^{5+} oxide [37]. Both MoO_x and WO_x gradually dissolve in water ($0.2 \sim 0.5 \text{ nm/day}$), which decreases the rate of the thickness change [37].

Fe and Zn undergo non-uniform dissolution by formation of nucleates at random locations [37]. Fig. 9E shows the variation in electrical resistance of Fe during the dissolution process ($<1 \times 10^{-3} \mu\text{m/h}$ in DI water at RT) [37]. Fe forms a thick surface layer of Fe_2O_3 that slows dissolution as a protective layer, such that dissolution gradually ceases (after 120 h in this study) [37]. Fig. 9H shows the microstructural changes in Fe during dissolution in DI water [37]. Fe_3O_4 is the final dissolution product of Fe and is formed after hydroxide formation under excessive oxygen [86]. The passivation by surface oxide decelerates the dissolution, so the pits and plateaus formed by non-uniform dissolution are not eliminated and remain [37]. A surface oxide does not form in an acidic environment (pH 5), so dissolution behavior is uniform and fast [37]. Zn also undergoes non-uniform dissolution similar to that of Fe. Zn has petal- and fiber-like dissolution products, mainly consisting of ZnO and Zn(OH)_2 , and a porous morphology with a non-uniform surface oxide. [37] Fig. 9F shows the change in EDR of Zn during dissolution ($0.07 \mu\text{m/h}$ in DI water at RT). [37] The EDR of Zn is faster than those of Mo, W, and Fe but slower than Mg and the Mg alloy [37]. EDR of Zn is four times lower in DI than in Hanks' solution due to rapid attack by Cl^- . [37] The dependence of EDR on pH and temperature is similar to that in Mg [37]. Dissolution in Hanks' solution leads to formation of a partially protective Zn oxide layer of relatively high solubility [37]. The hydrolysis products of Zn dissolve completely after 5–7 days, whereas Fe oxides do not dissolve completely even after a month [37].

The dimensions and surface morphologies also affect dissolution kinetics of metal features, as in the case of dissolution of thin metal foils that are useful as transient rigid substrates [37,81]. Mo foils (5 μm thick)

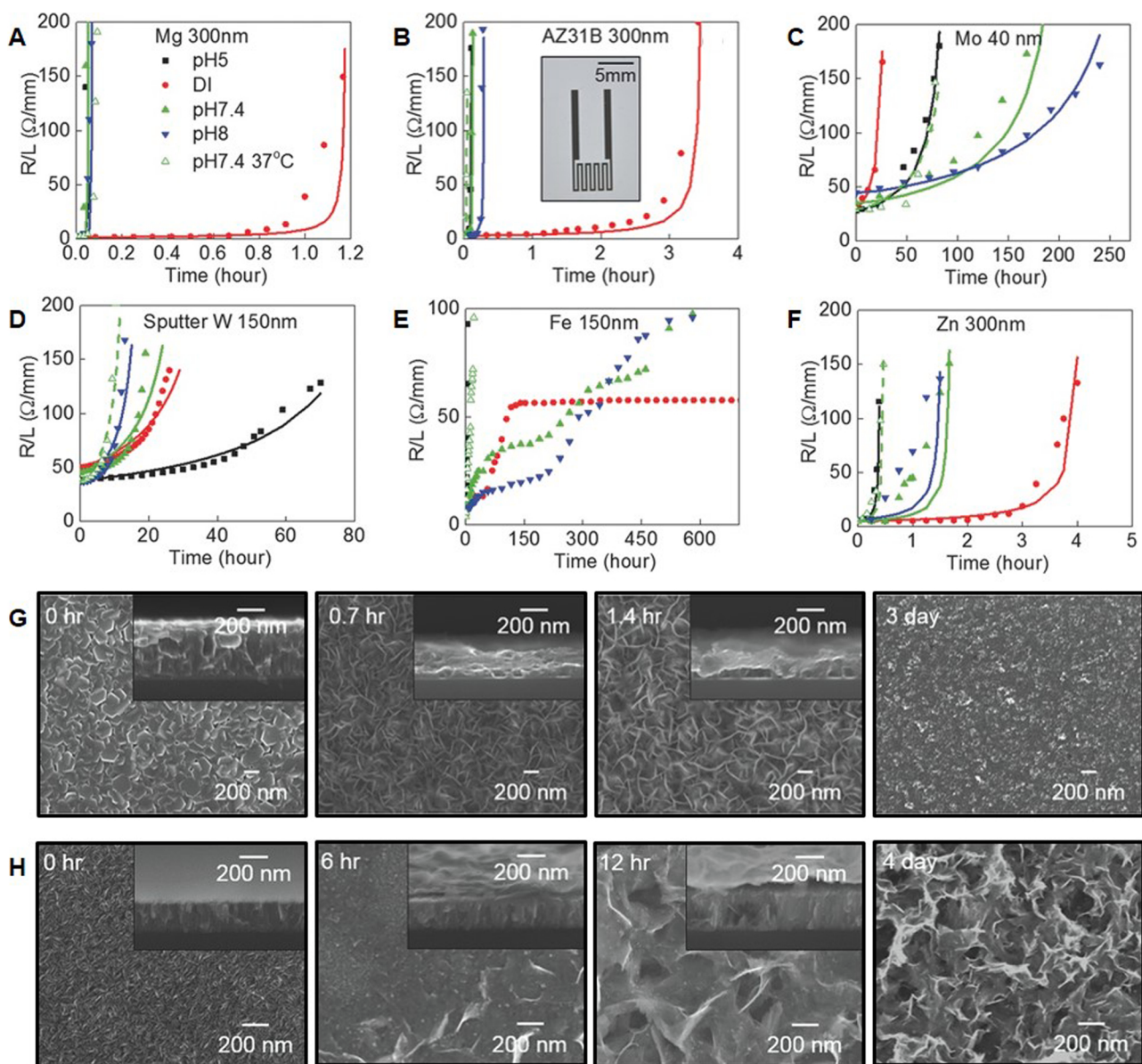


Fig. 9. Dissolution behavior of biodegradable metals in aqueous solution.

Variation in resistance of serpentine traces consisting of Mg (A), AZ31B Mg alloy (B), Mo (C), W (D), Fe (E), Zn (F) during dissolution in Hanks' solution of different pH and DI water (Hanks' solution of pH 5, black; 7.4, green; 8, blue; at RT and pH 7.4 at 37 °C, green outline; DI water, red). Adapted with permission from References [37]. © 2013 WILEY-VCH Verlag GmbH & Co. KGaA, Weinheim (G) SEM images of Mg microstructure during dissolution in DI water. Adapted with permission from References [37]. © 2013 WILEY-VCH Verlag GmbH & Co. KGaA, Weinheim (H) Irregular dissolution behavior of Fe (SEM images in DI water). Adapted with permission from References [37]. © 2013 WILEY-VCH Verlag GmbH & Co. KGaA, Weinheim (For interpretation of the references to colour in this figure legend, the reader is referred to the web version of this article.).

dissolved completely and uniformly after 25 days without significant change in surface morphology when immersed in pH 7.4 PBS (Sigma-Aldrich, USA) at 90 °C [81]. Dissolution tests on Zn, Fe, and W foils were also conducted in PBS and Hanks' solution [81]. The rates of film thickness change are 0.02, 3.5, 0.08, 0.15 µm/day in pH 7.4 PBS at 37 °C and 0.005, 7.2, 0.005, 0.19 µm/day in Hanks' solution for Mo, Zn, Fe, and W, respectively [81]. For Zn and W foils, dissolution was faster in Hanks' solution, while dissolution in PBS was faster for Mo and Fe foils [81]. These different results for the dissolution behavior of metal thin films support the conclusion that a metal's morphology can greatly affect dissolution behavior [81].

Metal elements can form alloys or intermetallic compounds with other metal or non-metal elements, and these materials can be excellent biodegradable conductors by combining the properties of various elements through alloying [82]. Metal components with very fast

dissolution rates such as K, Na, and Ca, or trace elements such as Sn and Mn also can be used in biodegradable alloys, and so much research is underway to utilize new alloys based on Mg, Fe, and Zn, such as a Mg alloy with a Sn-Na master alloy [82]. Biodegradable intermetallic compounds also can be used. Representatively, intermetallic compounds using various elements such as Ca₂Si, CaMgSi, Mg₂Si, and Mg₂Ca have dissolution behavior that depends on the element composition [82]. Metallic alloys and intermetallic compounds have much potential as transient conductors, since they can be tuned in various ways via the alloying elements [82]. In-vivo biocompatibility tests for various intermetallic compounds are likely to identify additional candidate biodegradable conductors [82].

3. Transient organic electronic materials

Organic materials are key components of transient electronics as well as inorganic materials. Organic materials have the advantages being mechanically flexible, stretchable, and soft compared with inorganic materials, and they are compatible with an inexpensive process at low temperatures through a solution process or fiber process [87]. Organic materials also can easily tune various properties such as mechanical properties, electrical properties, and degradation rates by adjusting the amount of monomer or by partly changing the chemical group during the synthesis process [87]. There have been attempts to utilize biodegradable polymers in electronics on the basis of these advantages. Biodegradable polymers were used for structural materials such as substrates or encapsulation layers based on excellent mechanical flexibility in the early days [21], but they started being used as key elements of active devices as polymers with semiconducting properties with long conjugation structure were discovered. Fig. 10 shows the chemical structure of various biodegradable polymers with semiconducting properties. Bettinger et al. demonstrated the first version of transient

electronics by 5,5'-bis-(7-dodecyl-9H-fluoren-2-yl)-2,2'-bithiophene (DDFTTF) with semiconducting properties from long intramolecular conjugation [22,88]. Fig. 11A shows a thin-film organic transistor composed of a p-channel DDFTTF active layer as a semiconductor, Ag electrode, PVA dielectric (non-crosslinked PVA (nPVA) and photo-crosslinked PVA (xPVA)), and PLGA substrate [22]. Fig. 11B shows the electrical performance of organic transistor with nPVA dielectric, which shows $0.153 \text{ cm}^2/\text{V}\cdot\text{s}$ of carrier mobility, 3.49×10^3 of on/off current ratio, and -15.6 V of threshold voltage [22]. A transistor with xPVA dielectric shows the inferior performance with $0.060 \text{ cm}^2/\text{V}\cdot\text{s}$ of carrier mobility, 2.93×10^3 of on/off current ratio, and -13.6 V of threshold voltage [22]. The organic transistor lost its functionality as the DDFTTF layer was delaminated from the dielectric in less than 2 days of immersion in the citrate buffer, and the mass of the device began decreasing significantly owing to the mass degradation of the PLGA substrate after 30 days [22]. Although the biodegradation mechanism of DDFTTF has not been accurately identified, it is predicted to be similar to melanin [22].

Various pigments in nature are also mainly used as natural organic

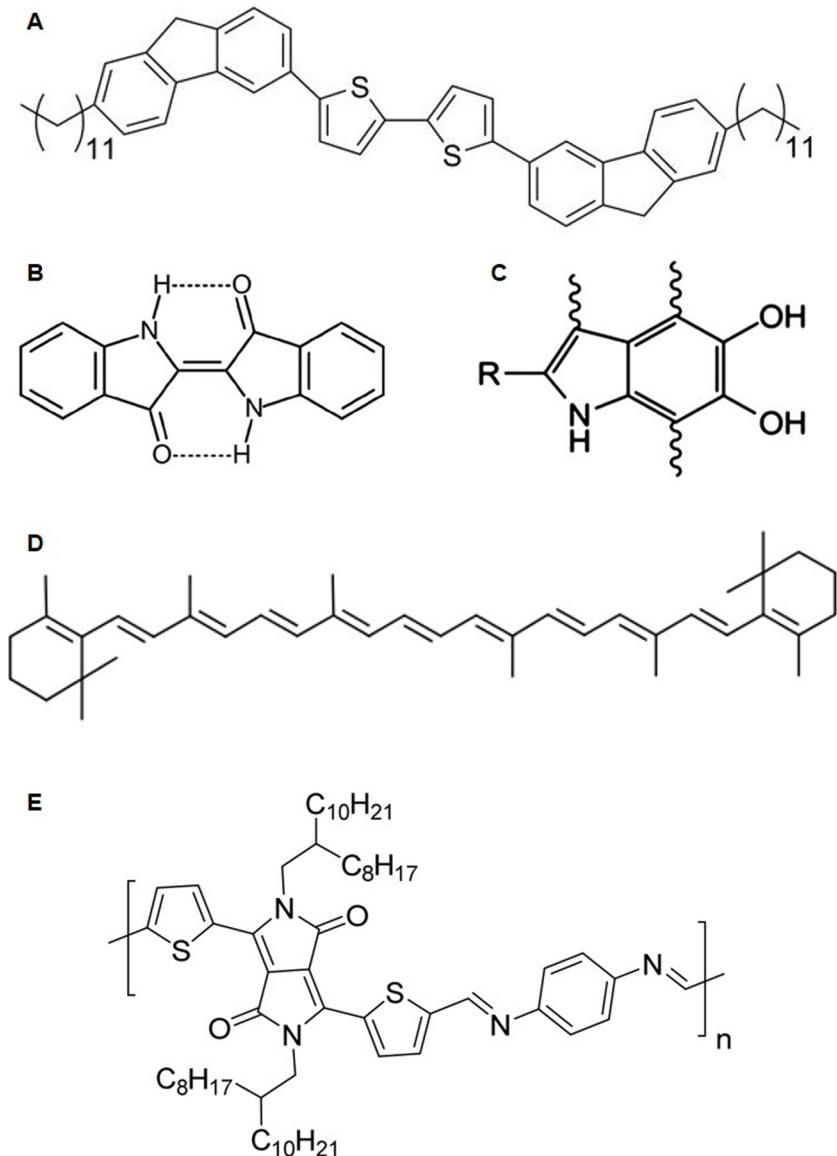
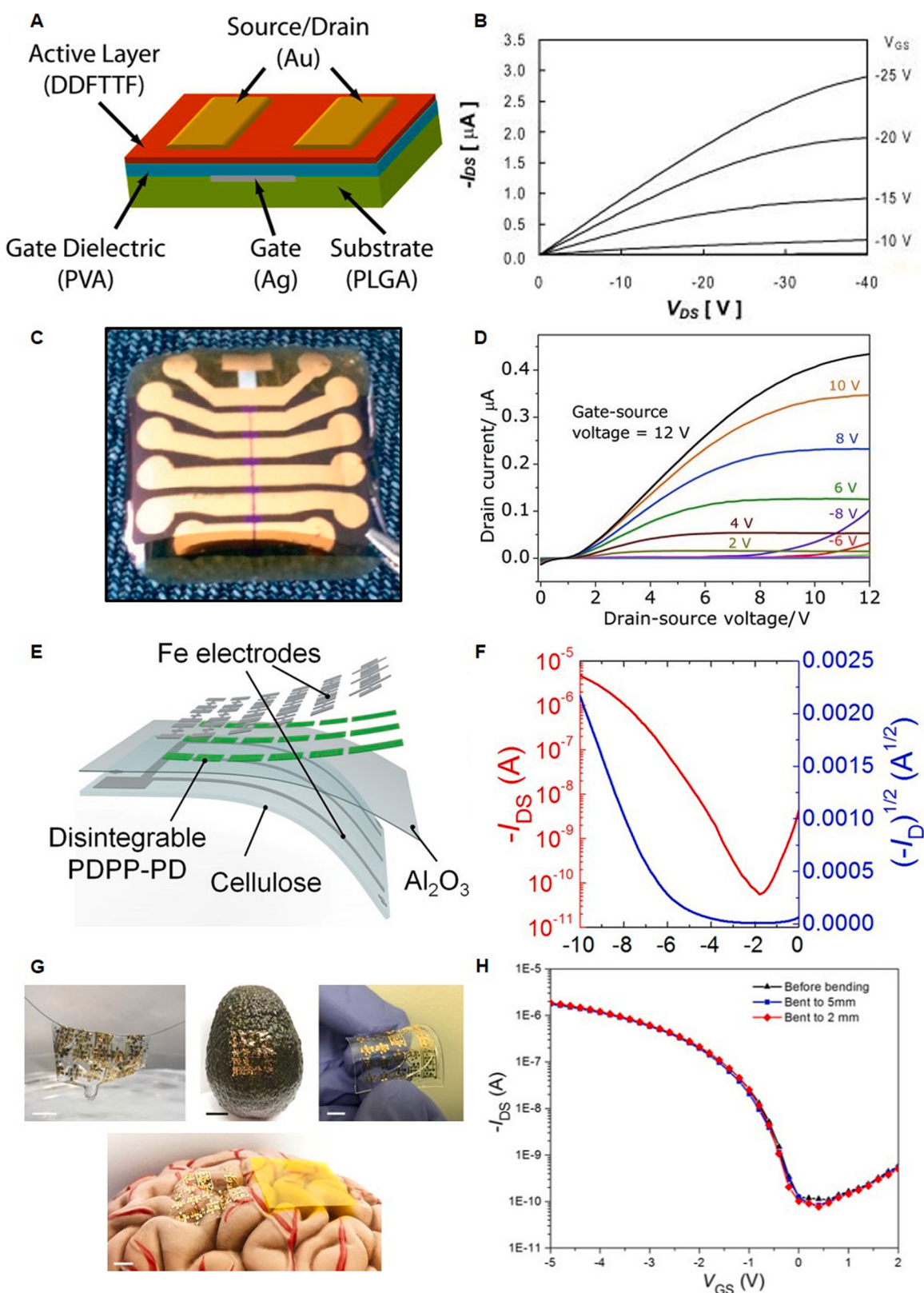


Fig. 10. Chemical structures of biodegradable polymers with semiconducting properties: (A) DDFTTF, (B) indigo, (C) melanin, (D) β-carotene, (E) PDPP-DP. Adapted with permission from References [22–24,90,93]. © 2010 WILEY-VCH Verlag GmbH & Co. KGaA, Weinheim, 2012 WILEY-VCH Verlag GmbH & Co. KGaA, Weinheim, 2012 National Academy of Sciences, 2010 WILEY-VCH Verlag GmbH & Co. KGaA, Weinheim, 2017 National Academy of Sciences.



(caption on next page)

Fig. 11. Electric performance and dissolution chemistry of transient organic electronic materials.

(A) Image of the thin-film organic transistor composed of p-channel DDFTTF semiconductor, Ag electrode, PVA dielectric, and PLGA substrate. Adapted with permission from References [22]. © 2010 WILEY-VCH Verlag GmbH & Co. KGaA, Weinheim (B) Electrical performance of organic transistor composed of DDFTTF semiconductor, Ag electrode, and PLGA substrate with nPVA dielectric. Adapted with permission from References [22]. © 2010 WILEY-VCH Verlag GmbH & Co. KGaA, Weinheim (C) Image of the fully natural OFETs composed of indigo semiconductor, natural resin shellac substrate, AlO_x with TTC passivation layer, and Au electrode. Adapted with permission from References [90]. © 2012 WILEY-VCH Verlag GmbH & Co. KGaA, Weinheim (D) Output characteristics of the n-channel OFETs composed of indigo semiconductor, natural resin shellac substrate, AlO_x with TTC passivation layer, and Au electrode. Adapted with permission from References [90]. © 2012 WILEY-VCH Verlag GmbH & Co. KGaA, Weinheim (E) Image of the CMOS logic circuit composed of PDPP-DP semiconductor, Al_2O_3 dielectric, Au and Fe electrode, and cellulose substrate. Adapted with permission from References [24]. © 2017 National Academy of Sciences (F) Electrical characteristics of fully disintegrable electronics composed of PDPP-DP semiconductor, Al_2O_3 dielectric, and cellulose substrate with Fe electrode. Adapted with permission from References [24]. © 2017 National Academy of Sciences (G) Images of device based on PDPP-PD transferred on human hair, avocado, PDMS, and human brain model. Adapted with permission from References [24]. © 2017 National Academy of Sciences (H) Electrical characteristics of device based on PDPP-PD before and after bending at radii of 5-mm and 2-mm curvatures. Adapted with permission from References [24]. © 2017 National Academy of Sciences.

semiconductors as they have a long conjugation structure [89]. Indigo, one of the most mass-produced pigments, has intra- and intermolecular hydrogen bonding between amine hydrogens and carbonyl groups that forms a tight π -stacking structure with interplanar spacing of $\sim 3.4 \text{ \AA}$ and high planarity of the molecule [87,90]. Indigo has small intramolecular conjugation caused by interference with the conjugation of the carbonyl groups and amine groups in the resonance model, but it shows excellent charge transport properties with a small bandgap of 1.7–1.8 eV as the π -stacking structure enhanced via hydrogen bonding acts as a pathway for charge carrier [87,90]. Fig. 11C shows the fully natural OFETs composed of indigo (thickness: 75 nm) as a semiconducting polymer, natural resin shellac substrates, AlO_x (thickness: 45 nm) gates with a thin passivation layer of tetratetracontane ($\text{C}_{44}\text{H}_{90}$, TTC; thickness: 30 nm) and Au electrode (thickness: 100 nm) [90]. Fig. 11D shows the output characteristics of n-channel indigo-based ambipolar transistor. Indigo-based transistors demonstrate their performance with threshold voltages of -1.5 to -3 V for holes and 4.5 V to 7 V for electrons, and field-effect mobilities of $1 \times 10^{-2} \text{ cm}^2/\text{V}\cdot\text{s}$ for electrons and 5×10^{-3} to $1 \times 10^{-2} \text{ cm}^2/\text{V}\cdot\text{s}$ for holes [90]. Indigo oxidizes to CO_2 , NH_4^+ , NO_3^- , SO_4^{2-} through TiO_2/UV -based photocatalytic degradation with an intermediate product of carboxylic acid. TiO_2 acts as a photocatalyst that oxidizes indigo by forming photoholes and radicals [91]. UV irradiation with a transmittance of $>290 \text{ nm}$ applied to 3- μmol solid-indigo-deposited optical disk degraded the solid indigo mostly within 9 h, and the CO_2 level reached a maximum value of 33 % conversion after 20 h [91].

Melanin, the major component in human skin pigment, also has semiconducting properties [92,93]. Melanin has semiconducting properties based on aromatic system with strong $\pi-\pi$ interaction and has a large range of electrical conductivity dependent on the temperature, physical form, and hydration state [92,93]. Melanin film has a low conductivity of 10^{-8} S/cm in the dried state, but the conductivity increases significantly to 10^{-3} S/cm in the fully hydrated state [92]. The hydration of melanin shifts the comproportionation equilibrium, as the equilibrium concentrations of hydroxyquinone, quinone, and semi-quinone in macromolecules are regulated to form electrons and protons as carriers [93]. Melanin film also has excellent biocompatibility that aids the growth and attachment of Schwann cells (SCs) and PC12 cells for neural tissue engineering [92]. SCs culture was performed on melanin film spin-coated substrate hydrated in 100 % humidity with a conductivity of $7.00 \times 10^{-5} \text{ S/cm}$, collagen-coated glass, and uncoated glass substrates, and the cell density of melanin-coated substrate was 2 times and 4 times higher than that of the collagen-coated glass substrate and the uncoated glass substrate at 5 days, respectively [92]. SCs on melanin film also had more activated phenotypes, enhanced proliferation, and larger distribution of neurite extension [92]. Melanin degrades to naturally occurring molecules, including dopamine, tyrosine, and their derivatives, but the exact mechanism of degradation has not yet been identified [92]. Carotenoids such as β -carotene also have linear π -conjugation that enables its use as hole-transporting semiconductors [23,87]. The natural OFETs on a biodegradable plastic substrate was demonstrated using β -carotene as a semiconductor and glucose as a

natural gate insulator; however, their efficiency was not very high with a low carrier mobility in the range of $1 \times 10^{-4} \text{ cm}^2/\text{V}\cdot\text{s}$ [23,87]. Indanthrene dyes such as indanthrene yellow G and indanthrene brilliant orange RF can also be used as a biodegradable organic semiconductor [23,87]. OFET was fabricated using indanthrene brilliant orange RF as an organic semiconductor and anodized aluminum with guanine and adenine as a gate dielectric, and it demonstrated a field-effect mobility of $\sim 1.75 \times 10^{-3} \text{ cm}^2/\text{V}\cdot\text{s}$ with an operation voltage as low as 7–8 V [23]. Further discussions regarding the detailed biodegradation mechanism of these various organic semiconducting polymers are required.

Synthetic polymers can enhance the semiconducting performance such as carrier mobility compared to natural semiconducting polymers. Recently, poly(diketopyrrolopyrrole-p-phenylenediamine) (PDPP-PD) has been used as a biodegradable semiconducting polymer with enhanced performance [24]. PDPP-PD can be synthesized by condensation reaction between diketopyrrolopyrrole-aldehyde (DPP-CHO) and p-phenylenediamine, which builds intramolecular conjugation and intermolecular π -stacking through imine bond ($=\text{C}=\text{N}-$) [24]. DPP is a dye synthesized from natural resources and has excellent processability through easy chemical functionalization [24]. DPP is synthesized by reacting succinic ester with 2-thiophenecarbonitrile under *tert*-amyl alcohol and then attaching branched alkyl chains from octyldodecanol to increase solubility [24]. DPP-CHO is synthesized by attaching two aldehydes onto DPP, and an imine bond is formed to form PDPP-PD as DPP-CHO is condensed with p-phenylenediamine under p-toluenesulfonic acid used as catalyst [24]. PDPP-PD is degraded through a catalysis reaction in an acidic condition ($\text{pH} = \sim 4.6$) [24]. First, an imine bond is hydrolyzed under acid catalyst resulting in decomposition of PDPP-PD into the DPP-CHO monomer; subsequently, the lactam ring of DPP-CHO is broken by hydrolysis and completely decomposed into colorless products [24]. The change in absorption spectrum of PDPP-PD during immersion in 1% (vol/vol) acetic acid shows excellent biodegradability of PDPP-PD [24]. The main absorption peak of 680 nm decreased significantly after 3 h due to the degradation of PDPP-PD under an acidic solution and disappeared completely after 10 days; thus, PDPP-PD had a spectrum similar to that of the pure monomer of DPP-CHO [24]. PDPP-PD also shows outstanding biocompatibility, as it had a negligible effect on the viability of HL-1 from 2 to 6 days at pH 7.4 during *in vitro* cell culture of HL-1 cardiomyocytes with PDPP-PD-coated glass substrate [24]. Fig. 11E shows the CMOS logic circuit composed of PDPP-PD as a semiconductor, Al_2O_3 as a dielectric, Au and Fe as electrodes, and a cellulose substrate. Fig. 11F shows the electronic characteristics of fully disintegrable electronics. The hole mobility is much higher when Au is the electrode ($\sim 0.21 \text{ cm}^2/\text{V}\cdot\text{s}$ and $\sim 0.12 \text{ cm}^2/\text{V}\cdot\text{s}$ for Au electrode and Fe electrode, respectively) as the Au work function (work function: 5.1 eV) is closer to HOMO of PDPP-PD (5.11 eV) than Fe (work function: 4.8 eV) [24]. However, fully disintegrable electronics were demonstrated with the Fe electrode as Au is not biodegradable [24]. The device demonstrated stable performance with on/off ratios $> 10^4$ for several days in DI, but its performance was lost within 1 h in pH 4.6 buffer solution, and all components completely disappeared after 30 days [24]. Devices based on organic materials have the advantage of

conformal contact and excellent flexibility compared with devices made of inorganic materials, although their electric performance is relatively low [24]. Fig. 11G shows the organic transistors based on PDPP-PD transferred onto human hair, avocado, PDMS, and the human brain model. The transistor with PDPP-PD has a soft contact to be used on various substrates that can even be transferred to rough surface like avocado or brain model [24]. Organic transistors based on PDPP-PD also shows high flexibility, exhibiting less than a 5% change in the transfer characteristics during bending deformation, with a 2 mm radius (Fig. 11H) [24].

4. Materials strategy for control of transiency

4.1. Encapsulation materials

One of the important factors in transient electronics is controlling the functional lifetime. The dissolution of the electronic circuit (usually by water diffusion) causes a loss of function before all of the material of the device dissolves. Thus, the functional lifetime of a transient device is usually much shorter than the full transient time. Fig. 12A shows the results of immersion tests of arrays of n-channel transistors using Si NM channel, SiO₂ gate dielectric and Mg electrode with MgO encapsulation by in-situ recording of transfer performance [15]. Two-stage transition of the encapsulated device explains the concept and controllability of the functional lifetime. First, the immersed device operates stably by blocking water permeation through the encapsulation layer, and the electrical performance drops sharply as the encapsulation layer slowly degrades and water diffuses to the crucial elements (Fig. 12B) [15]. The encapsulation layer delays the diffusion time of water vapor to the electronic circuit, which extends the stable operating time of the device [15]. The water permeation characteristics of encapsulation layers, which are usually related to their surface chemistry, crystallinity, and thickness, are key in controlling the operational lifetime [15,36,42,56, 94–97].

Inorganic materials with dense atomic arrangements are generally regarded as excellent encapsulants, while organic materials have relatively porous micromolecular structures of long and entangled chains and poor water barrier properties [15,36,42]. MgO is a good candidate for a biodegradable inorganic encapsulant. Fig. 12C shows that an encapsulation layer of 400 nm of MgO increases the stable period of resistance of a 300-nm-thick Mg resistor during immersion in DI water at RT from ~1 h to ~3 h [15]. The water diffusion time can be controlled by adjusting the thickness of the encapsulation layer [15]. For example, an encapsulation layer of 800 nm of MgO greatly increases the stable period of resistance up to ~13 h [15]. MgO is not suitable for long-term use because its own dissolution rate is relatively high [15]. Materials with moderate dissolution rates, such as SiO₂ and Si₃N_x, widely used in encapsulation in organic light-emitting diodes, have been highlighted for use for long-term encapsulation [36,42].

SiO₂ and Si₃N_x are dissolved in a uniform fashion, and the dissolution rate can be controlled through the method and conditions of deposition. [36]. PECVD is widely used for the encapsulation process because of its rapid deposition rate and low-temperature process conditions. However, it usually possesses a pinhole defect, which is a short path of water leakage [36,42]. Fig. 12D shows the localized dissolution of an Mg pattern by leakage through a pinhole in the SiO₂/SiN encapsulation layers [36]. Multilayer structures of silicon oxide and nitride or atomic layer deposition (ALD) have been introduced to minimize process defects and enhance water-barrier properties [36]. An Mg conductor (300 nm thick) encapsulated by a single layer of PECVD SiO₂ or Si₃N_x (~1 μm thick) showed a significant increase in resistance after a few hours of immersion in pH 7.4 PBS at 37 °C, whereas triple layers of PECVD SiO₂ and Si₃N_x (~200 nm/200 nm/200 nm/200 nm/100 nm/100 nm thick) extended the functional lifetime to ~10 days [36]. Atomic layer deposition (ALD) provides a defect-free SiO₂ layer [36]. A single layer of ALD SiO₂ (~20 nm thick) cannot significantly increase functional

lifetime because it is too thin to cover a structure uniformly; however, combinations of PECVD SiO₂/ALD SiO₂ (~500/20 nm thick) and PECVD Si₃N_x/ALD SiO₂ (~500/20 nm thick) increase the functional lifetime to ~5 days and ~7 days, respectively [36].

Thermal SiO₂ grown from single-crystal Si has a defect-free nature, so it is regarded as an excellent encapsulant, without crystalline defects and free volume [42,57,94]. An Mg conductor (200 nm thick) encapsulated with thermally grown SiO₂ (100 nm thick) dissolves completely at once and for up to 22 days during immersion in pH 7.4 PBS at 70 °C [42]. Depositing and patterning Mg conductors on thermally grown SiO₂ at ~1100 °C on a Si wafer, bonding the top side of Si to a glass temporary substrate coated with thin PI, removing the back side of the handle silicon wafer through dry etching, and peeling the wafer from a temporary substrate forms a thin Mg conductor entirely encapsulated with a thermal SiO₂ layer [42]. Electrical current leakage via permeation of PBS through thermal SiO₂ on n-type Si wafer was measured [42]. The time to reach the high leakage current due to permeation was linearly proportional to the thickness of the encapsulation layer [42]. This suggests hydrolysis of thermal SiO₂ mainly proceeds by surface reactions rather than reactive diffusion into bulk SiO₂ or permeation through defect sites [42]. Water penetration from the back side can also be prevented by transfer of the thermal SiO₂ layer on the back side of the polymer (PI) surface with a patterned layer of Mg [42]. Back-side SiO₂ encapsulation was found to expand the functional lifetime of Mg conductors up to 15 days in 70 °C PBS, whereas dissolution occurred in a few hours without encapsulation by direct water permeation through the PI [42].

Monocrystalline Si NM is also a good candidate for a defect-free encapsulation layer. Monocrystalline Si NM has excellent crystallinity, so hydrolysis occurs only through surface reactions, without diffusion through defects or pinholes [56]. An encapsulation layer of 1.5-μm Si NM was found to expand the functional lifetime of a thin Mg film (200 nm thick) up to ~10 months in pH 7.4 PBS at 37 °C and to ~23 days at 70 °C [56]. The dissolution rate of Si NM varies depending on intrinsic factors, so the lifetime of encapsulation is controllable [56]. The lifetime is significantly extended by increasing the doping concentration, owing to the lower dissolution rate of highly doped Si as described previously [39,56]. In addition, the initiation of Si dissolution can be delayed by reducing the reactivity through chemical functionalization of Si surfaces, such as Si-C and Si-O [56]. Furthermore, ~3- and ~20-nm-thick surface oxides are formed through exposure to UV ozone and O₂ plasma, which can delay Si dissolution by ~10 and ~30 days, respectively [56]. Si NMs can be used as an encapsulation layer in various applications because the encapsulation lifetime is easily adjusted by varying intrinsic factors [39,56].

Transient organic encapsulants offer a wide range of surface chemistries and mechanically soft and flexible forms of passivation with a low-temperature solution process, although their porous microstructures result in relatively poor water barrier properties [95–97]. Biodegradable polymers, which are easily formed by spin-coating or molding, such as silk fibroin, have been used in the past; however, these materials are prone to swelling and water permeation because of hydrophilic bonds, such as hydroxyl and carboxylic groups [15]. Natural wax, a representative hydrophobic and biodegradable polymer, is an excellent candidate for organic encapsulation [95]. Candelilla wax has the highest hydrocarbon content of the various natural waxes available and the most hydrophobic character [95]. The water permeability of candelilla wax is also the lowest, with negligible water uptake for more than 15 days at 37 °C [95]. The resistance of Mg traces (200 nm thick) with Candelilla wax encapsulation (300 μm thick) was found to remain unchanged for more than 7 days in pH 7.4 PBS at 37 °C, and a rapid increase in resistance was found to occur by 10 days, until complete disconnection after 15 days [95]. Candelilla wax also showed a continuous weight decrease, which means that dissolution is caused by surface reaction rather than by water absorption or swelling [95,96]. Fig. 12E shows the change in resistance of 300-nm-thick Mg traces encapsulated by various waxes containing hydrophobic candelilla wax

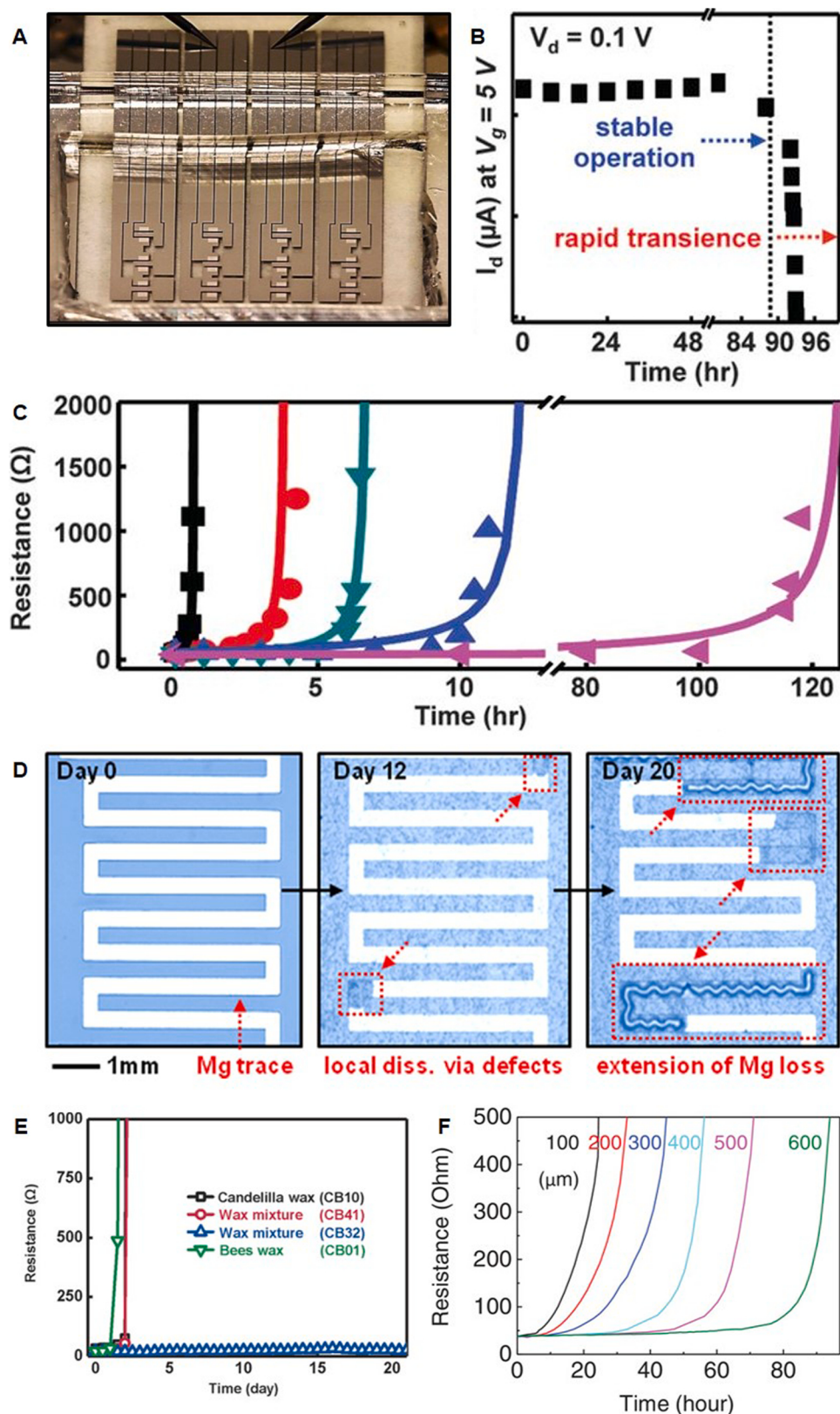


Fig. 12. Encapsulation materials and strategies for functional lifetime control of transient devices.

(A) Array of n-channel transistors with MgO encapsulation layer in an immersion test in a PDMS well filled with DI water for real-time monitoring Adapted with permission from References [15]. © 2012, American Association for the Advancement of Science (B) Two-stage dissolution behavior in n-channel transistors encapsulated by MgO and silk at $V_d = 0.1 \text{ V}$ and $V_g = 5 \text{ V}$ during immersion in Di water: stable operation during protection, fast drop in function by water molecule penetration. Adapted with permission from References [15]. © 2012, American Association for the Advancement of Science (C) Resistance variation in Mg traces encapsulated by various encapsulant layers. (without encapsulation, black; with MgO 400 nm, red; 800 nm, blue; with silk I, cyan; silk II, purple. Silk I and silk II have different crosslinking density). Adapted with permission from References [15]. © 2012, American Association for the Advancement of Science (D) Images of Mg trace (300 nm thick) encapsulated with triple layers of PECVD SiO_2 and Si_3N_4

(~200 nm/200 nm/200 nm/100 nm/100 nm thick, total thickness ~1 μm) illustrating localized dissolution via leakage through defects during immersion in DI water. Adapted with permission from References [36]. © 2014 WILEY-VCH Verlag GmbH & Co. KGaA, Weinheim (E) Encapsulation behavior of hydrophobic natural wax and its mixture illustrated by variation in resistance of encapsulated Mg trace during dissolution in PBS at 37 °C (candelilla wax (CB10), black; wax mixture of candelilla wax and beeswax at ratio of 4:1 (CB41), red; with ratio of 3:2 (CB32), blue; beeswax (CB01), green). Adapted with permission from References [96]. © 2020 WILEY-VCH Verlag GmbH & Co. KGaA, Weinheim (F) Encapsulation performance of PBTPA with ratio of 4PA, TTT, BDT is 1:4:7 at different thicknesses measured by variation of resistance in encapsulated Mg trace while immersed in pH 7.4 PBS at 37 °C (100 μm , black; 200 μm , red; 300 μm , blue; 400 μm , cyan; 500 μm , magenta; 600 μm , olive). Adapted with permission from References [97]. © 2020 WILEY-VCH Verlag GmbH & Co. KGaA, Weinheim (For interpretation of the references to colour in this figure legend, the reader is referred to the web version of this article.).

and hydrophilic beeswax [96]. Hydrophobic candelilla wax showed better encapsulation performance owing to its lower water permeation [96]. In addition, the encapsulation layer of hydrophilic beeswax wax with candelilla wax at a ratio of 3: 2 showed the best encapsulation performance, with the resistance unchanged for 22 days in pH 7.4 PBS at 37 °C [96]. Candelilla wax is strongly bonded with beeswax through hydrogen bonding, owing to the increased contents of ester and anhydride derivatives, resulting in excellent water barrier performance [96]. Candelilla wax can also be mixed with poly butanedithiol 1,3,5-triallyl-1,3,5-triazine-2,4,6(1H,3H,5 H)-trione pentenoic anhydride (PBTPA) to further enhance its mechanical properties [96]. The time to double the resistance of the Mg trace was found to increase from 2 days to 7 days as the concentration of candelilla wax in PBTPA increased from 0 to 20 wt% [96]. This could be increased up to 10 days with a bilayer of candelilla wax/PBTPA with 20 wt% candelilla wax [96]. PBTPA itself can also be used as an encapsulation layer [97]. Crosslinking of multi-armed divinyl linkers of 1,3,5-triallyl-1,3,5-triazine-2,4,6(1H,3H, 5 H)-trione (TTT) and allyl-containing monomers of 4-pentenoic anhydride (4PA) with 1,4-butanedithiol (BDT) through thiolene reactions initiated by UV light synthesizes well-controlled PBTPA films [97]. BDT contains a hydrophobic chain, so control of the hydrophobicity of PBTPA is possible by adjusting the ratio of BDT [97]. PBTPA 1:4:7 (4PA: TTT:BDT), which has the highest hydrophobicity, shows low water permeability and a low dissolution rate, allowing acceptable encapsulation performance [97]. The PBTPA film shows excellent mechanical stability under various deformations, which provides a robust water barrier to diverse transient and flexible electronics [97]. Fig. 12F shows the change in resistance of 300-nm-thick Mg traces encapsulated with different thickness of PBTPA 1:4:7 [97]. The electrical properties of a 300-nm-Mg trace encapsulated with 600- μm -thick PBTPA 1:4:7 did not change even after 80 h but were diminished after 95 h in pH 7.4 PBS at 37 °C [97]. There was no leakage through defects, as dissolution of the Mg trace occurred uniformly [97].

4.2. Triggered transient electronics for on-demand transience

On-demand control of degradation, referred to as triggered transient electronics, is another important mode in transient electronics. Most transient electronics are degraded by hydrolysis reactions in aqueous environments, so the dissolution time is passively determined by encapsulation materials and thickness [15,36,42,56,94–97]. Triggered transient electronics is a technology that controls the initiation of decomposition by specific types of stimulation, such as heat, light, moisture, and other types, at an on-demand time point. A given external stimulus can directly decompose electronic materials or induce other physical, mechanical, or chemical reactions in series to destroy the constituent materials [16–18]. Table 4 summarizes the representative stimulus strategies and degradation mechanisms of triggerable transient electronics. Stimulus-responsive materials are essential to control the initiation of overall degradation. Embedded systems for delivering the stimulus to a device on-demand (usually wirelessly) are also important in triggering transient electronics [16–18,98–112]. You et al.'s article offers comprehensive information regarding on-demand trigger transient electronics, including various material strategies, trigger mechanisms, and future directions [113].

Metastable polymers with low ceiling temperatures (T_c) and self-

immolative polymers are good candidate materials for stimulus-responsive degradation [16,114]. Cyclic poly(phthalaldehyde) (cPPA) synthesized through cationic polymerization of o-phthalaldehyde (oPA) is a representative acid-sensitive metastable material with a low T_c , as it undergoes immediate depolymerization to the oPA monomer through cleavage of the acetal backbone by acid- or mechanical force-induced unzipping above T_c [16,114,115]. The oPA monomer evaporates at sufficiently high temperatures (> 85 °C) with negligible residues (< 2 %). [115]. The main challenge of triggerable electronics with cPPA is how to deliver acids to cPPA [16]. Fig. 13A shows the overall strategy of acidic depolymerization of cPPA using light triggering by mixing 2-(4-methoxystyryl)-4,6-bis(trichloromethyl)-1,3,5-triazine (MBTT), a photoacid generator (PAG) [16]. MBTT generates a highly reactive Cl-radical that forms HCl with hydrogen from the environment when exposed to UV light, and HCl depolymerizes cPPA to oPA [16]. Acidic depolymerization of the cPPA substrate causes the mechanical destruction of the substrate and acid degradation of the electronic device [16]. Providing UV light (1.7 mW cm⁻²) to an Mg resistor (300 nm thick) on MBTT/cPPA substrate (40 μm thick) causes the resistor to disintegrate mechanically as the substrate collapses within several minutes and continues to be degraded by HCl, almost entirely disintegrating after 72 h [16]. The function of the electronic device is also stopped instantly as the resistance of the Mg resistor doubles within 20 min (here resistance increase consistently thereafter) [16].

Fig. 13B shows the acidic degradation of cPPA by the thermal triggering method [17]. Thermal triggering is achieved by pure silicon wax with a low melting temperature (T_m = 43 °C) embedded with micro-droplets of methanesulfonic acid (MSA) [17]. The coated wax with MSA melts and releases MSA to etch the electronic circuit and cPPA substrate by applying thermal power to reach a temperature exceeding the melting temperature [17]. An Mg resistor (300 nm thick) on a cPPA substrate with a 40 wt% MSA-in-silicone wax coating (45 μm thick) was found to be stable for more than a month at RT but decomposed and increased resistance by a factor of ~ 500 % within 30 s when heated to 55 °C by the release of acid from the coating and depolymerization of the cPPA substrate [17]. Selective coating with waxes with different melting points allows for selective destruction according to temperature [17].

Direct heating is also used as a triggering stimulus for depolymerizable polymers with a low T_c . Polyoxymethylene (POM) with a low T_c of 119 °C is one of the available depolymerizable polymers [98]. Fig. 13C shows the depolymerization mechanism of a POM substrate with terminal hydroxyl groups obtained by chemical vapor deposition (CVD) [98]. The active hydrogen of the terminal hydroxyl group undergoes thermal oxidative random scission followed by depolymerization at temperatures above T_c [98]. A new hydroxyl-containing POM with a short chain length is formed as the volatile oxymethylene gas is released, and complete unzipping of the macromolecular chain without any residues occurs as this process repeats [98]. A Cr (20 nm)/Au (100 nm)/SiO₂ (20 nm)/Cu (50 nm) memristor formed on a POM substrate (1 mm thick) shows a typical and stable I–V characteristic with bipolar resistive switching by imposing bias before triggering [98]. The POM substrate vanished after thermal triggering at 180 °C, resulting in structural collapse and disintegration into small debris as the POM substrate depolymerized [98]. The memristor lost its electrical properties within 8 min after depolymerization, and was completely destroyed after 42 min [98]. Similarly, a poly- α -methylstyrene (PAMS) substrate

Table 4

Trigger-transient electronics classified by triggering stimulus and decomposition sources.

Initiation stimulus	Decomposition stimulus	Decomposition element	Refs.
Heat	Heat	cPPA + H ⁺ → oPA monomer Mg + 2SO ₃ H → Mg ²⁺ 2SO ₃ ⁻ + H ₂ Polyoxymethylene (with heat) → Formaldehyde Nanocellulose is burned by Ag heater poly- α -methylstyrene (with heat) → methylstyrene monomer Si nanomembrane, SiO ₂ , Mg are mechanically destructed	[17]
		Mg + 2OH → Mg ²⁺ 2(OH) ⁻ Al + 3OH → Al ³⁺ 3(OH) ⁻	[18]
		Mechanically destruction Methyl cellulose (MC) is dissolved in water Poly(<i>N</i> -isopropylacrylamide) (PNIPAm) is dissolved in cold water (under LCST)	[100]
	Cooling	Ag nanowire is mechanically destructed PVP, Alginate film are dissolved in water Li + 2H ₂ O → 2LiOH + H ₂ 2LiOH + V ₂ O ₅ → 2LiVO ₃ + H ₂ O, LiVO ₃ + 2LiOH → LiVO ₄ + H ₂ O 2Al + 6H ₂ O → 2Al(OH) ₃ + 3H ₂ , Al(OH) ₃ + LiOH → LiAl(OH) ₄ Polyanhydride (hydrolysis in water) → Carboxyl acid	[102]
		Mg + 2H ₂ O → Mg(OH) ₂ + H ₂ H ₂ O + 2e ⁻ → H ₂ + 2OH ⁻ Polyanhydride (hydrolysis in water) → Carboxyl acid	[103]
		Metal + Carboxyl acid → RCOO ⁻ + Metal ion + H ₂ Metal oxide + Carboxyl acid → RCOO ⁻ + Metal ion + H ₂ O Metal + acid → Metal ion + H ₂ Metal oxide + acid → Metal ion + H ₂ O	[104]
Water/ Solvent	Water + Base	SI NM + H ₂ O → Si(OH) ₄ MBTT (with UV) → HCl cPPA + HCl → oPA monomer Mg + 2HCl → Mg ²⁺ Cl ²⁻ + H ₂ 4-arms-PEG-NH ₂ , UV sensitive crosslinker (with UV) → Monomer	[105]
		Water	[41]
		Mg + 2H ₂ O → Mg(OH) ₂ + H ₂ MgO + 2H ₂ O → Mg(OH) ₂ W + 6H ₂ O → W(OH) ₆ + 3H ₂ 4Au + 8CN ⁻ + O ₂ + H ₂ O → 4[AuCN] ₂ ⁻ + 4OH ⁻	[106]
	Chemical	[Fe(CN) ₆] ⁴⁻ + 2H ₂ O → [Fe(CN) ₅ H ₂ O] ³⁻ + OH ⁻ + HCN PVP is dissolved in water Li _x Al alloy is dissolved in base solution	[107]
		2NaOH + V ₂ O ₅ → 2NaVO ₃ + H ₂ O, NaVO ₃ + 2NaOH → NaVO ₄ + H ₂ O Porous SI + H ₂ O → Si(OH) ₄ PEO/LiClO ₄ separator are dissolved in water	[108]
		Metal + acid → Metal ion + H ₂ Metal oxide + acid → Metal ion + H ₂ O	[109]
Chemical	Base (NaOH)	CuO/Al nanothermite makes heat (ignition) 3CuO + 2Al → Al ₂ O ₃ + Cu + Heat	[110]
		Metal + acid → Metal ion + H ₂	[111]
	Acid	Si + xLi ⁺ → Li _x Si	[112]
Electric	Heat and Acid		
	Chemical		

with a low decomposition temperature of ~300 °C is also used for the triggerable circuit by integrating Si NM electronics [100].

Various triggering stimuli are also used. Acidic degradation by the electrical field as a triggering stimulus is possible [110]. In one study, an Si₃N₄ reservoir (400 nm thick) was filled with a corrosive mixture of copper etchant (CE-100) and a 10 % NaCl solution containing gold electrolysis electrodes, and the corrosive solution was electrolyzed to generate H₂ and Cl₂ gas with an applied DC voltage, which increased the inner gas pressure [110]. The Si₃N₄ membrane fractured, and the corrosive solution was released as the gas pressure increased above the critical level, resulting in rapid transience after ~50 s [110]. A 50-nm-thick Cu resistor with a resistance of 55 Ω was fabricated through e-beam evaporation on a glass substrate [110]. The resistance increased very quickly to several GΩ in 2 s as the corrosive solution was released to the Cu resistor, resulting in degradation after the voltage trigger [110]. Disintegration of the electronic circuits via electrochemical lithiation of the Si layer is also possible [112]. Li_xSi alloy is formed when Li ions are electrochemically inserted into Si, leading to a dramatic volume change of ~280 % [112]. An accelerated collapse of the circuit occurs due to the volume change, and the entire circuit components easily disappear in a normal environment after the collapse as the Li_xSi alloy is extremely reactive [112]. The degradation of a thin-film Si integrated circuit (IC) chip with metal-oxide-semiconductor field-effect transistors (MOSFETs) with a total thickness of 5 μm via lithiation was conducted. The circuit lost its function after lithiation initiation, and deformation and buckling due to lithiation were observed after 9 h, resulting in complete degradation to the Li_xSi alloy [112]. Lithiation-induced triggering has a high level of stability and controllability because the adjustability of the lithiation device (e.g., lithium ion battery) is excellent [112].

Direct mechanical collapse of a device using pressure from a thermally expandable polymer is also possible [101]. A thermally triggerable system was created by combining a flexible PI substrate (125 μm thick), a Joule heater, an expandable polymer layer (~275 μm thick), and an Si chip (25 μm thick) [101]. The expandable polymer included polymeric microspheres with a small amount of liquid hydrocarbon encapsulated by a gas-tight thermoplastic shell [101]. The shell was softened, and the liquid hydrocarbon changed to the gas phase as the temperature increased up to the critical temperature (80 °C) with a sufficient DC power supply (500–600 mW), followed by volumetric expansion to almost seven times the original volume [101]. Mechanical destruction of a thin Si electronic chip occurs within 10 s when the stress produced by volumetric expansion is greater than the ultimate tensile strength of Si (6.89 GPa) [101]. Localized protective destruction is possible through a suitable combination of the geometric positioning of devices, thicknesses of the polymers and silicon structures, heater location, and thermal characteristics [101]. Fig. 13D shows a system with several resistors connected in parallel that can be destroyed individually [101]. The total resistance of this system changed from 75 to 105 and 180 Ω, and the open circuit proceeded as a sequential fracture [101].

Materials that generate a base or an acid by hydrolysis provide a water-activated triggering strategy by forming an etchant to decompose other acid - or base-sensitive materials in series. Li is a representative example in which hydrolysis proceeds by



and forms a basic solution [103]. Fig. 13E shows the dissolution of lithium ion batteries triggered by cascade reactions of hydrolysis and degradation through byproducts that utilize Li metal as the anode, V₂O₅ as the cathode, polyvinylpyrrolidone (PVP) membrane as the separator, Al/Cu as the current collector, sodium alginate (Na-AG) as the battery encasement, and LiPF₆ as the organic electrolyte [103]. V₂O₅ has a high theoretical capacity of 294 mA h/g as a cathode when a voltage of 2 V is applied to Li/Li⁺ [103]. V₂O₅ has a low dissolution rate in pure water but dissolves very quickly in an alkaline solution with LiOH by [103]

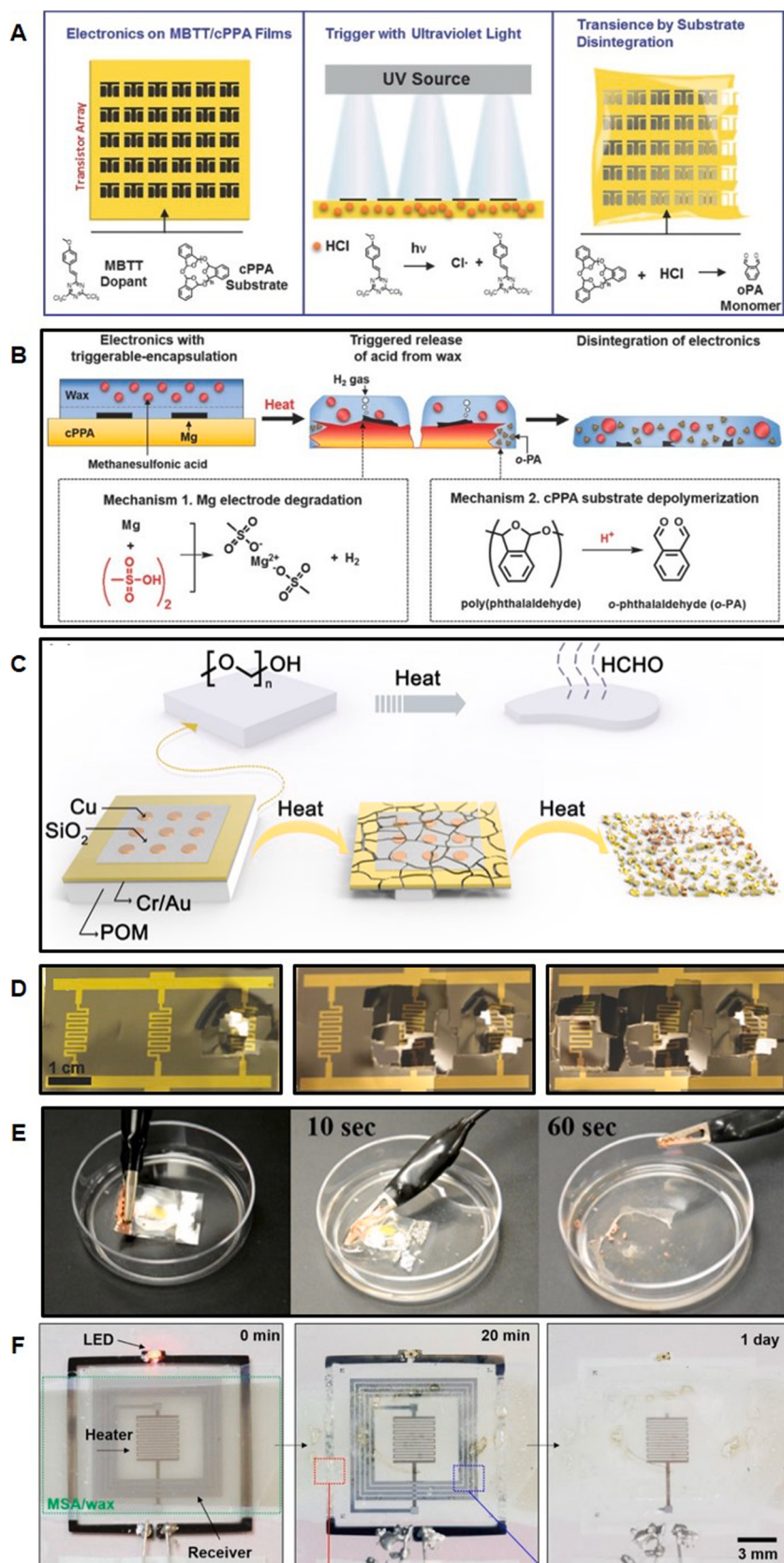


Fig. 13. Triggered transient electronics for on-demand transience control.

(A) Light-triggerable electronics using acid-sensitive cPPA substrates containing photo acid-generating MBTT. Depolymerization of substrate disintegrates the electronic circuit on it. Adapted with permission from References [16]. © 2014 WILEY-VCH Verlag GmbH & Co. KGaA, Weinheim (B) Transient behavior of a cPPA substrate and electronics by melting of MSA encapsulating wax. Adapted with permission from References [17]. © 2015 WILEY-VCH Verlag GmbH & Co. KGaA, Weinheim (C) Heat-triggered degradation of low-temperature-decomposable POM substrate. Adapted with permission from References [98]. © 2019, The Author(s) (D) Mechanically triggered transience using thermally expandable polymer. Adapted with permission from References [101]. © 2017 WILEY-VCH Verlag GmbH & Co. KGaA, Weinheim (E) Dissolution of transient battery triggered by cascade reaction including initial hydrolysis with H₂O of Li anode and following degradation of V₂O₅ cathode, PVP, and Na-AG by alkaline hydrolysis product of Li. Adapted with permission from References [103]. © 2015, American Chemical Society (F) On-demand self-destructing electronics using wireless inductive heating by melting MSA-containing wax. Adapted with permission from References [17]. © 2015 WILEY-VCH Verlag GmbH & Co. KGaA, Weinheim.



Other substances, such as PVP and Na-AG, also degrade rapidly in an alkaline solution [103]. When water droplets are dropped onto a cell, the Na-AG encapsulation and substrate are first dissolved, and then H₂ gas is generated as water reacts with the Li metal, resulting in diffusion of water with LiOH to the V₂O₅ cathode and final collapse [103]. A transient microbattery (with a total mass of 0.1 g) showed stable performance with a working voltage of ~2.8 V, an energy density of ~480 Wh/kg, and a discharge capacity of 131.3 mA h/g, until it was triggered by water, and all components were fully degraded within 60 s through cascade reactions after water triggering [103]. Polyanhydride (PA) is another material that generates an acid by hydrolysis [105]. PA undergoes hydrolysis by absorbing moisture in the air to form corrosive carboxylic acids that decompose a wide range of metal electrodes, metal oxide dielectrics, and semiconductors [105]. A Cu resistor (50 nm thick) was fabricated on a ~124-μm-thick PA substrate with 10 % poly(ethylene glycol) (PEG) at 75 % humidity, and the resistance increased from 600 Ω to 1000 Ω in 20 h as a result of carboxylic acid generated by PA hydrolysis [105]. The resistance increased to 10 MΩ after 25 h because the electrical current path was disrupted by numerous cracks [105].

Methods for applying the stimulus are also important in triggering transient electronics. The ability to embed a device system that can generate a stimulus and control it remotely is a key issue. Fig. 13F shows a self-destructive device that uses wireless thermal triggering with inductive coupling [17]. A resistive heater (Mg/SiO₂/Mg) connected to an Mg receiver coil generates thermal power to dissolve the wax coating, resulting in degradation of the cPPA substrate, Mg coil, and heater by MSA release [17]. The heat itself is also used as trigger stimulus, as mentioned above [18]. Fig. 14A shows similar approaches using a wireless heater but different triggering approaches using thermally expandable polymers [18]. The structure consists of a heating element, thermally expandable polymer, fluid reservoirs, and microfluidic channels [18]. A thermally expandable polymer (300 μm, Expance 031 Du 40) undergoes an irreversible volume increase of ~5 times as it is heated to 80°C and presses the water reservoir region [18]. The water ejects from the reservoir region due to high pressure and passes through a serpentine microfluidic channel containing NaOH powder, with which it mixes to form a highly corrosive etchant [18]. The resulting etchant spreads to the targeted locations of transient electronics, causing degradation of the device [18]. A radio-powered thermal actuator of resistive heating elements wirelessly generates heat up to approximately 80 °C and triggers this process [18]. These systems not only operate directly through the power supply but also achieve remote programmed heating through external stimuli such as time signaling, positioning, light, and pressure, using various sensors [18].

Triggered transient electronics are particularly interesting when combined with transformation. Selective degradation of a device or circuit can change the original functionality [18,41]. Fig. 14B shows the combination of transformation through selective degradation by water triggering [41]. As a specific interconnect with an Mg alloy is disconnected from a CMOS NAND or NOR gate using Si NM with Fe for source, drain, gate electrodes, and interconnects, it is transformed into CMOS inverters or individual transistors [41]. Transformation is also possible through various remote triggers [18]. Fig. 14C shows an example of transformation with a wireless triggering system using an expandable polymer with a heater, as described above [18]. A signal processing system, including analog amplifiers and square waveform generators, is demonstrated. The oscillation frequency changes through the selective degradation of Mg and Al resistors/interconnects through sequential release of a solution of H₂O and NaOH (Fig. 14D) [18]. Similarly, a radio frequency (RF) antenna that gradually reduces in length has been fabricated through selective degradation of Mg and Al and a frequency

change from 1.81 GHz to 1.90 GHz and 2.10 GHz [18].

5. Fabrication processes of transient electronics

Hybrid layers of organic-inorganic materials have remarkable advantages in exploiting excellent electrical performance from inorganics and soft and flexible mechanical properties from organic materials [44]. This enables the application of transient electronics to a wide range of applications, including wearable and disposable patches and/or conformal implantable sensors, which require high performance and mechanical softness [26,27,44,45]. Most biodegradable polymers have limitations in terms of process temperature and solvent compatibility, owing to their low glass transition temperature and high chemical reactivity [26,27,44]. A new fabrication process is required to integrate inorganic electronics on biodegradable or water-soluble substrates by avoiding high-temperature processes and reactive solvent processes [26, 27,45]. Fabrication of transient electronics is preceded by two representative main strategies: transfer printing, which separates reactive materials from electronic fabrication and integrates them after printing, and a solution process that uses degradable inorganic particles in an organic matrix as ink [26,27,45].

5.1. Transfer printing for transient electronic device

Processes for forming electronic devices using silicon are widely available and extremely well-developed. Transfer printing technology enables the integration of nanoscale silicon membranes into a wide range of polymer substrates [15,26,27,44]. The following are representative transfer printing technologies for building Si-based transient electronic devices [15,26,27,44]. Hwang et al. presented the inorganic silicon transient electronics for a Colpitts oscillator circuit using Si NMs as the semiconductor, Mg as the electrode, MgO as the dielectric layer, and silk as the substrate [15]. Si NMs were transferred from a silicon on insulator (SOI) wafer after doping to the silk substrate. Deposition of electronic materials directly onto the silk was carried out through fine-line stencil shadow mask patterning to avoid limitations associated with the substrates' poor chemical resistance, which makes photolithographic processing impossible [15]. It is possible to quickly and easily fabricate the desired electronics without exposure to high temperatures and reactive solvents through stencil shadow masking; however, complex structures are difficult to fabricate because the photolithography process cannot be used [15]. Practical devices with relatively large patterns, such as energy harvesters and transistor arrays, can also be fabricated on a silk substrate by e-beam evaporation and sputtering through a high-resolution stencil mask [15].

Transfer printing of fully formed electronics, which is enabled by the anisotropic etching of a specialized type of SOI wafer using the (111) crystal orientation of the Si handle, was introduced [26]. Fig. 15A shows the fabrication of transient silicon electronics such as MOSFETs (left) and a cross-section view of device after anisotropic etching (right). Transient MOSFETs are fabricated by n-doping by thermal diffusion, isolation by patterned etching, SiO₂ coating by PECVD, buffered oxide etch (BOE) etching, and electron beam evaporation [26]. Encapsulation layers of SiO₂ and Si₃N₄ are deposited through sequential PECVD [26]. The trench is built by etching the top Si and oxide insulator layers with reactive ion etching (RIE), and then anisotropic wet etching of the Si (111) handle wafers along the (110) direction using tetramethylammonium hydroxide (TMAH) to undercut the MOSFETs from the SOI wafer [26]. Released MOSFETs are transferred through a PDMS stamp on a biodegradable polymer, such as a silk substrate [26]. Fabrication based on (111) anisotropic etching has the advantage because it enables on-wafer processing, even at high temperatures; however, bending due to stresses may occur during the undercut process, and a limitation of dimension exists because the undercut must be performed in a specific direction [26]. A similar process of device isolation, metallization, trench etching with RIE, and anisotropic undercut release with TMAH

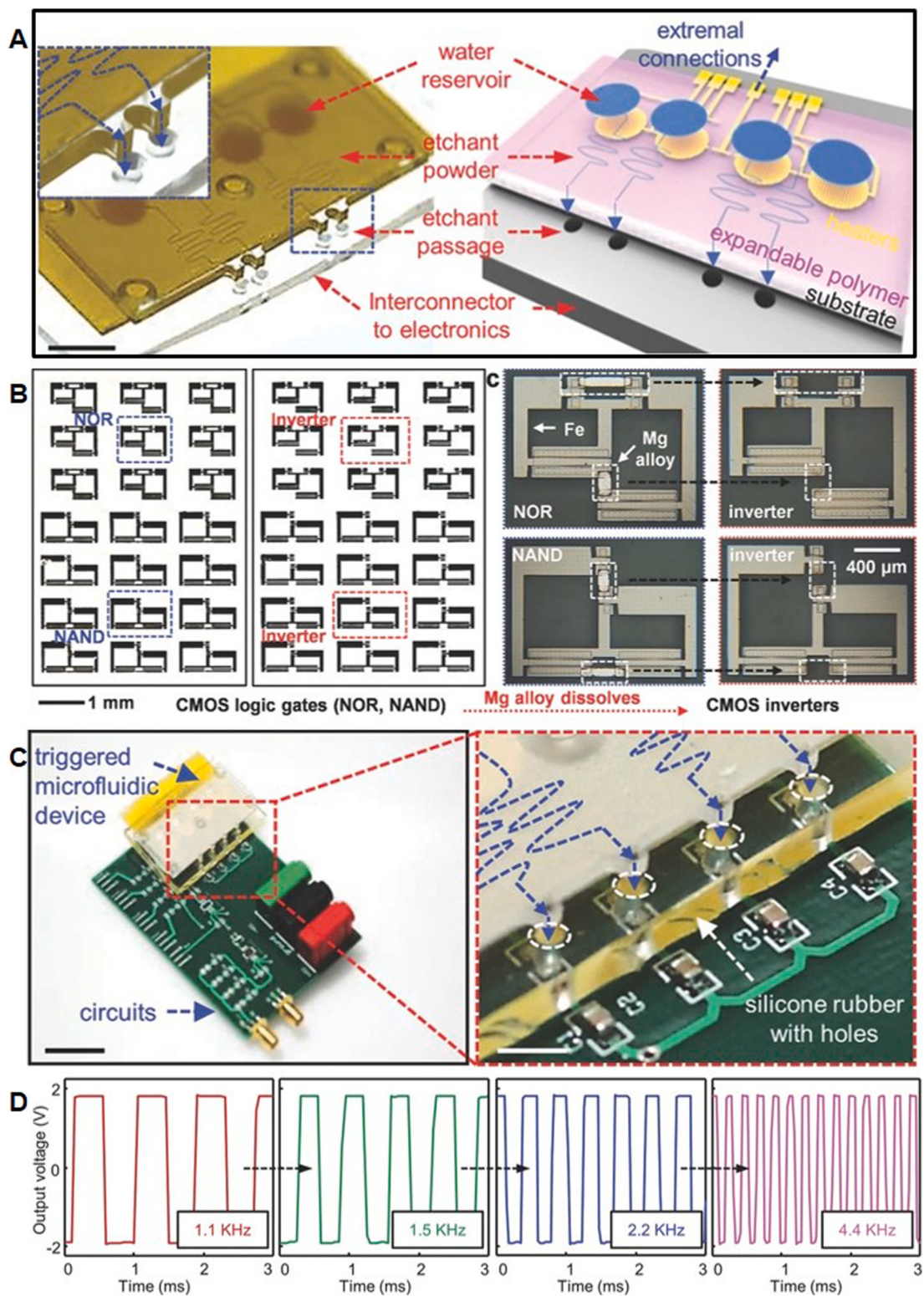


Fig. 14. Trigger transformation for on-demand functional transition.

(A) Wirelessly heat-triggered microfluidic device with thermally expandable polymers for on-demand localized etchant delivery. Adapted with permission from References [18]. © 2015 WILEY-VCH Verlag GmbH & Co. KGaA, Weinheim (B) Transformation from logic gates (NOR: top and NAND: bottom) to inverters through selective degradation by triggering with water. Adapted with permission from References [41]. © 2014 WILEY-VCH Verlag GmbH & Co. KGaA, Weinheim (C) Transformation of signal-processing circuit with wireless heat-triggered microfluidic device; H₂O and NaOH flow results in selective dissolution of Mg and Al resistors interconnects. Adapted with permission from References [18]. © 2015 WILEY-VCH Verlag GmbH & Co. KGaA, Weinheim (D) Transition of oscillation frequency of waveform generated from square waveform generators by selective degradation of circuit. Adapted with permission from References [18]. © 2015 WILEY-VCH Verlag GmbH & Co. KGaA, Weinheim.

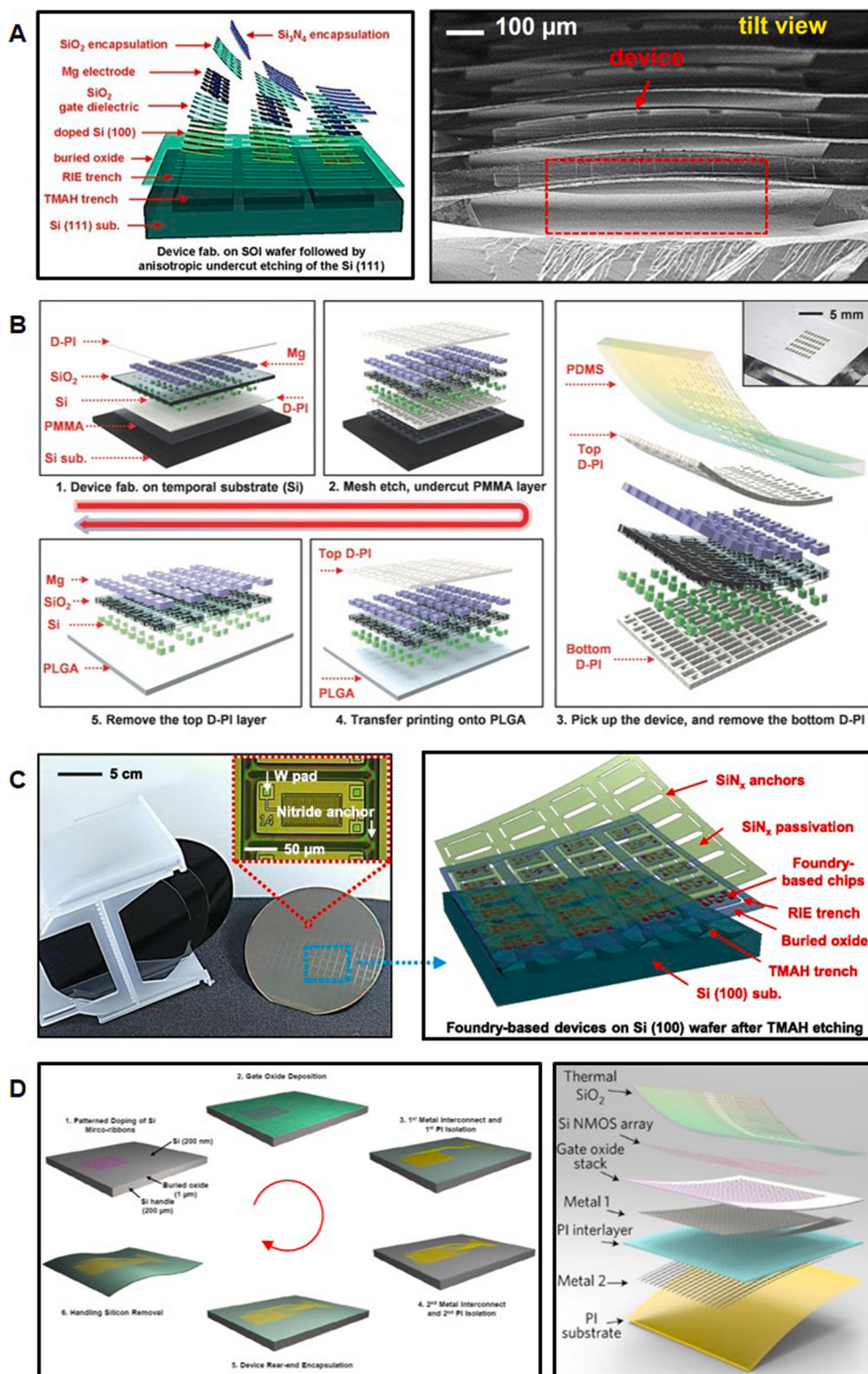


Fig. 15. Advanced transfer-printing methods for inorganic transient electronic devices on biodegradable polymers.

(A) Schematic illustration of an n-channel MOSFET on an SOI wafer with a (111) handle Si and trench structure for undercut using anisotropic etching with TMAH (left) and SEM image of a cross-sectional view of the device after TMAH undercut (right). Adapted with permission from References [26]. © 2013 WILEY-VCH Verlag GmbH & Co. KGaA, Weinheim (B) Fabrication processes in transfer printing of fully formed MOSFETs using PMMA sacrificial layers and dilute PI protective layers. Adapted with permission from References [27]. © 2014 WILEY-VCH Verlag GmbH & Co. KGaA, Weinheim (C) Fabrication process for direct transfer by grinding handle layer and inductively coupled plasma reactive ion etching with SF₆ (STS ICP-RIE) (left); multiplexed Si NM n-MOSFET array made by the process. (right) Adapted with permission from References [116]. © 2017, National Academy of Sciences (D) Image of full wafer-scale foundry-processed array of n-channel MOSFETs (left) and schematic electronics arrays for transfer printing using anisotropic etching after TMAH etching (right). Adapted with permission from References [117]. © 2017, Macmillan Publishers Limited, part of Springer Nature.

can be used to produce not only simple individual MOSFETs but also logic gates or small-scale integrated circuits [26]. More sophisticated circuits, such as NAND or NOR gates, can be manufactured through extended processing or use of interconnect structures after transfer printing [26].

Transfer printing of fully formed electronics is also possible through the use of a sacrificial layer, which separates the fabrication processes from biodegradable substrates [27]. Fig. 15B shows the procedures for fabricating transient electronic circuits using a sacrificial layer [27]. Monocrystalline Si NM is first transferred to a temporary substrate of spin-cast dilute polyimide (D-PI)/poly(methyl methacrylate) (PMMA) bilayer, and then a device is formed by photolithographic patterning of the deposited dielectric and electrode layer [27]. A fully formed device is released through undercutting of the PMMA in acetone. Transfer of the released device to the biodegradable polymer substrate is performed using a PDMS stamp or removable tape [27]. The bottom layer of D-PI is eliminated by RIE while the device is on the PDMS stamp, and the removal of the top layer of D-PI by RIE proceeds after transfer to a biodegradable substrate [27]. The use of a sacrificial layer enables fabrication without the limitation of feature sizes, but it is difficult to proceed with high-temperature processes ($T > 300$ °C) or with extra-large scale fabrication because the process uses a polymer sacrificial layer and two cycles of transfer [27].

Since these fully formed transfer printing processes are compatible with state-of-the-art silicon electronics fabrication, they can be applied to foundry-scale mass production of chip units for complex calculations and logic functions [116]. There have been attempts to apply conventional (100) SOI wafers to large CMOS foundries using XII0 technology from X-FAB semiconductor foundries (Fig. 15C) [116]. This follows release from the underlying substrate with lithographically defined structures and anisotropic wet etching with TMAH [116]. After transfer, the printed device undergoes planarization with a coating of PLGA using an anisole-based solution to prevent devices from washing away during the spin-coating process [116]. The top coating of the PECVD SiN_x layer is used as an encapsulation/passivation layer, which also acts as a strain-compensating layer to prevent the device from bending after release [116]. The transfer of such devices is also used for small and thin devices, even though the target substrate is much wider than the area defined as the source wafer, so it is possible to fabricate a structure in which small devices form an array [116]. All circuit components including the main device layer of Si electronics, SiO₂ dielectric layer, W metal interconnects, PLGA substrate and PECVD SiN_x layer coating have excellent biodegradability, thereby confirming that the foundry chip is sufficiently degradable [116].

(111) anisotropic etching and use of a sacrificial layer makes it possible to print fully formed electronics, but each still has disadvantages, including a dimension limitation and transfer twice [26,27]. A method for direct transfer of the entire device by removing the handle layer of the SOI wafer using a physical method has been proposed [117]. Fang et al. first suggested direct transfer printing by fabricating a multiplexed flexible silicon transistor capable of local signal amplification and multiplexed addressing (Fig. 15D) [117]. Slight grinding the back-side of an SOI wafer is performed first, and after the SOI wafer undergoes conventional silicon fabrication, inductively coupled plasma reactive ion etching (STS ICP-RIE) with SF₆ removes the Si handle wafer completely [117]. Because the etching selectivity of ICP-RIE is very high, removal of the buried oxide (BOX) layer is minimized in the process of erasing Si [117]. By transferring the Si NM and the BOX layer together to the outer perimeter, which is defined by laser cutting, the BOX layer can be used as a dielectric for capacitive coupling and a biofluid barrier [117]. Shin et al. applied this technique to fully bioresorbable pressure sensors with an encapsulation layer of a robust BOX layer using similar fabrication strategies [76]. SiO₂ can be used as an encapsulation layer in transient electronics, so backside etching that enables direct transfer and utilization of BOX as dielectrics simultaneously becomes more important [76].

5.2. Solution process using electronic inks

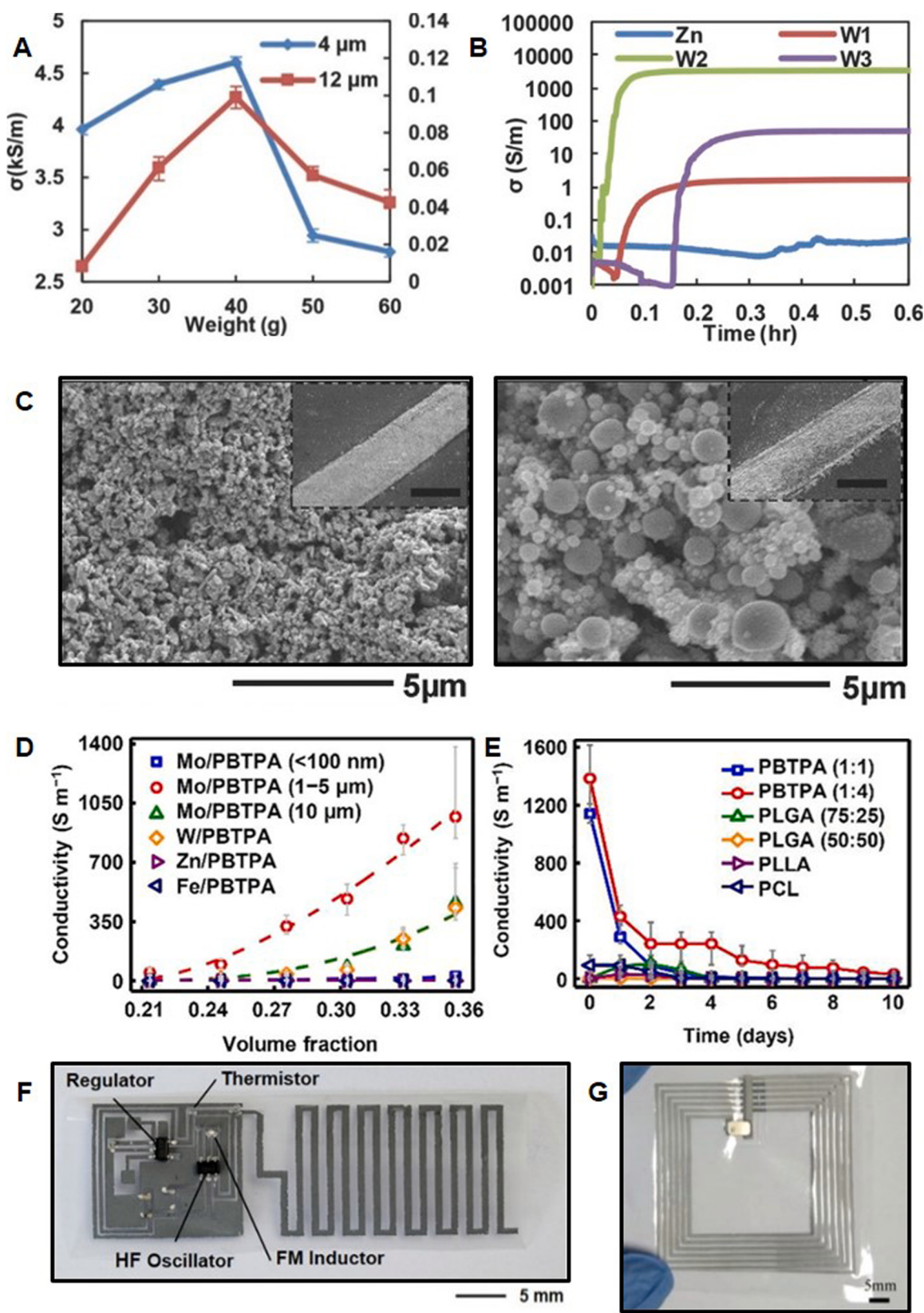
Fabrication by means of a solution process offers opportunities for large-area fabrication by low cost and simple low-temperature processes without harsh conditions [45]. Hybrid composites with sufficient electrical functionality and biodegradability for transient conductors can be prepared by mixing conductive inorganic elements, such as Mg, Zn, and W, and a biodegradable polymer matrix, such as PLGA, poly(ethylene oxide) (PEO), polycaprolactone (PCL) or polyvinyl alcohol (PVA) [45–53]. Printing of hybrid composites makes it possible to fabricate various high-performance and biodegradable electronic devices through screen and ink jet printing [45–53].

Huang et al. demonstrated a transient and conductive printable ink by dispersing a conductive inorganic particle filler of W microparticles (with average diameters of 0.6–1 μm, 4–6 μm, and 12 μm) in a biodegradable polymer matrix binder of PEO [45]. The concentration ratio and particle size of the paste are key factors in determining the conductivity via physical contact. The conductivity changes depending on the concentration of inorganic particles, according to percolation theory: [45]

$$\sigma = \sigma_0(\varphi - \varphi_c)^t \quad (33)$$

In this equation, σ is the composite conductivity, φ is the volume fraction, φ_c is the critical volume fraction according to the percolation threshold, and t is a critical exponent [45]. There is a specific concentration that maximizes the conductivity in Eq. (33) and saturates thereafter [45]. Fig. 16A shows the conductivities of W/PEO pastes at different weights with a binder solution of 1.5 g PEO and 10 g methanol [45]. The conductivity of W(4–6 μm)/PEO paste followed percolation trends, and it reached its maximum value of 4600 S/m when the concentration ratio of W particles was ~75 wt% [45]. The conductivity increased up to a W concentration ratio of 75 wt% as the physical contact area was enhanced and then decreased over 75 wt% due to the reduced binder coverage [45]. Fig. 16B shows the conductivities of PEO pastes with various metal particles [45]. The W paste showed the highest conductivity of 4–6 μm (3500 S/m) because of its polyhedral shape, which makes excellent physical contact [45]. A paste of smaller particles (0.6–1 μm, with a conductivity of 1.6 S/m) had high contact resistance, and a paste of larger particles (12 μm, with a conductivity of 47 S/m) resulted in increased separation between particles, as a result of the greater porosity resulting in reduced physical contact [45].

Physical contact is important in the conductivity of paste [47]. The sintering of conductive pastes significantly enhances physical connectivity and electrical conductivity [47]. Studies have demonstrated several methods of sintering of transient paste using Zn particles. One representative method is photo-sintering, which produces high-intensity light with a broad spectrum of particles that cause meltdown by localized heating through light absorption and recrystallization with forms of large droplets [47–49]. Fig. 16C shows the microstructure of Zn nanoparticle/PVP paste before and after photonic sintering. The particle size and conductivity of the pastes increased from ~135 nm to ~854 nm and from 86.2 S/m to 44642.8 S/m, respectively, through photo-sintering by pulsed light with an intensity of 25.88 J cm⁻² [47]. A UV laser can also be used for photo-sintering of Zn [50,51]. The penetration depth of a UV laser is limited to ~20 μm in densely packed metallic microparticles; thus, a sintering zone is formed only in the top layer, ~20 μm in depth [50]. Photo-sintering methods use heat to induce particle sintering, which can damage biodegradable polymers [47–49]. However, laser-induced photo-sintering can block heat flow to the polymer substrate by forming a composite film of Zn microparticles under the sintering zone, in a manner compatible with many biodegradable polymer substrates [50]. Laser sintering under optimized conditions (1.1-W power, 100-mm s⁻¹ scan speed) forms a highly conductive metal trace consisting of Zn/PVP paste (~10⁶ S/m) with an excellent sheet resistance of 0.02 Ω/□ [50]. Electrochemical sintering based on the



(caption on next page)

Fig. 16. Transient conductive inks for solution process.

(A) Variation in conductivity of W/PEO pastes depending on W concentration (particle size of 4 μm , blue; 12 μm , red). Adapted with permission from References [45]. © 2014 WILEY-VCH Verlag GmbH & Co. KGaA, Weinheim (B) Change in conductivity of PEO pastes made of various metal particles and at curing times at room temperature (Zn, blue; W with particle size of 0.6–1 μm , red; 4–6 μm , green; 12 μm , purple). Adapted with permission from References [45]. © 2014 WILEY-VCH Verlag GmbH & Co. KGaA, Weinheim (C) SEM image of Zn/PVP paste before (left) and after photonic sintering at supply intensity 25.88 J cm^{-2} . Adapted with permission from References [47]. © 2017 WILEY-VCH Verlag GmbH & Co. KGaA, Weinheim (D) Conductivity variation in metal particle/PBTPA inks depending on particle volume fraction (Mo (<100 nm), blue; Mo (1–5 μm), red; Mo (10 μm), green, W (<10 μm), yellow, Zn (<10 μm), purple, Fe (<10 μm), dark blue). Adapted with permission from References [46]. © 2018 Elsevier Ltd. (E) Conductivity change in Mo pastes with various biodegradable polymer matrix including PBTPA (1:1, blue; 1:4, red), PLGA, (75:25, green; 50:50, yellow), PLLA (purple), PCL (dark blue) during dissolution in PBS at 37 °C. Adapted with permission from References [46]. © 2018 Elsevier Ltd. (F) Bioresorbable radio circuit with meander antenna and PCB through-screen printing by electrochemically sintered Zn/PEO paste. Adapted with permission from References [53]. © 2019 WILEY-VCH Verlag GmbH & Co. KGaA, Weinheim (G) Bioresorbable NFC tag connected with screen-printed antenna and conductive coil made of laser-sintered Zn/PVP paste on Na-CMC substrate. Adapted with permission from References [50]. © 2019 WILEY-VCH Verlag GmbH & Co. KGaA, Weinheim (For interpretation of the references to colour in this figure legend, the reader is referred to the web version of this article.).

exchange of Zn and Zn^{2+} is also possible [52,53]. The native passivation layer of Zn is removed through self-exchange between Zn and Zn^{2+} in a buffered acidic solution, and dissolution and deposition of metal from aqueous Zn^{2+} occur simultaneously, resulting in sintering between adjacent particles by atomic diffusion [52]. A conductive Zn/PVP paste ($> 10^5 \text{ S/m}$) with excellent stability was obtained by mixing electrochemically sintered Zn particles with PVP binder in isopropyl alcohol [52]. A study of electrochemical sintering using humidity has also been conducted, since weak acid can damage the substrate [53]. Bioresorbable ink based on anhydride-wrapped Zn nanoparticles has been used in a humid environment [53]. Propionic acid is generated through the localized reaction of anhydride and water, and it removes the native oxide layer of Zn [53]. An excessive number of Zn^{2+} ions is released, and redeposition occurs as free Zn^{2+} ions recombine with electrons of other Zn nanoparticles [53]. Zn nanoparticles with reinforced physical contact are formed through the sintering process, and a Zn/PEO paste with a high conductivity of 72400 S/m is formed [53].

A polymer matrix is also important in swelling, biodegradable behavior, and mechanical properties, while inorganic particles play a crucial role in electrical function. The examples described above used hydrophilic polymers, such as PVP and PEO, but they dissolve too rapidly for most applications, within several hours or even minutes [45, 47–53]. A hydrophobic polymer matrix can slow biodegradation and increase the electrical lifetime because water penetration and swelling decrease [46]. A hybrid composite consisting of a hydrophobic bioresorbable polymer matrix of PBTPA with Mo microparticles is one example [46]. Fig. 16D shows the conductivities of PBTPA pastes with various metals [46]. The conductivity of the Mo/PBTPA paste reaches its maximum value of $\sim 1000 \text{ S/m}$ at an optimal volume fraction of 0.35 [46]. Additionally, Mo microparticles achieve good contact with hydrophobic PBTPA because they form hydrophobic native oxides of MoO_3 , and water permeation can be effectively blocked [46]. Mo/PBTPA paste provided an electric conductivity of $\sim 200 \text{ S/m}$ even after immersion in PBS for 9 days, while pastes with other hydrophilic matrices, such as PLGA and poly-L-lactide (PLLA) lose conductivity within 4 days (Fig. 16E) [46].

Another interesting candidate for a hydrophobic matrix is natural wax, such as soy, myrtle, or candelilla wax, as described previously [95]. Natural wax materials contain long-chain poly- and mono-unsaturated esters, fatty acids, and anhydrides, which make wax hydrophobic [95]. Won et al. produced W microparticles/candelilla wax paste through a straightforward mixing process, and this paste had a maximum conductivity of $\sim 4000 \text{ S/m}$ at a volume fraction of 0.35 [95]. The $\Delta R/R_0$ of the paste remained below a 100 % change for ~ 5 days in DI water at 37 °C, and cracks and further fragmentation occurred after 5 days, leading to dissolution of the particles through water penetration [95]. The ratio of hydrophobic hydrocarbon contents or reactive functional groups varies depending on the type of wax, so natural waxes with various dissolution rates can be used as hydrophobic matrices [95].

Hybrid paste made by mixing conductive inorganic elements and biodegradable polymer binders can be fabricated into various devices through solution processes such as screen and ink jet printing [45,47,50],

[53]. Bikram et al. proposed a circuit that included a battery and LED connected with sintered Zn strips, and the LED showed a stable output, which means that the Zn strips delivered sufficient current [47]. Printed circuit boards (PCBs) were fabricated by stacking commercial off-the-shelf (COTS) components on a bilayer of sodium carboxymethylcellulose (Na-CMC) substrates with an adhesive layer of PEO, using pastes consisting of W or Zn microparticles with a PEO binder [45]. Huang demonstrated a device that harvests RF energy, senses the ambient temperature, and transmits the corresponding data through a wireless signal via a Zn paste [45]. Li et al. fabricated a bioresorbable radio circuit with a meander antenna and PCB through Zn paste by electrochemical sintering with humidity [53]. The output frequency and amplitude of the RF circuit had variations of only 0.2 % and 2.8 %, respectively, which indicates stable operation. The sensitivity of the circuit changed with humidity because the degree of sintering was different (Fig. 16F). [53]. A near field communication (NFC) tag was also fabricated by connecting a fully laser-sintered Zn paste printed antenna with a Zn conductive coil and PVP insulating layer, interconnected to an NFC chip [50]. The NFC tag was fully functional and communicated with an NFC-enabled smartphone until degradation (Fig. 16G) [50].

6. Transient electronic devices and applications

6.1. Electronic component to sensors

A wide variety of transient electronic devices and sensors can be produced by combining biodegradable semiconductors, dielectric conductors, and metal conductors, such as those described in the previous chapter, on flexible biodegradable polymers, including silk fibroin, Na-Ag, PEO, PCL, PVA, PLGA, poly(glycerol sebacate) (PGS), poly(1,8-octanediol citrate) (POC), etc. [15,26–29,45,67]. Transient Si electronics in particular can be used to produce sophisticated devices with performance comparable to conventional Si devices by exploiting Si's versatile electrical, photoelectric, and piezoresistive characteristics [15, 26–29,45,67]. Here, we describe representative transient electronic components and sensors using an Si nanomembrane as a demonstrative example.

Si is a representative semiconducting material with excellent mobilities and a doping concentration-tunable transport characteristics and is thus widely used for active devices and logical circuits [15]. Figs. 17A and B show basic active devices such as PIN diodes and n-MOSFETs produced using an Si NM ($\sim 300 \text{ nm}$ thick) semiconductor, an Mg ($\sim 200 \text{ nm}$ thick) conductor, MgO ($\sim 150 \text{ nm}$ thick) dielectrics, and a silk ($\sim 20 \mu\text{m}$ thick) substrate [15]. The transient diodes showed a forward voltage of $\sim 0.7 \text{ V}$, and the n-channel transient MOSFETs showed a performance with saturation and linear regime mobilities of 560 $\text{cm}^2/\text{V}\cdot\text{s}$ and 660 $\text{cm}^2/\text{V}\cdot\text{s}$, subthreshold slopes of 160 mV/dec (at drain voltage = 0.1 V), and width-normalized current outputs of 0.34 mA/mm (at a gate voltage = 5 V) with an on/off ratio of $>10^5$, which is comparable to that of non-transient conventional Si devices. [15] Integrating active-component transient logical circuits such as NAND, NOR, and an

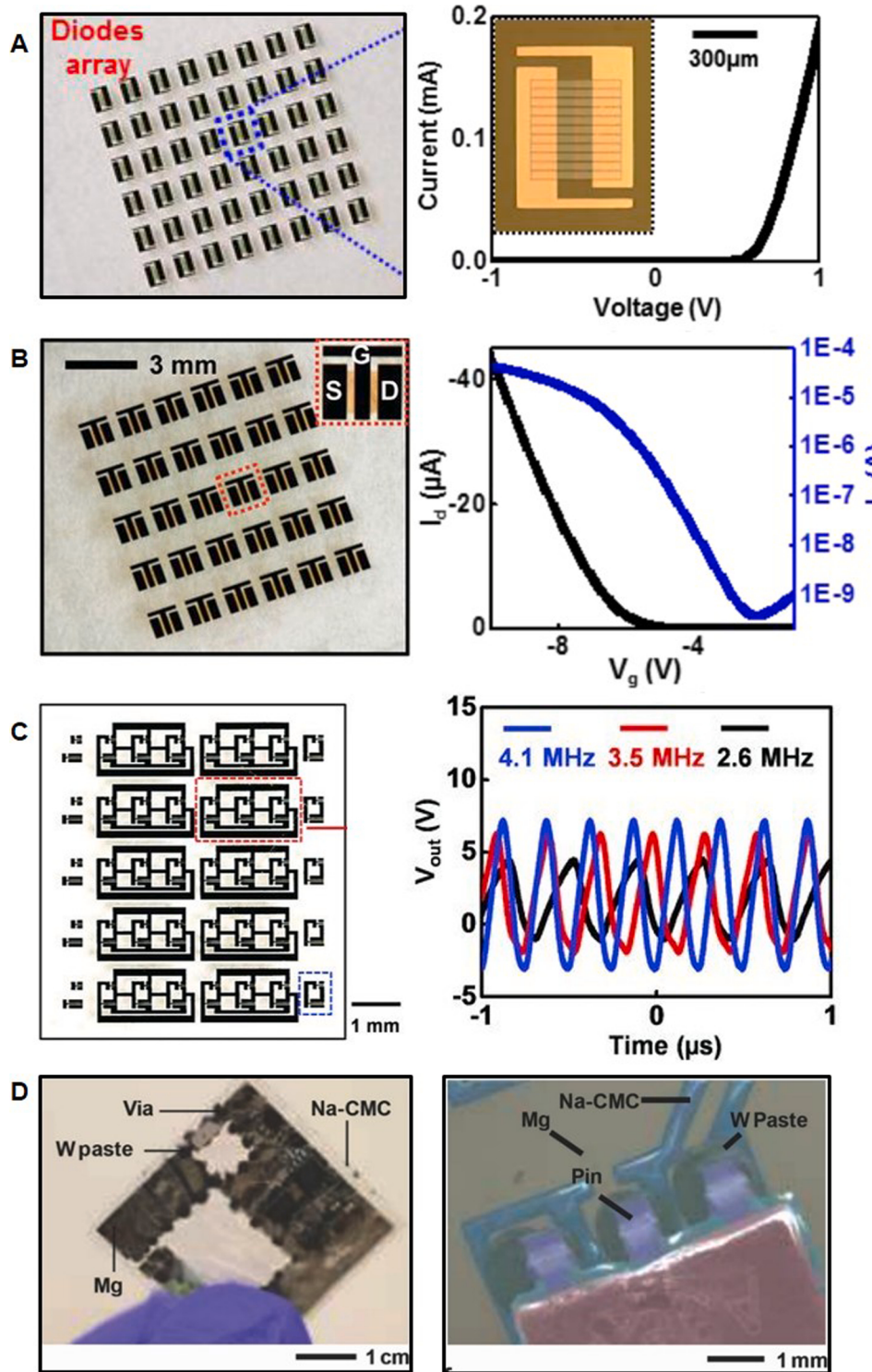


Fig. 17. Transient electronic components and circuits.

(A) Transient Si diode array made of Si NM (~ 300 nm thick) semiconductor, Mg (~ 200 nm thick) conductor, and silk substrate (~ 20 μm thick) (left) and its typical I-V characteristics (right). Adapted with permission from References [15]. © 2012, American Association for the Advancement of Science (B) Array of p-channel MOSFETs made of Si NM (~ 300 nm thick), Mg (~ 200 nm thick) conductor, MgO (~ 150 nm thick) dielectric, and silk substrate (~ 20 μm thick) (left) and representative transfer curve (right) (linear, black; log scale, blue). Adapted with permission from References [15]. © 2012, American Association for the Advancement of Science (C) Image of Si CMOS three-stage ring oscillator composed of Si NMs (~ 300 nm thick), Mg contacts (~ 250 nm thick), and MgO dielectrics (~ 80 nm thick) (left) and time-domain responses at different frequencies (4.1 MHz, blue; 3.5 MHz, red; 2.6 MHz, black) (right). Adapted with permission from References [28]. © 2013 WILEY-VCH Verlag GmbH & Co. KGaA, Weinheim (D) Optical photograph of PCBs fabricated by integrating wireless antennas and resonant coils (left) and colorized SEM image of COTS component (right). Adapted with permission from References [45]. © 2014 WILEY-VCH Verlag GmbH & Co. KGaA, Weinheim (For interpretation of the references to colour in this figure legend, the reader is referred to the web version of this article.).

inverter is also possible by combining n-channel MOSFETs with Mg traces in specific directions after RIE trench etching and transfer [26]. Multiple integration is also possible; for example, an Si CMOS ring oscillator using p- and n-MOSFETs based on Si NMs with Mg contacts and MgO dielectrics is illustrated in Fig. 17C [28]. Many complex circuits, such as PCBs, have been fabricated by integrating various components, such as wireless antennas and resonant coils (Fig. 17D) [45].

The versatile properties of Si, such as photoconductivity, photovoltaic properties, and piezoresistivity, offer diverse opportunities to apply Si transient devices to sensors [15,27,29,67]. Fig. 18A shows a transient

photodetector based on a Si PIN diode using an Si NM channel (~ 1500 nm thick), a Zn electrode (400 nm thick), and an SiO_2 encapsulation layer (~ 50 nm thick) on a PLGA substrate (10 μm). [67] The measured I-V curves change according to the wavelength of the illuminated light, with excellent responsivity sensitivities of 0.135 and $0.133 \text{ A}\cdot\text{W}^{-1}$ and quantum efficiencies of 31.5 % and 26 % for green and red light, respectively, at a dark current of 4.97×10^{-2} nA [67]. Fig. 18B shows transient strain gauges with an Si NM (~ 300 nm thick) resistor with a gauge factor ~ 40 with no significant difference from state-of-the-art devices [15]. Integration of strain gauges with

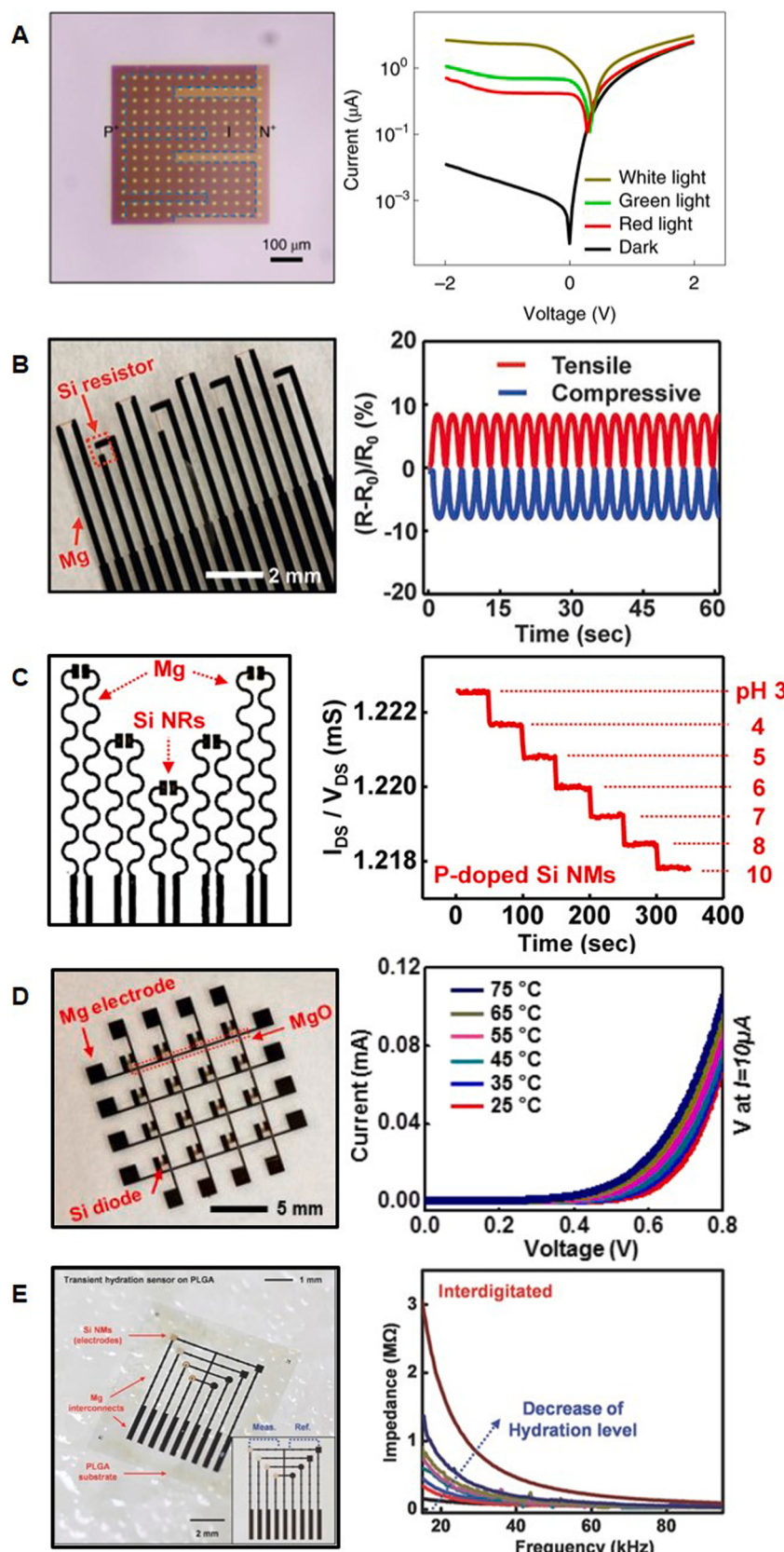


Fig. 18. Representative transient electronic sensors.

(A) Transient photodetector constructed with a PIN diode: Si NM channel (~1500 nm thick), Zn electrode (400 nm thick), SiO₂ encapsulation layer (~50 nm thick) and PLGA substrate (10 μm) (left) and its I-V characteristics under white light (olive), red light (633 nm, red), green light (530 nm, green), and dark environment (black) (right). Adapted with permission from References [67]. © 2019, The Author(s), under exclusive license to Springer Nature Limited (B) Transient strain gauge: Si NM resistor (~300 nm thick), Mg electrodes (~200 nm thick), MgO dielectrics (~150 nm thick) and silk substrate (~20 μm thick) (left) and resistance change during cyclic loading test (tensile strain, red; compressive strain, blue) (right). Adapted with permission from References [15]. © 2012, American Association for the Advancement of Science (C) pH sensor based on Si nanoribbon (300 nm thick), Mg electrodes (300 nm thick), SiO₂ dielectrics (300 nm thick) and POC substrate (left) and change in conductance Si nanoribbon (phosphate doped) from pH 3–10 (right). Adapted with permission from References [29]. © 2012, American Chemical Society (D) Array of temperature sensors using Si NM channel (~300 nm thick), Mg (~200 nm thick) electrode, MgO (~150 nm thick) passivation layer and silk substrate (~20 μm thick) (left) and I-V characteristics at different temperatures (25 °C, black; 35 °C, red, 45 °C, blue; 55 °C, cyan; 65 °C, magenta) (right). Adapted with permission from References [15]. © 2012, American Association for the Advancement of Science (E) Transient hydration sensor made of Si NM electrodes (~300 nm thick), Mg interconnects (200–250 nm thick), SiO₂ interlayer dielectrics (~100 nm thick) and PLGA substrate (~20 μm thick) (left) and its impedance change as a function of frequency with interdigitated electrodes at different hydration levels (119.00, black; 87.30, red; 70.90, blue; 52.40, cyan; 44.00 magenta; 30.90, olive; 16.70, dark blue; in air, brown) (right). Adapted with permission from References [27]. © 2014 WILEY-VCH Verlag GmbH & Co. KGaA, Weinheim (For interpretation of the references to colour in this figure legend, the reader is referred to the web version of this article.).

biodegradable supporting structure materials, such as metal foils, Si membranes, nanoporous Si, pressure sensors, and accelerometers is also possible in transient form [15]. Transient chemical sensors have also been demonstrated [15,27,29]. Fig. 18C shows a pH sensor based on Si nanoribbons (300 nm thick), an Mg electrode (300 nm thick), and SiO₂ dielectrics (300 nm thick) on a POC substrate. Si nanoribbons have been produced with —NH₂ and —SiOH groups on their surfaces through functionalization with 3-aminopropyltriethoxysilane (APTES) [29]. The concentration of charge carriers in the Si nanoribbons changes as -SiOH is deprotonated to -SiO⁻ at high pH, and -NH₂ is protonated to -NH₃⁺ at low pH, thereby changing conductance according to the surrounding pH [29]. The sensitivities were 0.1 ± 0.01 and 0.3 ± 0.02 μS/pH for phosphorus- and boron-doped Si nanoribbons, respectively [29]. Fig. 18D shows a transient temperature sensor based on an Si NM diode [15]. The I-V curve of the diode changed depending on the temperature, and the sensitivity was -2.23 mV/°C (change in voltage for a given current output), which is comparable to that of a conventional sensor [15]. Highly doped Si is used in other types of sensors that use capacitors or conductors as conducting layers but has a wide range of tunability of the dissolution rate [15]. Fig. 18E shows that the hydration sensor

system consists of Si NM electrodes (~300 nm thick) with interlayer dielectrics of SiO₂ (~100 nm) [27]. As the water and ionic contents change according to the surrounding hydration level, the channel impedance amplitude changes steadily depending on the change in conductivity and permittivity [27]. The difference in impedance amplitude shows tendencies similar to those of a conventional non-transient epidermal hydration sensor [27]. All of these sensors are composed of biodegradable materials, such as Si, SiO₂, Mg, MgO, and PLGA, so the sensors dissolve after several days at pH 7.4 PBS at 37 °C [15,26–29,45,67].

6.2. Transient energy devices

Transient energy sources are essential for the operation of transient electronics in various applications. Examples include batteries, capacitors, and energy harvesters, such as photovoltaics, piezoelectric devices, tribogenerators, and others, as a wide range of choices of voltage output, energy density, and conversion efficiency [15,28,35,71,104,118,119]. In this section, we describe representative transient energy sources and their structures and performances.

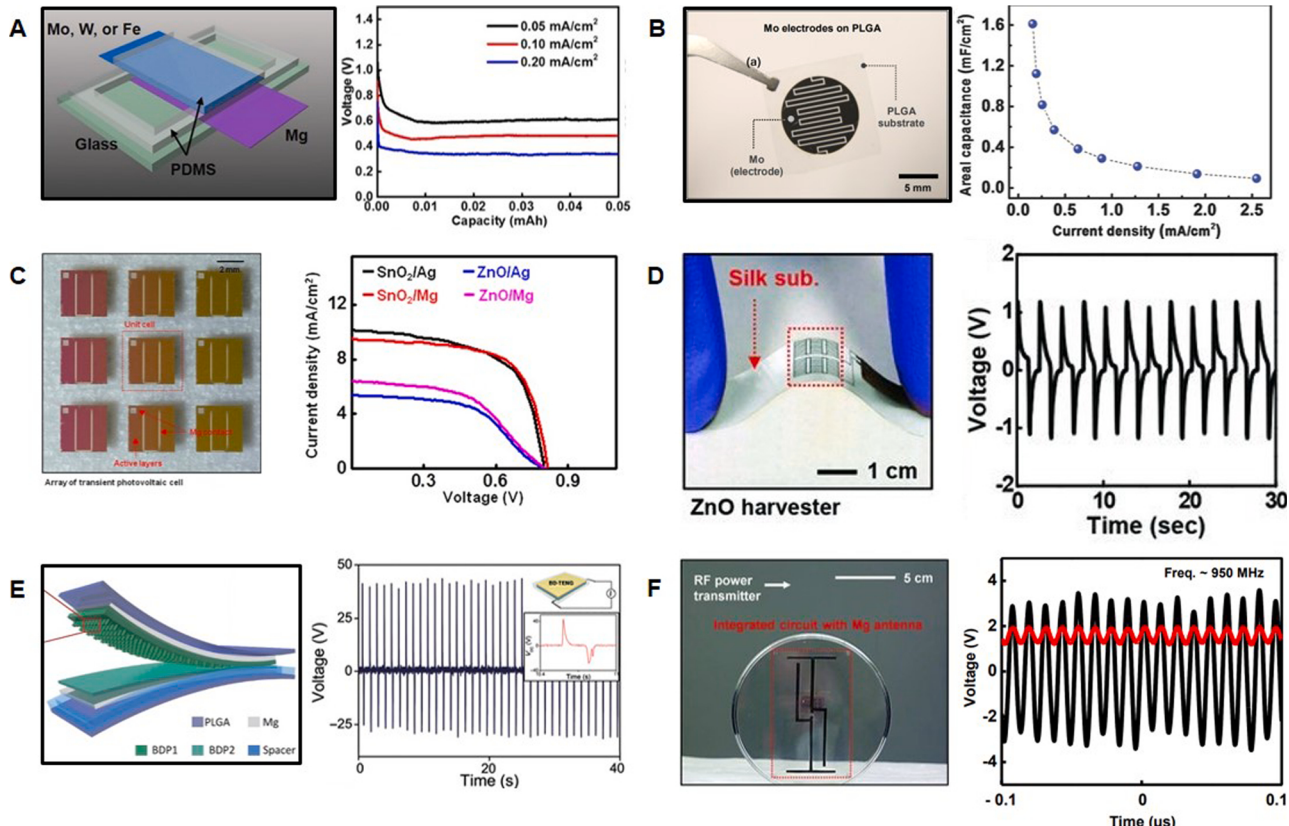


Fig. 19. Transient energy storage and harvester.

(A) Structure of Mg-X (Mo, W, or Fe) battery cell with PDMS liquid chamber filled with PBS electrolyte (left) and output voltage of Mg-Mo battery depending on discharging current density (0.05, black; 0.10, red; 0.20 mA/cm², blue) (right). Adapted with permission from References [104]. © 2014 WILEY-VCH Verlag GmbH & Co. KGaA, Weinheim (B) Biodegradable microsupercapacitor: Mo electrode and agarose hydrogel electrolyte with NaCl salt on PLGA film (left) and areal capacitance of microsupercapacitor as a function of current density (right). Adapted with permission from References [118]. © 2017 WILEY-VCH Verlag GmbH & Co. KGaA, Weinheim (C) Biodegradable thin-film solar-cell array: hydrogenated a-Si diode (230 nm thick), Mg electrodes (~300 nm thick), ZnO transparent conductive oxide (TCO) (~100 nm thick) (left) and voltage-charge density behavior with different combinations of metal electrodes and TCO (Ag metal electrodes and SnO₂:F TCO, black; SnO₂/Mg, red; ZnO/Ag, blue; ZnO/Mg, purple). Adapted with permission from References [35]. © 2015, American Chemical Society (D) Transient mechanical energy harvester: ZnO piezoelectric layer (500 nm thick) between Mg top electrode (500 nm thick) and bottom electrode (300 nm thick) on silk substrate (left) and output voltage during cyclic bending. Adapted with permission from References [71]. © 2013 WILEY-VCH Verlag GmbH & Co. KGaA, Weinheim (E) Transient triboelectric nanogenerator: biodegradable polymer friction layers (100 µm thick) and spacer (200 µm thick), Mg electrode (50 nm thick) with PLGA encapsulation layer (100 µm thick) (left) and electrical voltage generated by applying external forces (right). Adapted with permission from References [119]. (F) Transient wireless RF power scavenger circuit with Mg receiving antenna (left) and output voltage at frequency 950 MHz (right). Adapted with permission from References [28]. © 2013 WILEY-VCH Verlag GmbH & Co. KGaA, Weinheim (For interpretation of the references to colour in this figure legend, the reader is referred to the web version of this article.).

Batteries provide high energy density and instant readiness and thus are the most widely used power sources [104]. Transient galvanic batteries, as representative primary batteries, can generate current with spontaneous redox reactions from the difference in redox potential between the biodegradable anode and the cathode [104]. The main electrochemical reaction usually follows [104]

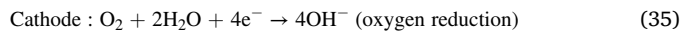


Fig. 19A shows a fully transient galvanic cell composed of Mg foil as the anode material, biodegradable metal foils such as Fe, W, and Mo as the cathode materials, and PA as the encapsulation layer [104]. The operation voltages were ~ 0.75 V, ~ 0.65 V, and ~ 0.45 V for Fe, W, and Mo, respectively, under a constant discharge current density of 0.1 mA cm^{-2} . A battery using Mo foil as a cathode had a specific capacity of $\sim 276\text{ mAh/g}$ and showed stable performance for more than 24 h, losing nearly half of its capacity within 1–2 days in PBS due to degradation of the Mg foil [104]. Stacking single cells increases the output voltage: for example, stacking four Mg–Mo batteries increases the output voltage from ~ 0.45 V to ~ 1.6 V [104]. Subsequent research was conducted to improve the performance of transient batteries by combining diverse materials. An $Mg_{100-x}Zn_x$ ($0 \leq x \leq 100$) system or Mg–Zn–Zr alloy was used for the anode to improve the corrosion resistance [120]. The cathode materials, such as MoO_3 , can be alternated to obtain a high stable output voltage of up to 1.6 V for a single cell [121]. A fully organic battery consisting of cellulose membranes, carbon paper electrodes, beeswax impermeable coatings, and organic redox species is also able to achieve a high output voltage (1.5–3.0 V) [122]. Fabrication of a water-soluble secondary battery using Li described in previous transient trigger section is also possible in transient form [103]. Recently, a biodegradable sodium-ion secondary battery (SIB) constructed using sodium- and iron-based polyanion compounds such as $Na_4Fe_3(PO_4)_2(P_2O_7)$ (NFP) as cathode, pyroprotein-based carbon anode, propylene carbonate electrolyte, cellulose-based separator, and cellulose/polyester/silicon-based package materials [123]. All materials used in the battery have adequate biodegradability, as most components show a noticeable mass decrease of $\sim 10\%$ after 120 days of fungal inoculation; especially, the electrolyte shows a mass decrease of $\sim 100\%$ without any toxic remains [123]. Biodegradable SIB exhibited a reasonable electric performance compared with batteries using commercial binders with specific charge-discharge capacity of $\sim 110\text{ mA g}^{-1}$ and cycle retention of $\sim 93\%$ after 100 cycles at a current rate of 20 mA/g [123].

Microsupercapacitors are additional candidates for transient energy storage. Microsupercapacitors provide high power densities and are mainly used as back-up energy sources [118]. **Fig. 19B** shows transient microsupercapacitors consisting of biodegradable Mo films (300 nm thick), a biopolymer hydrogel electrolyte with NaCl salt (agarose gel), and a PLGA substrate with a PA encapsulation layer [118]. Microsupercapacitors form an electrical double layer on the interface between the electrode surface and electrolyte and store energy electrostatically through the adsorption of ions in the electrolyte to the electrode surface [118]. Pseudocapacitance from the additional redox reactions of the metal oxide coating formed by electrochemical corrosion of the interface between the metal electrode and the hydrogel electrolyte improves the performance of the microsupercapacitors [118]. Microsupercapacitors using Mo-interdigitated electrodes showed an areal capacitance of 0.16 m F cm^{-2} , an energy density of $0.14\text{ }\mu\text{W}\cdot\text{h cm}^{-2}$, and a power density of 1.0 mW cm^{-2} , which are comparable to those of a nontransient device [118]. The capacitance of Mo microsupercapacitors increases dramatically, up to 20 times the initial value, over approximately 3000 cycles, owing to additional redox reactions induced by the growth of metal oxide [118]. The capacitance decreases after ~ 3000 cycles

because of a decrease in ion mobility that occurs as the hydrogel dries and a reduction in current collection efficiency that occurs as the metal oxide film becomes thicker [118]. Mo-interdigitated electrodes were completely degraded after 9 days in pH 7.4 PBS at 37°C and showed stable performance until degradation [118]. The output voltage increased up to 2.1 V, but the cell capacitance was reduced by 1/3 by connecting three capacitors in series [118]. Hereafter, a more advanced biodegradable microsupercapacitor composed with two-dimensional, defective amorphous MoO_x flakes on Mo foil as a binder-free pseudocapacitance electrode, biodegradable Na-AG gel electrolyte, and PVA-/PLA as package materials was demonstrated [124]. The microsupercapacitor with the MoO_x flake electrode showed higher electric performance with areal capacitance of 112.5 m F cm^{-2} at 1 mA cm^{-2} , energy density of $15.64\text{ }\mu\text{W}\cdot\text{h cm}^{-2}$, and power density of 2.53 mW cm^{-2} . The MoO_x flake was completely separated from the Mo foils and microsupercapacitor fully disintegrated after immersing in PBS (10 mM, pH 7.4) at 37°C for 1 month [124].

Scavenging surrounding energy into electrical energy is an effective approach to continuously deliver power to transient electronic devices. Various energy sources, such as light, mechanical energy, and electromagnetic energy, can be harvested for energy through specific materials or structures [15,28,35,71,119]. Transient photovoltaics using single-crystalline Si and amorphous Si are examples of light energy collection devices [15,35]. A biodegradable ultrathin Si solar cell composed of a thin Si layer ($\sim 3\text{ }\mu\text{m}$ thick), an Mg electrode, and a silk substrate was demonstrated to have a power conversion efficiency of $\sim 3\%$ at a 66 % fill factor, which is comparable to that of a thin conventional cell without light-trapping structures, backside reflectors, or antireflection coatings [15]. **Fig. 19C** shows a thin and flexible amorphous Si solar cell consisting of a hydrogenated a-Si film ($Si:H$, 230 nm thick) with a PIN doping profile (20-nm-thick n-region with $\sim 10^{20}\text{ cm}^{-3}$ P doping, a 200-nm-thick undoped region, and a 10-nm-thick p-region with $\sim 10^{20}\text{ cm}^{-3}$ B doping) as the active material, a ZnO film with Al dopant ($\sim 100\text{ nm}$ thick) as the transparent conductive oxide, and Mg electrodes ($\sim 300\text{ nm}$ thick) [35]. An a-Si solar cell exhibited an efficiency of 2.6 %, open-circuit voltage of 0.81 V, and short-circuit current density of 6.4 mA/cm^2 [35]. The ZnO and Mg conducting layer quickly dissolved within a few hours when immersed in DI water at RT, resulting in a rapid decrease in the short-circuit current density and open-circuit voltage, and the a-Si dissolved completely after several days [35].

A mechanical energy harvester is another useful energy scavenging device. **Fig. 19D** shows a piezoelectric energy harvester consisting of a ZnO thin film (500 nm thick) as the piezoelectric component, Mg electrodes (300 nm/500 nm thick for the bottom and top electrodes), and a silk substrate ($\sim 25\text{ }\mu\text{m}$ thick) [71]. ZnO also shows a strong piezoelectric response in which the electrical charge of the dipoles is aligned and net electric polarization occurs as a mechanical stress is applied, which produces an electric potential [71]. When electric oscillation occurs through mechanical vibration, the piezoelectric components operate as a power source [71]. A piezoelectric energy harvester showed an output current of $\sim 0.55\text{ nA}$, an output voltage of $\sim 1.14\text{ V}$, and a power density of $\sim 10\text{ nW/cm}^2$ with 0.28 % energy-conversion efficiency under bending [71]. All of the electronic materials completely dissolved after 15 h in DI water at RT [71]. A triboelectric generator that uses friction between different biodegradable polymers is another example of a mechanical energy harvester [119]. **Fig. 19E** shows a transient triboelectric nanogenerator consisting of PLGA, PVA, PCL, and poly (3-hydroxybutyric acid-co-3-hydroxyvaleric acid) (PHB/V) [119]. The biodegradable triboelectric generator has a multilayered structure consisting of the PLGA encapsulation structure (100 nm thick), friction layers, spacers of biodegradable polymers (50–100 μm and 200 μm thick, respectively), and an Mg electrode (50 nm thick) [119]. Electron flow between electrodes is induced through triboelectrification and electrostatic induction as contact between two friction layers occurs by external force, and a pulsatile AC electrical output is generated through periodic external force [119]. A triboelectric nanogenerator exhibited

an open-circuit voltage of ~ 40 V, short-circuit current of ~ 1 μ A, and power density of 32.6 mW/m 2 at a motion frequency of 1 Hz [119]. The triboelectric generator lost its structural integrity and degraded after 50 days at pH 7.4 PBS at 37 °C [119].

RF energy harvesting devices, such as antennas and inductor coils, are excellent tools for wirelessly transferring energy. Fig. 19F shows a transient wireless RF power scavenger circuit consisting of Si NM (300 nm thick) as the semiconductor, Mg (150 -nm-thick and ~ 3 - μ m-thick first and second layers, respectively) as the conductor, SiO₂ (900 nm thick) as the interlayer dielectrics, and silk as the substrate [28]. The system consists of an Mg RF antenna, an inductor, six capacitors, a resistor, and eight diodes [28]. An Mg antenna operating at a frequency of 950 MHz is connected to the circuit, and the system scavenges energy through an RF transmitter with a power of 54 mW and power conversion efficiency of 15.7 % [28]. All of the electronic materials are biodegradable in DI water at RT, where the circuit is disintegrated as the silk dissolves first and the rest of the materials dissolve completely over time [28].

6.3. Biomedical applications

Among the important applications of transient electronics are biodegradable medical devices that do not require a secondary surgery to remove implants after their operational lifetime ends. An implant acts as a nidus site for biofilm formation resulting from reaction with infection agents, such as bacteria and virus and migrate inside the body cavity, so damage tissues and organs, and interrupt regular metabolism [8–11,73,125–128]. For example, migration of the pocket and erosion of wires are major accidents that can occur with implantable pacemakers [129]. Extraction surgery poses additional surgical risk, along with the risks of secondary infection and other complications [8–11,73,126,126,127,128]. Biodegradable forms of electronics can provide a wide range of sensing and treatment options without residue or removal surgery [8–11,73,126,126,127,128]. Transient electronics in biomedical applications are currently developed in various aspects, but the discussion regarding biocompatibility still remains at the level that there is no abnormal effect. Long-term safety issues including comprehensive investigation of the device/tissue interface and the metabolic processes of degradation products are necessary to be investigated from multiple perspectives. Maintaining a constant lifetime regardless of the diverse external stimuli is another critical challenge of the transient electronics. Especially, biodegradable polymers show the change in lifetime due to swelling very frequently, so most transient electronic systems construct their own independent passivation system [130,131].

6.3.1. Biodegradable electronics in diagnostic applications

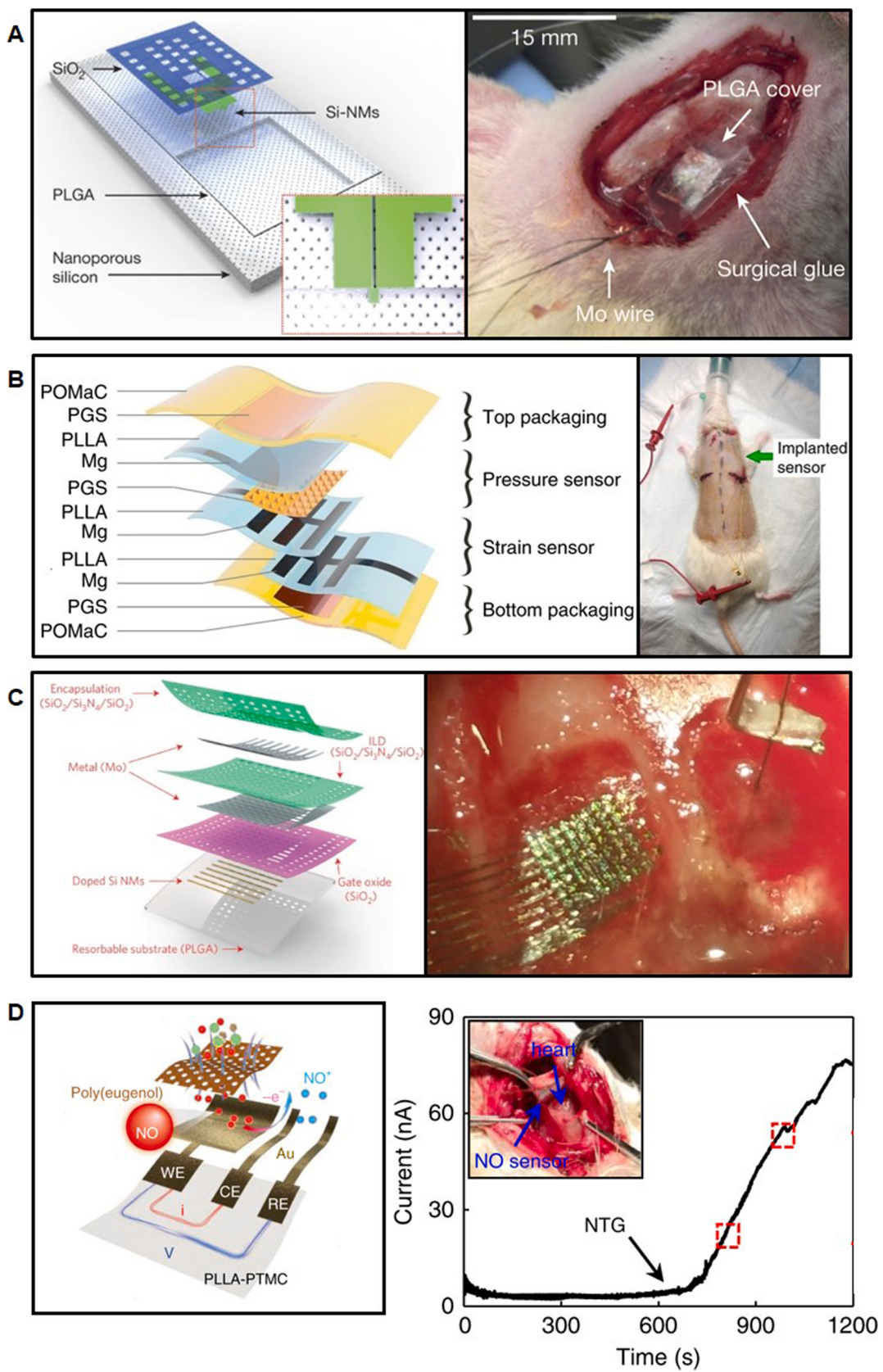
Biodegradable electronics are very useful in monitoring acute diseases with latent periods, such as traumatic brain injury. Local bleeding caused by external shock to the brain can continue to increase local pressure for about 10 days [132]. Continuous intracranial pressure monitoring after initial injury is very useful in identifying the progress of recovery following a traumatic brain injury [9]. Fig. 20A shows an of a bioresorbable intracranial pressure (ICP) sensor integrated with a temperature sensor [9]. The sensor consists of a strain gauge of serpentine Si NM (300 nm thick) on a PLGA (30 μ m thick)-sealed nanoporous silicon (60 – 80 μ m thick) substrate with an encapsulation layer of SiO₂ [9]. The resistance of the sensing element increases linearly with a slope of 83 Ω (mmHg) $^{-1}$ as the ICP increases to 0 – 70 mm Hg through the piezoresistivity of Si NM during deflection of the PLGA membrane into the air cavity [9]. The ICP sensor was implanted in the intracranial space of a rat with a biodegradable Mo wire coated with PLGA and connected wirelessly to an external data transmission system [9]. Rapid increases and decreases in ICP resulting from periodic manual abdominal compression activating the Valsalva maneuver and gradual increases and decreases in ICP through Trendelenburg and reverse Trendelenburg showed excellent *in vivo* sensing performance, comparable to the clinical

standard of a wired ICP sensor, for up to three days [9]. Recently Shin et al. demonstrated the use of an ICP sensor with an enhanced lifetime (25 days) using thermally grown silicon SiO₂ as an encapsulation layer in rats [76]. Continuous and wireless monitoring with biodegradable pressure sensors is also effective for intracranial, intraocular, and intravascular sites in diagnosing glaucoma and hypertension and monitoring recovery from brain injury [76]. Biodegradable pressure sensors are one of the most common platforms in diagnostic applications, such as the recent demonstration about blood flow monitoring by measuring arterial pulse through a biodegradable pressure sensor based on fringe-field-capacitive sensing [133].

Post-surgical monitoring of recovery and rehabilitation is also possible using biodegradable electronics. Fig. 20B shows fully degradable strain sensors for monitoring mechanical forces on tendons, based on an Mg thin-film capacitor (100 nm thick) with PGS (50 μ m thick) and poly(octamethylene maleate (anhydride) citrate) (POMaC) (500 μ m thick) as elastomers and PLLA packaging (50 μ m thick) [126]. The sliding of two thin-film comb electrodes relative to each other by strain induces a change in the effective area and distance of the capacitor, resulting in a change in capacitance [126]. Strain sensors and pressure sensors have excellent sensitivities in comparison to conventional sensors, which can distinguish strains as small as 0.4 % and pressures as low as 12 Pa, without impeding the natural movement of the tendon [126]. Biodegradable elastomers of PGS and POMaC have been shown to improve strain cycling stability up to 54 % [126]. The sensor system showed stable performance in the bodies of rats, successfully measuring physiological strain signals for more than two weeks and then slowly degrading [126].

A biodegradable physiological sensor enables recording of *in vivo* electrophysiological signals. Fig. 20C shows a neurophysiologic monitoring system that can diagnose and treat various brain disorders [10]. Highly doped Si NMs electrodes ($\sim 10^{20}$ cm $^{-3}$, thickness of ~ 300 nm), an SiO₂ insulating layer, and a PLGA substrate make up the monitoring system, and Si NM arrays constitute a bioresorbable neural interface for recording normal physiological and epileptic activity in electrocorticography (ECoG) and subdermal encephalography (EEG) [10]. High-resolution spatiotemporal mapping of large areas is possible using a fully biodegradable actively multiplexed sensing system [10]. The 8×8 embodiment includes 128 MOSFETs based on Si NMs (300 nm thick) as the active semiconductor and neural interface electrode, Mo (300 nm thick) as the electrode, SiO₂ (~ 100 nm thick) gate dielectrics, and a trilayer of SiO₂/Si₃N₄/SiO₂ (300 nm/ 400 nm/ 300 nm thick) as the interlayer dielectric [10]. Bioresorbable electrode arrays were implanted in the barrel cortex of an anesthetized rat, and spatial distributions of low-amplitude evoked cortical activity corresponding to the barrel cortex and estimated relative location were recorded by stimulating different whiskers [10]. The measured spatial distribution was consistent with the relative location of the activated whiskers on the barrel cortex as described in a color map, which confirms the ability to record stimulus-evoked and drug-induced neural activity [10]. This monitoring system exhibited sensor performance and tissue reactivity reduction comparable to a conventional clinical system [10]. This system can be applied to neural interfaces as well as other situations in which transient monitoring and modulation of physiologic functions are needed [10].

A biodegradable chemical sensor is another possible diagnostic application of transient electronics. Fig. 20D shows the transient NO sensor composed of biodegradable substrate (copolymer of poly(L-lactic acid) and poly(trimethylene carbonate), PLLA-PTMC; thickness: 400 μ m), ultrathin gold nanomembrane electrodes (thickness: ~ 32 nm), and biocompatible poly(eugenol) film (thickness: ~ 16 nm) as the selective membrane [134]. Real-time monitoring of NO levels plays a crucial role in neurotransmission, inflammatory responses, and cardiovascular systems [134]. Detection of NO proceeds through amperometry based on three-electrodes configuration with Au nanomembranes [134]. The redox reaction including the oxidation of NO follows:



(caption on next page)

Fig. 20. Biodegradable electronic sensors for biomedical monitoring.

(A) Schematic illustration of biodegradable pressure sensor: Si NM piezoresistive gauge (300 nm thick), SiO_2 encapsulation (100 nm thick) and PLGA membrane (30 μm thick) sealing trench of nanoporous Si structure (60–80 μm thick) (left) and implantation image of bioresorbable pressure sensors in rat intracranial space (right). Adapted with permission from References [9]. © 2016, Nature Publishing Group, a division of Macmillan Publishers Limited (B) Exploded view of the structure of a fully biodegradable strain and pressure sensor using Mg electrode (100 nm thick), PGS dielectric layer (50 μm thick), POMaC elastomer (500 μm thick) and PLLA substrate (50 μm thick) (left) and application to biodegradable strain and pressure sensor on the back tendon of Sprague-Dawley rat (right). Adapted with permission from References [126] (C) Schematic illustration of transient multiplexed sensing: Si NM active channel (~300 nm thick), SiO_2 dielectric (~100 nm thick), Mo electrode (~300 nm thick), encapsulation trilayers of $\text{SiO}_2/\text{Si}_3\text{N}_4/\text{SiO}_2$ (~300 nm/400 nm/300 nm thick) on PLGA substrate (~30 μm thick) (left) and image of implanted multiplexed electrode array on the cortical surface of rat left hemisphere (right). Adapted with permission from References [10]. © 2016, Nature Publishing Group (D) Schematic of transient NO sensor: PLLA-PTMC substrate (thickness: 400 μm), ultrathin gold nanomembrane electrodes (thickness: ~32 nm), biocompatible poly(eugenol) selective membrane (thickness: ~16 nm) (left) and image of implanted NO sensor in the joint cavity of New Zealand white rabbits with real-time measurement of the redox current (right). Adapted with permission from References [134]. © 2020, The Author(s), under exclusive license to Springer Nature America, Inc.



The NO concentration can be monitored by measuring the redox current between the working electrode and the counter electrode while an oxidation potential is applied between the working electrode and the reference electrode. The current response rapidly increases as the NO concentration increases [134]. The transient NO sensor showed remarkable performances with a low detection limit (3.97 nmol), a wide sensing range (0.01–100 μM), high temporal resolution (< 350 ms), and anti-interference characteristics. [134]. A transient NO sensor is implanted in the joint cavity of a New Zealand white rabbit for *in vivo* NO monitoring, with nitroglycerine (NTG) injection that releases NO to expand the vascular system for treatment of cardiovascular diseases such as angina pectoris through the ear vein of New Zealand white rabbits [134]. The response current of the NO sensor immediately increased after NTG insertion, indicating that the NO concentration in the heart region increased [134]. The NO sensor was also able to record electrocardiography (ECG) signals through NO detection, so the NO sensor can properly adjust the NTG dose [134].

6.3.2. Biodegradable electronics in therapeutic applications

Biodegradable electronic devices can also deliver stimuli to modulate biological responses or neuron activity or trigger drug delivery. Fig. 21A shows a wireless electrical stimulator used to accelerate functional recovery from peripheral nerve injury [11]. The device includes an energy harvester consisting of a loop antenna with a bilayer, a dual-coil configuration ~50 μm thick Mg, an RF diode made of Si NM with an Mg electrode, a parallel plate capacitor made of Mg ~50 μm thick, an SiO_2 passivation layer, and a PLGA substrate [11]. Electrical stimulation applied to the targeted sciatic nerve in a controlled manner enhances and accelerates the functional recovery of the cross-section nerve [11]. Monophasic cathodic electrical impulses (duration of 200 μs , frequency of 200 Hz) were activated over the course of one hour using an external source of RF power with a transmitting coil supplied to a transmission antenna [11]. The evoked maximum amplitude of electromyogram (EMG) response and muscle force increased with electric stimulation, indicating that electric stimulation helps nerve recovery effectively [11]. In addition, muscle mass was degraded to a smaller degree in the presence of electrical stimulation eight weeks after the injury [11]. The electromyograms and muscle force were much higher for a stimulation time of six days than for stimulation times of one or three days [11]. The entire system disintegrated completely within 25 days, and negligible damage was observed on the nerve–cuff interface, confirming that the device had excellent biodegradability and biocompatibility [11]. Stimulator is a still attractive choice as an effective therapeutic platform for various diseases treatment and wound healing processes. A nerve stimulator utilizing bioresorbable dynamic covalent polyurethane (b-DCPU) as a substrate and biofluid barrier was demonstrated recently, and it provides excellent mechanical stretchability and minimal swelling to ensure more robust operation in moving tissues

[135]. Wang et al. demonstrated another sophisticated stimulating platform for neuroregenerative medicine using dissolvable galvanic cells composed of Mg thin films and FeMn alloy electrodes on a polymer-based scaffold, where electroactive galvanic cells not only stimulate the calcium activity and neurite outgrowth of DRG neurons but also promote the proliferation of Schwann cells and up-regulation of neurotrophic factor [136].

Thermal therapy can help recovery by removing an infection source. An initial programmable transient thermal therapy system using inductive coils of Mg with resistive microheaters of Si NMs on a silk substrate was demonstrated [127]. The fully transient version was implanted under the skin of a BALB/c mouse with localized heating ΔT of ~5 °C [127]. Fig. 21B shows the implantation of a posterior wireless heating system consisting of Mg as the serpentine resistor heater, a power-receiving coil, and an MgO interlayer dielectric with silk as the substrate and encapsulation layer into BALB/c mice [127]. Wireless inductive power transfer was possible through near-field coupling, and the system maintained localized heating ΔT of ~20 °C for 10 min or more as the primary coil was operated at a wireless power of 500 mW at 80 MHz [127]. Heat treatment at 100 mW and 500 mW for 10 min by implantation into infection sites of BALB/c mice resulted in increases in skin temperature up to 42 °C and 49 °C, and the bacterial count was significantly decreased after 24 h [127]. Some residues of the Mg-inductive coil were found inside the mice after 7 days, but they dissolved completely after 15 days [127].

Transient drug delivery by remote triggering is another effective medical application. Pharmacological treatment with drug delivery vehicles for various diseases, such as hormone imbalances, malignant cancers, osteoporosis, and diabetes, is possible [137]. A remote drug delivery system consisting of temperature-sensitive lipid-based layered films (dipalmitoylphosphatidylcholine, 1,2-dilauroyl-sn-glycero-3-phosphoethanolamine, dipalmitoylphosphatidylglycerol or 1,2-dioleoyl-3-trimethylammonium-propane and cholesterol, 12–30 μm thick) encapsulating various drugs and 2 × 2 arrays of inductive coils, resistive heaters, and interconnects with Mo foil (15 μm thick) on a PLGA substrate (200 μm thick) has been demonstrated [8]. The lipid film wraps around the drug evenly and keeps it enclosed until it reaches the desired point [8]. The lipid film is then rapidly heated to a critical temperature (41–43 °C, lower than the maximum allowable temperature for body tissues, 43–45 °C) through remote heating by wireless power with inductive coils, which results in the release of the drugs via expansion of the drug reservoir [8]. Drug stabilization and delivery by remote heat triggering have also been performed in a similar manner using a silk matrix [8]. The use of temperature-sensitive polymers has relatively poor mechanical stability because of weak molecular bonding, which results in initial leakage of drugs [8,128]. Fig. 21C shows a drug delivery system that includes a mechanically stable PBTPA reservoir (~100 μm thick) with complete sealing by an Mg and Mo metal gate, which permits more effective blocking of drug leakage until triggering [128]. This system involves a single reservoir with Mg electrodes and a wireless power harvester based on magnetic inductive coupling to an external transmission coil, which consists of an Mg RF coil, an Si NM RF

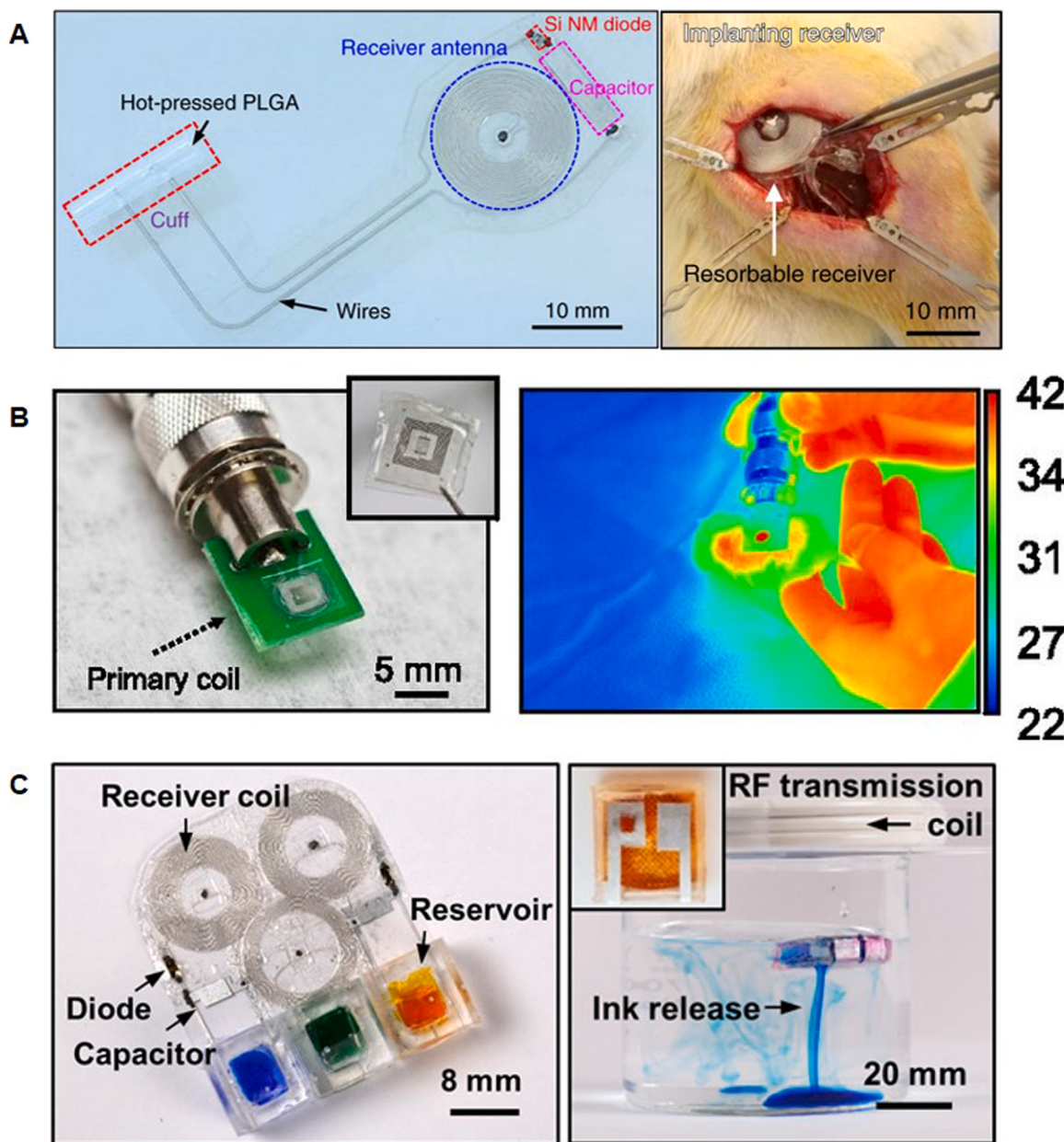


Fig. 21. Biodegradable actuators for therapeutic treatment.

(A) Biodegradable wireless electrical stimulator: loop antenna of Mg (~50 µm thick), RF diode using Si NM (~320 nm thick) channel and Mg (~300 nm thick) electrode, and plane capacitor of Mg/SiO₂/Mg (50 µm /600 nm/50 µm thick) on PLGA substrate (~30 µm thick) (left) and its application to sciatic nerve for functional regeneration (right). Adapted with permission from References [11]. © 2018, The Author(s), under exclusive license to Springer Nature America, Inc. (B) Biodegradable wireless heater using Mg resistor-heating element (~200 nm thick) and Mg inductive coil (~2 µm thick) with MgO passivation layer (~1 µm thick) on silk substrate (~50 µm thick) (left) and IR image after implanting heater at infection site of BALB/c mouse during wireless heating (right). Adapted with permission from References [127]. © 2014, National Academy of Sciences (C) On-demand wireless drug-delivery vehicle with triple reservoir and different colored inks: PBTpa reservoir (~100 µm thick) sealed with Mg metal gate (50 µm thick), Mg electrodes (30 µm thick) and wireless power harvester based on Mg RF coil (50 µm thick), Si NM RF diode (320 nm thick), and Mg/SiO₂/Mg parallel-plate capacitor (30 µm/100 nm/30 µm thick) (left) and image of on-demand release of blue dye by accelerated degradation of gate metal with wirelessly generated current in PBS (right). Adapted with permission from References [128]. © 2020, American Association for the Advancement of Science (For interpretation of the references to colour in this figure legend, the reader is referred to the web version of this article.).

diode, and an Mg/SiO₂/Mg parallel-plate capacitor. [128] Electro-chemically accelerated dissolution of metal gate sealing occurs through the wirelessly delivered electrical current, resulting in the release of drugs from the PBTpa reservoir [128]. Multiple drugs can be delivered by independent triggers through distinct drug reservoirs and corresponding RF harvesters [128]. A drug delivery system with insulin was implanted under the skins of male Lewis rats, enabling independent triggering through RF power at different frequencies (5, 10, and 15 MHz) [128]. More than 80 % of the insulin was released into the

surroundings 10–30 min after the triggering, followed by conversion of glucose into glycogen in the liver, thereby reducing glucose levels in the blood. [128]. All constituents undergo complete dissolution after more than 4 weeks in pH 7.4 PBS at 85 °C, and the PBTpa reservoir has a projected lifetime of ~660 days in PBS at 37 °C, while other components dissolve more quickly [128].

7. Conclusions

The dissolution chemistry and kinetics of inorganic electronic materials, including semiconductors, dielectrics, and conductors, with respect to environmental factors, such as temperature, pH, and ion species, provide a wide choice of combinations of circuit materials suitable for diverse applications. Microstructural factors, such as crystallinity, porosity, doping, and alloy composition, permit a wide range of tunability of dissolution rates of transient devices via the process of material formation. Inorganic and organic transient encapsulants enable control of the diffusion of vapors such as water molecules, thus extending the functional lifetimes of transient devices to desired time frames. Active-trigger transient systems incorporating specific stimulus-responsive materials allow on-demand initiation of transience and remote control of degradation via integration with wireless stimulus generators. Various fabrication strategies can support the construction of a transient electronic system using appropriate materials and an appropriate design structure. Transfer printing is a method that protects the reactive and sensitive layers from aggressive effects of high temperature and the solution processes by exploiting mechanical integration between an inorganic electronic circuit and soft and flexible polymer substrates. A solution process using biodegradable electronic inks that consist of inorganic particles and a polymer matrix provides other fabrication options that exploit the advantages of low-temperature and large-area processing. Clinically relevant biomedical applications, including temporary monitoring of acute diseases, post-surgical monitoring, regenerative therapy, controlled drug delivery, and others, demonstrate the feasibility of integrating transient electronics into practice.

The research aspects of the field remain very interesting and will likely continue to grow on that basis alone. Understanding the dissolution kinetics of other potential transient electronic materials is necessary to extend the ranges of dissolution rates and electrical properties. Exploring various dimensional materials, such as nanoparticles, nanowires, and two-dimensional (2-D) single layers, is an approach that has promise for widening the bandgap properties, dissolution kinetics, and mechanical form factors. Future advances in the design of materials via alloying metals and inorganic compounds can create unique degradation kinetics and electrical functionality. Fundamental modeling and computational approaches may be required to understand the diffusion dynamics of ions and water vapor through transient encapsulants, as well as the effects of electrochemical interactions on the degradation process at the atomic and molecular levels. Advances in materials strategies to minimize the gap between the dissolution period and water permeation are required for month- to year-scale transient applications. Biocompatible and degradable stimulus-responsive materials are also important for on-demand lifetime control of transient electronic devices in medical applications. From the point of view of fabrication, more complicated circuits and higher-level integration, including stacking and packaging, are foreseen for advanced digitalized and logic-processable transient systems. Interfacial properties or disintegration strategies will be important for both structural reliability and dissolution speeds.

Looking further into the future, an important driving force sustaining the field will be applications. Demonstrated advances may reveal opportunities for other applications in biodegradable electronics such as implantable electroceuticals for acute pain relief and regeneration of nerve or cardiac tissues, temporary pacemakers during surgical recovery or acute diseases, injectable biochemical sensors like pH and glucose monitors for use in emergency and battlefield sites, and other on/post-surgical device like thermo/chemotherapy devices for tumor treatment after surgery and biochemical sensors for detecting tumor recurrence. Eco-friendly devices, such as eco-degradable energy harvesters and disposable electronic patches (E-patches) for health monitoring combined with mass production of solution processes using recycled electronic powders – such as Si particles ground from discarded wafers,

hardware-security devices like transient memory chips that disintegrate when use ends and fully degradable military drones blocking information leakage with remote triggers – are also of growing interest as personalized electronic devices and autonomous robots and drones become more common. Accurate degradation and reliable initiation of triggering events are critical in translating transient electronics to other fields of practice. Transient electronics have huge potential in terms of both fundamental and applied research. This article both summarizes the state of the art of transient electronics and offers various suggestions for their future uses.

Declaration of Competing Interest

The authors report no declarations of interest.

Acknowledgement

This paper was supported by the National Research Foundation of Korea (NRF) grant funded by the Korea government (MSIT) (NRF-2019R1C1C1004232) and by KIST Institutional Program (Project No. 2V07080-19-P141).

References

- [1] Y.H. Joung, Int. Neurotol. J. 17 (2013) 98–106.
- [2] X. Yu, Z. Xie, Y. Yu, J. Lee, A.V. Guardado, H. Luan, et al., Nature 575 (2019) 473–479.
- [3] S. Xu, A. Jayaraman, J.A. Rogers, Nature 571 (2019) 319–321.
- [4] H.U. Chung, B.H. Kim, J.Y. Lee, J. Lee, Z. Xie, E.M. Ibler, et al., Science 363 (2019), eaau0780.
- [5] Y. Liu, J.J.S. Norton, R. Qazi, Z. Zou, K.R. Ammann, H. Liu, et al., Sci. Adv. 2 (2016), e1601185.
- [6] S.I. Park, D.S. Brenner, G. Shin, C.D. Morgan, B.A. Copits, H.U. Chung, et al., Nat. Biotechnol. 33 (2015) 1280–1286.
- [7] R.C. Webb, Y. Ma, S. Krishnan, Y. Li, S. Yoon, X. Guo, et al., Sci. Adv. 1 (2015), e1500701.
- [8] C.H. Lee, H. Kim, D.V. Harburg, G. Park, Y. Ma, T. Pan, et al., NPG Asia Mater. 7 (2015) e227.
- [9] S.K. Kang, R.K.J. Murphy, S.W. Hwang, S.M. Lee, D.V. Harburg, N.A. Krueger, et al., Nature 530 (2016) 71–76.
- [10] K.J. Yu, D. Kuzum, S.W. Hwang, B.H. Kim, H. Juul, N.H. Kim, et al., Nat. Mater. 15 (2016) 782–791.
- [11] J. Koo, M.R. MacEwan, S.K. Kang, S.M. Won, M. Stephen, P. Gamble, et al., Nat. Med. 24 (2018) 1830–1836.
- [12] Peeranart Kiddee, Ravi Naidu, M.H. Wong, Waste Manage. 33 (2013) 1237–1250.
- [13] A.R.K. Gollakota, S. Gautam, C.M. Shu, J. Environ. Manage. 261 (2020), 110234.
- [14] J.A. Amoah, Technol. Forecast. Soc. Change 105 (2016) 20–26.
- [15] S.W. Hwang, H. Tao, D.H. Kim, H. Cheng, J.K. Song, E. Rill, et al., Science 337 (2012) 1640–1644.
- [16] H.L. Hernandez, S.K. Kang, O.P. Lee, S.W. Hwang, J.A. Kaitz, B. Inci, et al., Adv. Mater. 26 (2014) 7637–7642.
- [17] C.W. Park, S.K. Kang, H.L. Hernandez, J.A. Kaitz, D.S. Wie, J. Shin, et al., Adv. Mater. 27 (2015) 3783–3788.
- [18] C.H. Lee, J.W. Jeong, Y. Liu, Y. Zhang, Y. Shi, S.K. Kang, et al., Adv. Funct. Mater. 25 (2015) 5100–5106.
- [19] M. Prakasam, J. Locs, K. Salma-Ancane, D. Loca, A. Largeteau, L. Berzina-Ciminda, J. Funct. Biomater. 8 (2017) 44.
- [20] P.A. Gunatillake, R. Adhikari, Eur. Cell. Mater. 5 (2003) 1–16.
- [21] D.H. Kim, Y.S. Kim, J. Amsden, B. Panilaitis, D.L. Kaplan, F.G. Omenetto, et al., Appl. Phys. Lett. 95 (2009), 133701.
- [22] C.J. Bettinger, Z. Bao, Adv. Mater. 2 (2010) 651–655.
- [23] M. Irimia-Vladu, P.A. Troshin, M. Reisinger, L. Shmygleva, Y. Kanbur, G. Schwabegger, et al., Adv. Funct. Mater. 20 (2010) 4069–4076.
- [24] T. Lei, M. Guan, J. Liu, H.C. Lin, R. Pfäffner, L. Shaw, et al., Proc. Natl. Acad. Sci. 114 (2017) 5107–5112.
- [25] K. Liu, H. Tran, V. Feig, Z. Bao, MRS Bull. 45 (2020) 96–102.
- [26] S.W. Hwang, D.H. Kim, H. Tao, T.i. Kim, S. Kim, K.J. Yu, et al., Adv. Funct. Mater. 23 (2013) 4087–4093.
- [27] S.W. Hwang, J.K. Song, X. Huang, H. Cheng, S.K. Kang, B.H. Kim, et al., Adv. Mater. 26 (2014) 3905–3911.
- [28] S.W. Hwang, X. Huang, J.H. Seo, J.K. Song, S. Kim, S. Hage-Ali, et al., Adv. Mater. 25 (2013) 3526–3531.
- [29] S.W. Hwang, C.H. Lee, H. Cheng, J.W. Jeong, S.K. Kang, J.H. Kim, et al., Nano Lett. 15 (2015) 2801–2808.
- [30] Y. Choi, J. Koo, J.A. Rogers, MRS Bull. 45 (2020) 103–112.
- [31] S.K. Kang, L. Yin, C. Bettinger, MRS Bull. 45 (2020) 87–95.
- [32] S.K. Kang, J. Koo, Y.K. Lee, J.A. Rogers, Acc. Chem. Res. 51 (2018) 988–998.
- [33] H. Cheng, J. Mater. Res. 31 (2016) 2549–2570.

- [34] S.W. Hwang, G. Park, H. Cheng, J.K. Song, S.K. Kang, L. Yin, et al., *Adv. Mater.* 26 (2014) 1992–2000.
- [35] S.K. Kang, G. Park, K. Kim, S.W. Hwang, H. Cheng, J. Shin, et al., *ACS Appl. Mater. Interfaces* 7 (2015) 9297–9305.
- [36] S.K. Kang, S.W. Hwang, H. Cheng, S. Yu, B.H. Kim, J.H. Kim, et al., *Adv. Funct. Mater.* 24 (2014) 4427–4434.
- [37] L. Yin, H. Cheng, S. Mao, R. Haasch, Y. Liu, X. Xie, et al., *Adv. Funct. Mater.* 24 (2014) 645–658.
- [38] L. Yin, A.B. Farimani, K. Min, N. Vishal, J. Lam, Y.K. Lee, et al., *Adv. Mater.* 27 (2015) 1857–1864.
- [39] S.W. Hwang, G. Park, C. Edwards, E.A. Corbin, S.K. Kang, H. Cheng, et al., *ACS Nano* 8 (2014) 5843–5851.
- [40] R. Li, H. Cheng, Y. Su, S.W. Hwang, L. Yin, H. Tao, et al., *Adv. Funct. Mater.* 23 (2013) 3106–3114.
- [41] S.W. Hwang, S.K. Kang, X. Huang, M.A. Brenckle, F.G. Omenetto, J.A. Rogers, *Adv. Mater.* 27 (2015) 47–52.
- [42] H. Fang, J. Zhao, K.J. Yu, E. Song, A.B. Farimani, C.H. Chiang, et al., *Proc. Natl. Acad. Sci.* 113 (2016) 11682–11687.
- [43] G. Lee, Y.S. Choi, H.J. Yoon, J.A. Rogers, *Matter* 3 (2020) 1031–1052.
- [44] W.B. Han, G.J. Ko, J.W. Shin, S.W. Hwang, *MRS Bull.* 45 (2020) 113–120.
- [45] X. Huang, Y. Liu, S.W. Hwang, S.K. Kang, D. Patnaik, J.F. Cortes, et al., *Adv. Mater.* 26 (2014) 7371–7377.
- [46] S. Lee, J. Koo, S.K. Kang, G. Park, Y.J. Lee, Y.Y. Chen, et al., *Mater. Today* 21 (2018) 207–215.
- [47] B.K. Mahajan, X. Yu, W. Shou, H. Pan, X. Huang, *Small* 13 (2017), 1700065.
- [48] B.K. Mahajan, B. Ludwig, W. Shou, X. Yu, E. Fregene, H. Xu, et al., *Sci. China Inf. Sci.* 61 (2018), 060412.
- [49] J. Li, S. Luo, J. Liu, H. Xu, X. Huang, *Materials Basel* (Basel) 11 (2018) 1102.
- [50] S. Feng, Z. Tian, J. Wang, S. Cao, D. Kong, *Adv. D. Electron. Mater.* 5 (2019), 1800693.
- [51] S. Feng, S. Cao, Z. Tian, H. Zhu, D. Kong, *ACS Appl. Mater. Interfaces* 11 (2019) 45844–45852.
- [52] Y.K. Lee, J. Kim, Y. Kim, J.W. Kwak, Y. Yoon, J.A. Rogers, *Adv. Mater.* 29 (2017), 1702665.
- [53] J. Li, H. Xu, Z. Zhang, Y. Hao, H. Wang, X. Huang, *Adv. Funct. Mater.* 30 (2020), 1905024.
- [54] J. Shin, Z. Liu, W. Bai, Y. Liu, Y. Yan, Y. Xue, et al., *Sci. Adv.* 5 (2019), eaaw1899.
- [55] H. Seidel, L. Csepregi, A. Heuberger, H. Baumgärtel, *J. Electrochem. Soc.* 137 (1990) 3612–3626.
- [56] Y.K. Lee, K.J. Yu, E. Song, A.B. Farimani, F. Vitale, Z. Xie, et al., *ACS Nano* 11 (2017) 12562–12572.
- [57] A.F. Wallace, G.V. Gibbs, P.M. Dove, *J. Phys. Chem. A* 114 (2010) 2534–2542.
- [58] L. Wang, Y. Gao, F. Dai, D. Kong, H. Wang, P. Sun, et al., *ACS Appl. Mater. Interfaces* 11 (2019) 18013–18023.
- [59] H. Seidel, L. Csepregi, A. Heuberger, H. Baumgärtel, *J. Electrochem. Soc.* 137 (1990) 3626–3632.
- [60] S.H.C. Anderson, H. Elliott, D.J. Wallis, L.T. Canham, J.J. Powell, *phys. stat. sol. (a)* 197 (2003) 331–335.
- [61] E.J. Anglin, L. Cheng, W.R. Freeman, M.J. Sailor, *Adv. Drug Deliv. Rev.* 60 (2008) 1266–1277.
- [62] L.T. Canham, C.L. Reeves, D.O. King, P.J. Branfield, J.G. Crabb, M.C.L. Ward, *Adv. Mater.* 8 (1996) 850–852.
- [63] S.P. Low, N.H. Voelcker, *Handbook of Porous Silicon* (2014) 381–393.
- [64] F. Witte, *Acta Biomater.* 6 (2010) 1680–1692.
- [65] F. Witte, J. Fischer, J. Nellesen, C. Vogt, J. Vogt, T. Donath, et al., *Acta Biomater.* 6 (2010) 1792–1799.
- [66] F. Witte, N. Hort, C. Vogt, S. Cohen, K.U. Kainer, R. Willumeit, et al., *Curr Opin Solid State Mat Sci* 12 (2008) 63–72.
- [67] W. Bai, J. Shin, R. Fu, I. Kandela, D. Lu, X. Ni, et al., *Nat. Biomed. Eng.* 3 (2019) 644–654.
- [68] W.W. Harvey, H.C. Gatos, et al., *J. Electrochem. Soc.* 105 (1958) 654–660.
- [69] J.T. Borenstein, N.D. Gerrish, M.T. Currie, E.A. Fitzgerald, *IEEE Micro Electro Mech. Syst.* (1999) 205–210.
- [70] S.H. Jin, S.K. Kang, I.T. Cho, S.Y. Han, H.U. Chung, D.J. Lee, et al., *ACS Appl. Mater. Interfaces* 7 (2015) 8268–8274.
- [71] C. Dagdeviren, S.W. Hwang, Y. Su, S. Kim, H. Cheng, O. Gur, et al., *Small* 9 (2013) 3398–3404.
- [72] D. Lu, T.L. Liu, J.K. Chang, D. Peng, Y. Zhang, J. Shin, et al., *Adv. Mater.* 31 (2019), 1902739.
- [73] P.V. Brady, J.V. Walther, *Chem. Geol.* 82 (1990) 253–264.
- [74] F.K. Crundwell, *ACS Omega* 2 (2017) 1116–1127.
- [75] Y. Niibori, M. Kunita, O. Tochiyama, T. Chida, J. Nucl. Sci. Technol. 37 (2000) 349–357.
- [76] J. Shin, Y. Yan, W. Bai, Y. Xue, P. Gamble, L. Tian, et al., *Nat. Biomed. Eng.* 3 (2019) 37–46.
- [77] Y.K. Lee, K.J. Yu, Y. Kim, Y. Yoon, Z. Xie, E. Song, et al., *ACS Appl. Mater. Interfaces* 9 (2017) 42633–42638.
- [78] M.M. Adeva, G. Souto, N. Blanco, C. Donapetry, *Metabolism* 61 (2012) 1495–1511.
- [79] O. Fruhwirth, G.W. Herzog, I. Hollerer, A. Rachetti, *Subsurf. Sens. Technol. Appl.* 24 (1985) 301–317.
- [80] A. Fedorová, P. Raschman, *Chem. Eng. Sci.* 143 (2008) 265–272.
- [81] S.K. Kang, S.W. Hwang, S. Yu, J.H. Seo, E.A. Corbin, J. Shin, et al., *Adv. Funct. Mater.* 25 (2015) 1789–1797.
- [82] Y. Liu, Y. Zheng, X.H. Chen, J.A. Yang, H. Pan, D. Chen, et al., *Adv. Funct. Mater.* 29 (2019), 1805402.
- [83] R.W. Revie, H.H. Uhlig, *Corrosion and Corrosion Control: An Introduction to Corrosion Science and Engineering*, 4th Edition, John Wiley & Sons, New Jersey, 2008, pp. 115–148.
- [84] W.A. Badawy, F. M. Al-Kharafi 44 (1998) 693–702.
- [85] R.S. Lillard, G.S. Kanner, D.P. Butt, *J. Electrochem. Soc.* 145 (1998) 2718–2725.
- [86] E.S.M. Sherif, R.M. Erasmus, J.D. Comins, *Electrochim. Acta* 55 (2010) 3657–3663.
- [87] M. Irimia-Vladu, E.D. Glowacki, G. Voss, S. Bauer, N.S. Sariciftci, *Mater. Today* 15 (2012) 340–346.
- [88] M.E. Roberts, S.C.B. Mannsfeld, N. Queralto, C. Reese, J. Locklin, W. Knoll, et al., *Proc. Natl. Acad. Sci.* 105 (2008) 12134–12139.
- [89] A. Pron, P. Rannou, *Prog. Polym. Sci.* 27 (2002) 135–190.
- [90] M. Irimia-Vladu, E.D. Glowacki, P.A. Troshin, G. Schwabegger, L. Leonat, D. K. Susarova, et al., *Adv. Mater.* 24 (2012) 375–380.
- [91] M. Vautier, C. Guillard, J.M. Herrmann, *J. Catal.* 201 (2001) 46–59.
- [92] C.J. Bettinger, J.P. Bruggeman, A. Misra, J.T. Borenstein, R. Langer, *Biomaterials* 30 (2009) 3050–3057.
- [93] A.B. Mostert, B.J. Powell, F.L. Pratt, G.R. Hanson, T. Sarna, I.R. Gentle, et al., *Proc. Natl. Acad. Sci.* 109 (2012) 8943–8947.
- [94] E. Song, Y.K. Lee, R. Li, J. Li, X. Jin, K. Yu, et al., *Adv. Funct. Mater.* 28 (2018), 1702284.
- [95] S.M. Won, J. Koo, K.E. Crawford, A.D. Mickle, Y. Xue, S. Min, et al., *Adv. Funct. Mater.* 28 (2018), 1801819.
- [96] Q.S. Yang, S. Lee, Y. Xue, Y. Yan, T.L. Liu, S.K. Kang, et al., *Adv. Funct. Mater.* 30 (2020), 1910718.
- [97] Y.S. Choi, J. Koo, Y.J. Lee, G. Lee, R. Avila, H. Ying, et al., *Adv. Funct. Mater.* 30 (2020), 2000941.
- [98] D. Liu, S. Zhang, H. Cheng, R. Peng, Z. Luo, et al., *Sci. Rep.* 9 (2019) 18107.
- [99] J. Yoon, J. Lee, B. Choi, D. Lee, D.H. Kim, D.M. Kim, et al., *Nano Res.* 10 (2017) 87–96.
- [100] G.J. Li, E.M. Song, G.S. Huang, Q.L. Guo, F. Ma, B. Zhou, et al., *Adv. Funct. Mater.* 28 (2018), 1801448.
- [101] A. Gumus, A. Alam, A.M. Hussain, K. Mishra, I. Wicaksono, G.A. Torres Sevilla, et al., *Int. J. Adv. Mater. Technol.* 2 (2017), 1600264.
- [102] X. Zhang, L.M. Bellan, *ACS Appl. Mater. Interfaces* 9 (2017) 21991–21997.
- [103] K. Fu, Z. Liu, Y. Yao, Z. Wang, B. Zhao, W. Luo, et al., *Nano Lett.* 15 (2015) 4664–4671.
- [104] L. Yin, X. Huang, H. Xu, Y. Zhang, J. Lam, J. Cheng, et al., *Adv Mater.* 26 (2014) 3879–3884.
- [105] Y. Gao, Y. Zhang, X. Wang, K. Sim, J. Liu, J. Chen, et al., *Sci. Adv.* 3 (2017), e1701222.
- [106] S. Zhong, X. Ji, L. Song, Y. Zhang, R. Zhao, *ACS Appl. Mater. Interfaces* 10 (2018) 36171–36176.
- [107] W.D. Chen, S.K. Kang, W.J. Stark, J.A. Rogers, R.N. Grass, *Sens. Actuators B Chem.* 282 (2019) 52–59.
- [108] N. Muralidharan, J. Afolabi, K. Share, M. Li, C.L. Pint, *Int. J. Adv. Mater. Technol.* 3 (2018), 1800083.
- [109] A. Douglas, N. Muralidharan, R. Carter, K. Share, C.L. Pint, *Nanoscale* 8 (2016) 7384–7390.
- [110] K. Sim, X. Wang, Y. Li, C. Linghu, Y. Gao, J. Song, et al., *J. Micromech. Microeng.* 27 (2017), 065010.
- [111] S.S. Pandey, N. Banerjee, Y. Xie, C.H. Mastrangelo, *Int. J. Adv. Mater. Technol.* 3 (2018), 1800044.
- [112] Y. Chen, H. Wang, Y. Zhang, R. Li, C. Chen, H. Zhang, et al., *Nanotechnology* 30 (2019), 394002.
- [113] C. You, H. Zhao, Q. Guo, Y. Mei, *MRS Bull.* 45 (2020) 129–134.
- [114] C.E. Diesendruck, G.I. Peterson, H.J. Kulik, J.A. Kaitz, B.D. Mar, P.A. May, et al., *Nat. Chem.* 6 (2014) 623–628.
- [115] H.L. Hernandez, O.P. Lee, C.M.P. Casey, J.A. Kaitz, C.W. Park, C.L. Plantz, et al., *Macromol. Rapid Commun.* 39 (2018), 1800046.
- [116] J.K. Chang, H. Fang, C.A. Bower, E. Song, X. Yu, J.A. Rogers, *Proc. Natl. Acad. Sci.* 114 (2017) E5522–E5529.
- [117] H. Fang, K. Yu, C. Gloschat, Z. Yang, E. Song, C.H. Chiang, et al., *Nat. Biomed. Eng.* 0038 (2017) 1–11.
- [118] G. Lee, S.K. Kang, S.M. Won, P. Gutruf, Y.R. Jeong, J. Koo, et al., *Adv. Energy Mater.* 7 (2017), 1700157.
- [119] Q. Zheng, Y. Zou, Y. Zhang, Z. Liu, B. Shi, X. Wang, *Sci. Adv.* 2 (2016), e1501478.
- [120] M.M. Khan, Z.U. Rahman, K.M. Deen, I. Shabib, W. Haider, *Electrochim. Acta* 329 (2020), 135129.
- [121] X. Huang, D. Wang, Z. Yuan, W. Xie, Y. Wu, R. Li, et al., *Small* 14 (2018), 1800994.
- [122] J.P. Esquivel, P. Alday, O.A. Ibrahim, B. Fernandez, E. Kjeang, N. Sabate, *Adv. Energy Mater.* 7 (2017), 1700275.
- [123] M.H. Lee, J. Lee, S.-K. Jung, D. Kang, M.S. Park, G.D. Cha, et al., *Adv. Mater.* 33 (2021), 2004902.
- [124] H. Sheng, J. Zhou, B. Li, Y. He, X. Zhang, J. Liang, et al., *Sci. Adv.* 7 (2021), eabe3097.
- [125] L.H. Stoodley, J. Costerton, P. Stoodley, *Nat. Rev. Microbiol.* 2 (2004) 95–108.
- [126] C.M. Boutry, Y. Kaizawa, B.C. Schroeder, A. Chortos, A. Legrand, Z. Wang, et al., *Nat. Electron.* 1 (2018) 314–321.
- [127] H. Tao, S.W. Hwang, B. Marelli, B. A, J.E. Moreau, M. Yang, et al., *Proc. Natl. Acad. Sci.* 111 (2014) 17385–17389.
- [128] J. Koo, S.B. Kim, Y.S. Choi, Z. Xie, A.J. Bandodkar, J. Khalifeh, et al., *Sci. Adv.* 6 (2020), eabb1093.
- [129] J.I. Laughner, S.B. Marrus, E.R. Zellmer, C.J. Weinheimer, M.R. MacEwan, S. X. Cui, et al., *PLoS One* 8 (2013), e76291.

- [130] W.B. Han, J.H. Lee, J.W. Shin, S.W. Hwang, *Adv. Mater.* 32 (2020), 2002211.
- [131] R. Li, L. Wang, L. Yin, *Materials* 11 (2018) 2108.
- [132] Brain Trauma Foundation, *Neurotrauma* 24 (2007) S37–S44.
- [133] C.M. Boutry, L. Beker, Y. Kaizawa, C. Vassos, H. Tran, A.C. Hinckley, et al., *Nat. Biomed. Eng.* 3 (2019) 47–57.
- [134] R. Li, H. Qi, Y. Ma, Y. Deng, S. Liu, Y. Jie, et al., *Nat. Commun.* 11 (2020) 3207.
- [135] Y.S. Choi, Y.Y. Hsueh, J. Koo, Q. Yang, R. Avila, B. Hu, et al., *Nat. Commun.* 11 (2020) 5990.
- [136] L. Wang, C. Lu, S. Yang, P. Sun, Y. Wang, Y. Guan, et al., *Sci. Adv.* 6 (2020), eabc6686.
- [137] S.A. Stewart, J.D. Robles, R.F. Donnelly, E. Larrañeta, *Polymers (Basel)*. 10 (2018) 1379.



Jun-Seok Shim is a Ph.D. candidate in the Department of Materials Science and Engineering at Seoul National University, Republic of Korea, since 2020. He obtained his BS in materials science and engineering from Seoul National University in 2020. Shim's research includes materials chemistry and fabrication of green energy electronics.



John A. Rogers is the Louis Simpson and Kimberly Querrey Professor of Materials Science and Engineering, Biomedical Engineering and Medicine at Northwestern University, with affiliate appointments in Mechanical Engineering, Electrical and Computer Engineering and Chemistry, where he is also Director of the recently endowed Querrey/Simpson Institute for Bioelectronics, since 2016. He obtained BA and BS degrees in chemistry and in physics from the University of Texas, Austin, in 1989. From MIT, he received SM degrees in physics and in chemistry in 1992 and the PhD degree in physical chemistry in 1995. From 1995–1997, Rogers was a Junior Fellow in the Harvard University Society of Fellows. He joined Bell Laboratories as a Member of Technical Staff in the Condensed Matter Physics Research Department in 1997, and served as Director of this department from 2000 to 2002. He then spent thirteen years on the faculty at University of Illinois, most recently as the Swanson Chair Professor and Director of the Seitz Materials Research Laboratory. His interests are in unusual electronic materials and devices, with an emphasis on bio-integrated systems and bio-inspired designs. He is a member of the National Academy of Engineering, the National Academy of Sciences, the National Academy of Medicine, the National Academy of Inventors and the American Academy of Arts and Sciences.



Seung-Kyun Kang is an assistant professor in the Department of Materials Science and Engineering at Seoul National University, Republic of Korea, since 2019. He was an assistant professor in the Department of Bio and Brain Engineering at the Korea Advanced Institute of Science and Technology, Republic of Korea from 2017 to 2019. He obtained his BS in materials science and engineering from Seoul National University in 2006 with honor and early graduate. He received Ph.D. degrees in Materials Science and Engineering from Seoul National University 2012. He was a postdoctoral researcher at the University of Illinois at Urbana-Champaign from 2012 to 2016 and at Northwestern University from 2016 to 2017. Kang's research applied aspects of materials for biointerface technologies and biodegradable electronics.